Development of Metamaterial Composites for Compact High Power Microwave Systems and Antennas

ONR Contract Number
N00014-13-1-0516

Final Report submitted May 2016

Presented to: Joong Kim, PhD
Deputy Program Manager
Force Protection Thrust, Code 30
Office of Naval Research

Prepared by:

Dr. Randy Curry, PI

Technical Contributors: Kevin O'Connor, Aric Pearson, Kelli Noel, Sarah Mounter

University of Missouri-Columbia Center for Physical and Power Electronics
Electrical and Computer Engineering
311 Engineering Building West
Columbia, MO 65211
573-882-3017
curryrd@missouri.edu

Table of Contents

Table of Figures

1. Executive Summary

During the period of performance we investigated the electrical and mechanical properties of two types of ferrite metamaterials: "ferrite-based composites" and "core-shell composites." Both were fabricated using advanced polymer composite techniques and then characterized. The measurements were compared to models and the analysis is presented in this report.

The ferrite-based composites consist of combining a ferrite powder with a silane binder and pressing them together following a mixing operation. These composites are easily manufactured in bulk and their properties can be tailored to specific wave impedance requirements.

In the other approach, the core-shell composites are formed by chemically depositing a barium titanate ($BaTiO_3$) shell around a ferrite core to form a composite of small "beads" of ferrite surrounded by insulating $BaTiO_3$.

Both metamaterials were then fabricated into test coupons and the electrical properties were investigated.

Investigations of electrical properties included: studies of real and imaginary permeability of the composite materials; studies of real and imaginary permittivity of the composites; electrical breakdown strength of the composites.

Accomplishments included:

- Fabrication of test coupons (disks) of ferrite-based composites of varying thickness and emplacing electrodes on the disks
- Investigating the breakdown voltages of the disks utilizing a high voltage nanosecond PA-80 pulser to apply high voltages to the disks under a dielectric fluid until breakdown occurred
- Correlating the breakdown voltages for varying test coupon thicknesses
- Fabricating test coupons (disks) of core-shell composites
- Comparing the electrical properties of the ferrite-based composites with the core-shell composites
- Surface modification of composite materials to increase voltage hold-off
- Fabrication of continuous particle distribution, bimodal (two distinct particle sizes) particle distribution and trimodal (three distinct particle sizes) particle distribution composites
- Investigation of ε_r' and μ_r' of the three different distributions as a function of frequency
- Investigation of dielectric strength of the composites when manufactured into 2.54 cm diameter disks: bimodal and trimodal disks held off significantly higher fields than continuous-distribution composites
- Investigation of the bimodal and trimodal material properties to improve understanding of the relationship of material properties to electrical properties
- Investigation of the material properties of core-shell particles built around 30 nm, 5 μm and 45 μm ferrite particles

- Electromagnetic simulation of ferrite composites to confirm the properties of different formulations. The simulations utilize 3-D CST Monte Carlo techniques to fill a volume with composites. The simulations confirm properties of trimodal distributions; both permittivity and permeability.

2. Introduction

High power microwave devices have a large number of commercial and military applications. However, such devices have yet to reach their full potential due to limitations in size and portability. In particular, the large size of high power microwave antennas can limit their application for portable or compact systems. The development of new materials to be used in antenna construction is seen as a promising method to enable improved miniaturization of antennas and potentially other system components.

The key focus of this program was to develop a metamaterial that has both permittivity and permeability matching the wave impedance to free space. The materials developed must also have high voltage breakdown fields comparable to ferrites or polymers for use in high powered microwave applications. The groundwork for the metamaterial began with a high-dielectric composite developed from barium titanate ceramics made into composites. The development of a multiferroic metamaterial was approached from two fronts. One aspect is focused on ferrite particles as the main component of the composite. The focus of this work is to combine the ferrite particles with barium titanate ceramics into a composite with different dielectric and magnetic materials.

3. Theory

3.1 Multiferroic Metamaterials

A metamaterial is defined as a material engineered to have properties not found in nature [1]. Metamaterials have been investigated for electromagnetic wave applications many times before and are classified depending on the permittivity and permeability. For high power applications, the focus of this research was on double positive metamaterials. Double positive metamaterials have both relative permittivity and permeability values that are above that of free space [2]. Combining ferroelectric and ferromagnetic materials into one multiferroic composite is the approach to achieve the higher levels of both permittivity and permeability desired. Engineering a multiferroic metamaterial is necessary for the design flexibility in the material properties and a high power capability. Similar metamaterial approaches involving insulating structures or grain boundaries to obtain material properties are not typically applicable for high power microwave systems with

exceptionally high fields [3]. Edge effects and field enhancement due to the resonant structures on the metal surfaces can result in flashover at the surface of the insulator.

Designing metamaterials with both increased permittivity and permeability can enhance the capabilities of a structure that uses such a material. A change in electromagnetic properties in the fabrication substrate can significantly reduce the size of an antenna. While the geometry of antennas differ, the basic principle, that the dimension of the antenna should be proportional to the operating wavelength, remains the same [4]. If an antenna is designed with a dielectric material, the wavelength, and thus the dimensions, of the antenna is determined by the velocity of the wave propagation in the material as seen in Equation 3.1.1. By increasing both the permittivity and permeability, the dimensions of an antenna can be greatly reduced.

$$l \propto \lambda_a = \frac{1}{f\sqrt{\epsilon_0 \epsilon_r \mu_0 \mu_r}} \tag{3.1.1}$$

Another factor that is greatly affected by the permittivity and permeability of a material is impedance. Equation 3.1.2 shows the relation of impedance to permittivity and permeability. If only the permittivity of a material were increased, the impedance seen by a wave in the material would be decreased and would result in reflections or impedance mismatches from the antenna radiating into free space [5]. The mismatch of impedances at the interface between the material and free space, reduces the efficiency of a traveling wave antenna. If both the permittivity and permeability were increased simultaneously, the size reduction would increase antenna efficiency and the impedance mismatch would not be as great or even eliminated.

$$\eta = \sqrt{\frac{\mu_0 \mu_r}{\epsilon_0 \epsilon_r}} \tag{3.1.2}$$

It is also important to have materials with low loss. In a dielectric material, loss is characterized by the ratio of the real part of the complex permittivity to the imaginary part, termed tangent, as seen in Equation 3.1.3. Materials with high losses, or lossy materials, have a loss tangent greater than one and can form resonant effects inside the material, excluding the propagation of waves through the material [6]. A multiferroic material has both dielectric and magnetic losses that can affect wave propagation.

$$\gamma = \frac{\epsilon''}{\epsilon'} \tag{3.1.3}$$

3.2 Ferrites

A multiferroic metamaterial must have both permittivity and permeability greater than that of free space, and low losses in the ultrahigh frequency (UHF) band and very high frequency band (VHF) for high powered applications. Ferrite materials meet these criteria. Ferrites have high permeability values in the UHF and VHF ranges as well as increased permittivity depending on the atomic structures. This allows them to couple well with electromagnetic devices and have low losses [7].

Ferrites are magnetic oxides, usually with atomic structure Fe_2O_4, that have additional metals in the crystalline lattice to add specific magnetic characteristics and they exist as cubic or hexagonal structures with compact and repeating lattices. These structures exist due to the crystalline structure of the oxygen atoms in the material. The oxygen ions originally form in a set of equilateral triangles, and then align themselves in layers. If the layers of oxygen ions align themselves with the center of the previous layers' triangles in a repeating ababab pattern, the hexagonal form of ferrite is found. If the third layer of oxygen ions aligns directly with the second layer, and then the fourth layer is aligned with the first in an abcabc pattern, the cubic form is found. Spinal ferrites are a type of cubic close-packed structure and are the most prolific geometry of ferrite [8]. Figure 1 shows the two geometries of ferrite typically found in nature. The type of crystalline structure is determined by the size and charge of the metal ions that balance the oxygen ions, and is related to the application of the ferrites. Nickel-Zinc ferrites are a type of spinal ferrite, where the nickel is added to provide extra unpaired electrons that add to the magnetic moment of the particles and the zinc, while not paramagnetic, also increases the magnetic moment. Nickel-zinc ferrites also have increased resistivity and lower losses which makes them more useful at frequencies above 1 MHz [9].

Since ferrites have their magnetic ions distributed over at least two interpenetrating sub-lattices, ferrites exhibit nonreciprocal properties in terms of the phase constants and phase velocities experienced by circularly polarized waves, transmission coefficients, and tensor based permeabilities [10]. Since the magnetic permeability of the bulk material is an important design parameter, this section will outline how the permeability is defined for ferrites.

The magnetic dipole moment $d\vec{m}$ of a magnetic dipole is given by Equation 3.2.1. If an external magnetic field, H_0 is applied, a torque $\vec{T}$ is felt by the dipole [10].

If the z axis is chosen to be parallel to the applied magnetic field, then the dipole will precess about this axis. The torque is given by

$$\vec{T} = \mu_0 \vec{m} \times \vec{H}_0 \qquad (3.2.1)$$

It is now helpful to look at the movement of the electrons in the dipole. The motion of the electrons around the nucleus result in a current I, that form a dipole moment described by

$$m = I\,ds = \frac{ev}{2\pi a}(\pi a^2) = \frac{1}{2}eva \tag{3.2.2}$$

where e is the charge of an electron, v is the velocity of the electron, and a is the radius of the circular path traced out by the electron [5]. While it is true that the electron's orbit around the nucleus is in fact far from circular, it is sufficient for our purposes and is used here in order to significantly simplify the analysis. We can also describe the angular momentum of the electron as

$$P = m_e va \tag{3.2.3}$$

where m_e is the mass of the electron. If we now take the ratio of the electron's magnetic moment and angular momentum we get

$$\gamma = \frac{m}{P} = \frac{e}{2m_e} \tag{3.2.4}$$

which is referred to as the gyromagnetic ratio.

From a macroscopic prospective, we can consider an infinite unbounded ferrite slab with an applied magnetic field $\vec{H}_0 = \vec{H}_0\hat{a}_z$. Letting all the electrons per unit volume be represented by N, then the total magnetization of a bulk piece of ferrite can be represented by

$$\vec{M} = N\vec{m} \tag{3.2.5}$$

If the applied external magnetic field is strong then $\vec{M} = \vec{M}_s$, where $\vec{M_s}$ is the saturation magnetization where all the magnetic domains in the material are aligned with the field [10]. When a time-varying magnetic field is also applied, $\vec{M}$ will have a time-varying component, $\vec{M}_{ac}$. In this case the equation of motion for the total magnetization per unit volume is given by

$$\frac{d(\vec{M}_s+\vec{M}_{ac})}{dt} = \frac{\vec{M}_{ac}}{dt} = -\gamma\left[\left(\vec{M}_s + \vec{M}_{ac}\right) \times \left(\vec{B}_0 + \mu_0\vec{H}_{ac}\right)\right] \tag{3.2.6}$$

where H_{ac} is the applied time-varying magnetic field. Equation 3.2.6 can be expanded to

$$\frac{dM_{ac}}{dt} = -\gamma(\vec{M}_s \times \vec{H}_0 + \vec{M}_s \times \vec{H}_{ac} + \vec{M}_{ac} \times \vec{H}_0 + \vec{M}_{ac} \times \vec{H}_{ac}) \tag{3.2.7}$$

If we now assume that the alternating portion of the magnetic field is small compared to the static portion so that $M_{ac} \ll M_s$ and $H_{ac} \ll H_0$ and since $M_s \times B_0 = 0$, we can reduce Equation 3.2.7 to

$$\frac{d\vec{M}_{ac}}{dt} = -\gamma(\mu_0 \vec{M}_s \times \vec{H}_{ac} + \vec{M}_{ac} \times \vec{B}_0) \tag{3.2.8}$$

Letting the time dependence of $\vec{H}_{ac}$ be given by Euler's relation $\vec{H}e^{j\omega t}$ we can again rewrite Equation 3.2.8 as

$$j\omega\vec{M} + \gamma\vec{M} \times B_0 = \gamma\omega\vec{M} + \omega_0\vec{M} \times \hat{a}_z = -\gamma\mu_0\vec{M}_s \times \vec{H} \tag{3.2.9}$$

where $\omega_0 = \gamma_0\mu_0 H_0$ is the Larmor procession frequency [10].

Separating Equation 3.2.9 into its spatial components, we have

$$j\omega M_x + \omega_0 M_y = \gamma M_s \mu_0 H_y \tag{3.2.10}$$

$$j\omega M_y - \omega_0 M_x = -\gamma M_s \mu_0 H_x \tag{3.2.11}$$

$$j\omega M_z = 0 \tag{3.2.12}$$

and solving for M_x, M_y, M_z gives

$$M_x = \frac{\omega_0\gamma\mu_0 M_s H_x + j\omega\gamma\mu_0 M_s H_y}{\omega_0^2 - \omega^2} \tag{3.2.13}$$

$$M_y = \frac{\omega_0\gamma\mu_0 M_s H_y + j\omega\gamma\mu_0 M_s H_x}{\omega_0^2 - \omega^2} \tag{3.2.14}$$

$$M_z = 0. \tag{3.2.15}$$

Putting Equations 3.2.13-3.2.15 into matrix form, we have

$$\begin{bmatrix} M_x \\ M_y \\ M_z \end{bmatrix} = \begin{bmatrix} \chi_{xx} & \chi_{xy} & 0 \\ \chi_{yx} & \chi_{yy} & 0 \\ 0 & 0 & 0 \end{bmatrix} \begin{bmatrix} H_x \\ H_y \\ H_z \end{bmatrix} \tag{3.2.16}$$

$$\chi_{xx} = \chi_{yy} = \frac{\omega_0 \gamma \mu_0 M_s}{\omega_0^2 - \omega^2} \tag{3.2.17}$$

$$\chi_{xy} = \chi_{yx} = \frac{j\omega \gamma \mu_0 M_s}{\omega_0^2 - \omega^2} \tag{3.2.18}$$

We can now write the B fields in similar form, giving

$$\begin{bmatrix} B_x \\ B_y \\ B_z \end{bmatrix} = \mu_0 \begin{bmatrix} 1+\chi_{xx} & \chi_{xy} & 0 \\ \chi_{yx} & 1+\chi_{yy} & 0 \\ 0 & 0 & 1 \end{bmatrix} \begin{bmatrix} H_x \\ H_y \\ H_z \end{bmatrix} \tag{3.2.19}$$

where

$$\bar{\mu} = \mu_0 \begin{bmatrix} 1+\chi_{xx} & \chi_{xy} & 0 \\ \chi_{yx} & 1+\chi_{yy} & 0 \\ 0 & 0 & 1 \end{bmatrix} \tag{3.2.20}$$

is the magnetic permeability tensor in ferrites [10].

Magnetic Losses in a bulk piece of ferrite are separated into three categories based on the Legg equation:

$$\frac{R}{L} = \mu e f^2 + \mu a f B_{max} + \mu c f \tag{3.2.21}$$

where R is the series resistance, L is the inductance in material under investigation, B_{max} is the maximum flux density in the material, and e, a, and c are constants [11]. On the right side of the equation the terms represent eddy current, hysteresis, and residual losses respectfully.

Eddy current losses occur due to an alternating magnetic field which induces circular currents in a magnetic material that in turn generate a secondary magnetic field that opposes the first. The constant e in Equation 3.2.21 can be related to the resistivity of the ferrite material by

$$\mu_0 e = \frac{8}{c_1} \pi^3 \frac{d^2}{\rho} \times 10^{-7} \tag{3.2.22}$$

where c_1 is a constant whose value depends on the geometry of the ferrite material. The value of c_1 for a sheet, cylinder, and sphere geometry has been shown to be 6, 16, and 20 respectfully [11]. At low frequencies, the reduction in the magnetizing field through eddy current is not significant due to there being sufficient time for the currents to dissipate and for the applied field to reach the center of the sample [12]. However, as the frequency is increased there is less time for the eddy currents to decay and thus the reverse magnetizing field becomes significant at the surface of the material. This reverse field shields the inside of the ferromagnetic material from the applied field, making it useless [12]. The skin depth of a material is defined as the point where the applied field is reduced to $1/e^{th}$ of what it is at the surface. The equation for the skin depth s is

$$s = \frac{1}{2}\pi\sqrt{\frac{\mu f}{\rho}} \qquad (3.2.23)$$

where f is the frequency and ρ is the resistivity.

A second type of loss in ferrite is related to the energy dissipated during a magnetic cycle. This is referred to as hysteresis loss and is proportional to the area enclosed by the hysteresis loop of the material. This type of loss is intrinsic to the lattice structure of the type of ferrite used [12].

Magnetic energy dispersion that cannot be attributed to either eddy currents or the hysteresis mechanism is called residual loss. Such losses are usually attributed to the relaxation of the domain walls within the ferrite material. As the frequency of the applied field increases the variation becomes so rapid that the domain walls cannot keep up since their relaxation frequency is in the 50MHz range [15]. Also, the walls are strongly bound to equilibrium position which result from the small voids in the polycrystalline ferrite structure. Differences in hard and soft ferrites stem from differing affinity for these equilibrium positions [11].

As discussed earlier, the permeability of a material has a major effect on the electromagnetic properties and wave propagation with the material. The choice of using ferrites as a magnetic core for the proposed metamaterial was made due to the standard permeability values of nickel-zinc ferrites in the UHF and VHF bands. Nickel-zinc ferrites are soft ferrites with higher resistivity at frequencies above 1 MHz. They also have low coercivity, meaning the magnetization of the material can change with very low magnetic losses [11].

3.3 Core Shell

Ferromagnetic materials are usually conductive, which would inhibit some of the applications in high frequency applications. To mitigate this property, the ferromagnetic material must be

insulated by a ferroelectric phase [13]. Perovskite ceramics have high permittivity values that, when used as a dielectric medium, can reduce the size of an antenna by a factor of 10 or more and act as an insulator. Barium titanate ($BaTiO_3$) is one such ceramic that has ε_r values of 100 or greater and high dielectric strength.

When a ferromagnetic and ferroelectric material are combined into one phase, an interesting phenomenon occurs known as the magnetoelectric (ME) effect [16]. The ME effect can be derived from the free energy equations that follow:

$$F(E,H) = F_0 - P_i^S E_i - M_i^S H_i - \frac{1}{2}\epsilon_0\epsilon_{ij}E_iE_j - \frac{1}{2}\mu_0\mu_{ij}H_iH_j - \alpha_{ij}E_iH_j - \frac{1}{2}\beta_{ijk}E_iH_jH_k - \frac{1}{2}\gamma_{ijk}H_iE_jE_k \quad (3.3.1)$$

Differentiation of the free energy leads to polarization

$$P_i(E,H) = -\frac{\partial F}{\partial E_i} \quad (3.3.2)$$

$$= P_i^S + \epsilon_0\epsilon_{ij}E_j + \alpha_{ij}H_i + \frac{1}{2}\beta_{ijk}H_jH_k + \gamma_{ijk}H_iE_k + \cdots \quad (3.3.3)$$

and magnetization.

$$M_i(E,H) = -\frac{\partial F}{\partial H_i} \quad (3.3.4)$$

$$= M_i^S + \mu_0\mu_{ij}H_j + \alpha_{ij}E_i + \beta_{ijk}E_iH_j + \frac{1}{2}\gamma_{ijk}H_iE_j \ldots \quad (3.3.5)$$

The P^S and M^S terms are the spontaneous polarization and magnetization of the material. α represents the induction of polarization in a magnetic field or magnetization by an electric field and is known as the linear ME effect. The terms β and γ are representations of higher order ME effects that are usually ignored. The ME effect then reduces to the ratio of polarization to a magnetic field, or magnetization to an electric field, specifically equation (3.3.6).

$$\alpha = \frac{\bar{P}}{\bar{H}} = \frac{\bar{M}}{\bar{E}} \quad (3.3.6)$$

To get a perfect ME effect, the material must be a single phase, but it is very rare to achieve this, so a composite must be formed. The ME effect arises from a strain mechanism between the two phases in the composite. When an electric field is applied, the piezoelectric phase changes its

volume according to the piezoelectric coefficient e, exerting a force against the ferromagnetic counterpart. The latter is also magnetostrictive, with a piezomagnetic coefficient e^m, and in turn it develops a magnetization as a result of the mechanical strain S, and a polarization is obtained when applying a magnetic field. The ME effect comes from the combination of these effects with a coupling factor, k_c:

$$\frac{\partial P}{\partial H} = \alpha = k_c \cdot e \cdot e^m \tag{3.3.7}$$

Solid combination and sintering of the two phases increase the magnetoelectric (ME) effects, but the material is typically very lossy since the coupling factor is very low [15]. The losses occur because the two phases' boundaries are not matched, causing micro cracks and low material density. To better match the boundaries of the two phases a core shell growth method is proposed. Core shell materials put the FE and FM phases in direct contact with each other without grain boundaries where charge can build up. If the FE and FM phases have well matched lattice parameters, the contact with be even stronger, increasing the coupling factor.

The new material developed on this program attempts to isolate each ferromagnetic particle and surround it with the ferroelectric phase which can be achieved with sol-gel, or hydrothermal synthesis methods. The hydrothermal process was selected rather than the sol gel process for it is readily scalable and single layers can be deposited simply by changing the concentration of the barium hydroxide solution.

3.4 Multi-modal Particle Mixing

The density of a composite is a factor for increasing permittivity, permeability, and voltage strength. The effective permittivity of a composite material is equal to the weighted sum of the logarithm of the permittivity of each separate material of the composite, as seen in equation 3.4.1 [16], where alpha represents the volume percent of each material.

$$\epsilon_{eff} = \prod_{n=1}^{N} \epsilon_n^{\alpha_n} \tag{3.4.1}$$

Mixing powders to form a composite can introduce voids into the solids. Voids lower the dielectric constant of the composite by introducing large volume percentages of low dielectric constant materials, such as air. Air voids can also be the site of breakdown under high voltage. To reduce the number of voids in the composites, mixing multiple particle sizes was investigated.

Furnas proposed a system for combining aggregates of different sizes to increase density of mortars and cements and developed a mathematical model [17, 18]. The models were then

confirmed with experiments done by Anderegg [19]. The following analysis is based on Furnas' model and applied to the material composites. To combine different particles sizes into one aggregate, the materials must be "sized" first. Furnas defines "sized" as a material that passes through one screen but stays on another screen with holes with a factor of $\sqrt{2}$ smaller.

Before beginning packing density analysis, some material variables must be defined. Every material has a material density, denoted here as ρ_{mx} [g/cm^3]. This density does not change with decreased particle sizes as it is an innate physical property of the material structure. When the particles are packed into a container the total volume, V_{Tx} [cm^3], is not completely filled with material. A fraction of the total volume is made up of air pockets, or voids, where the material cannot fill due to the geometry of the particles, and this void fraction is denoted by v_x, and is unitless. With only a fraction of the volume being filled, the material then has an apparent density, ρ_{bx}[g/cm^3], meaning mass of the material, m_x[g], that fills the total volume. This can be calculated using equation 3.4.2.

$$\rho_{bx} = \frac{m_x}{V_{Tx}} \tag{3.4.2}$$

The void fraction of the material can then be found using the relationship between material density and apparent density in equation 3.4.3. Rearranging equation 3.4.3 and solving results in equation 3.4.4.

$$\frac{\rho_{bx}}{\rho_{mx}} = 1 - v_x \tag{3.4.3}$$

$$v_x = 1 - \frac{\rho_{bx}}{\rho_{mx}} \tag{3.4.4}$$

An ideal bimodal system would consist of material with size d_1 [cm] and density ρ_{m1} [g/cm^3] that filled a volume V_{T1} [cm^3], producing a volume fraction v_1. A second material with d_2 [cm] and density ρ_{m2} [g/cm^3] that filled a volume V_{T2} [cm^3], producing a volume fraction v_2 would fill in all the voids produced by material d_1 creating a completely filled composite. This ideal system is never achievable, but mixing particles of differing sizes can increase the composite density significantly.

To maximize the composite density, appropriate fractions of the particle sizes must be determined. The mass fraction of a particle is calculated by the ratio of the particles mass to the total mass of the system, as seen in equation 3.4.5.

$$Z_n = \frac{m_n}{m_n + m_{n+1} + m_{n+2} \ldots} \tag{3.4.5}$$

If a system were made up of only one particle size, the specific volume of the system (SV1) would be determined by the mass fraction, the particle density, and the percent voids with the relationship in equation 3.4.6. A system with two particle sizes would have a specific volume (SV2) determined by the relationship of the same properties seen in equation 3.4.7.

$$SV1 = \frac{Z_1}{\rho_{m1}(1-v_1)} \tag{3.4.6}$$

$$SV2 = \frac{1-Z_1}{\rho_{m2}(1-v_2)} + \frac{Z_1}{\rho_{m1}} \tag{3.4.7}$$

Where these two systems intersect, there is a point of maximum density. Equation 3.4.8 and 3.4.9 combine the two systems and determine the necessary mass fraction needed for this maximized density bimodal system.

$$\frac{1-Z_1}{\rho_{m2}(1-v_2)} + \frac{Z_1}{\rho_{m1}} = \frac{Z_1}{\rho_{m1}(1-v_1)} \tag{3.4.8}$$

$$Z_1 = \frac{\rho_{m1}(1-v_1)}{\rho_{m1}(1-v_1)+v_1\rho_{m2}(1-v_2)} \tag{3.4.9}$$

Assuming both particles in the bimodal system have a void percentage of .3 and the same density of 1 g/cm^3, the bimodal specific gravities can be illustrated, as in Figure 1. The intersection point is the maximized density of a bimodal system.

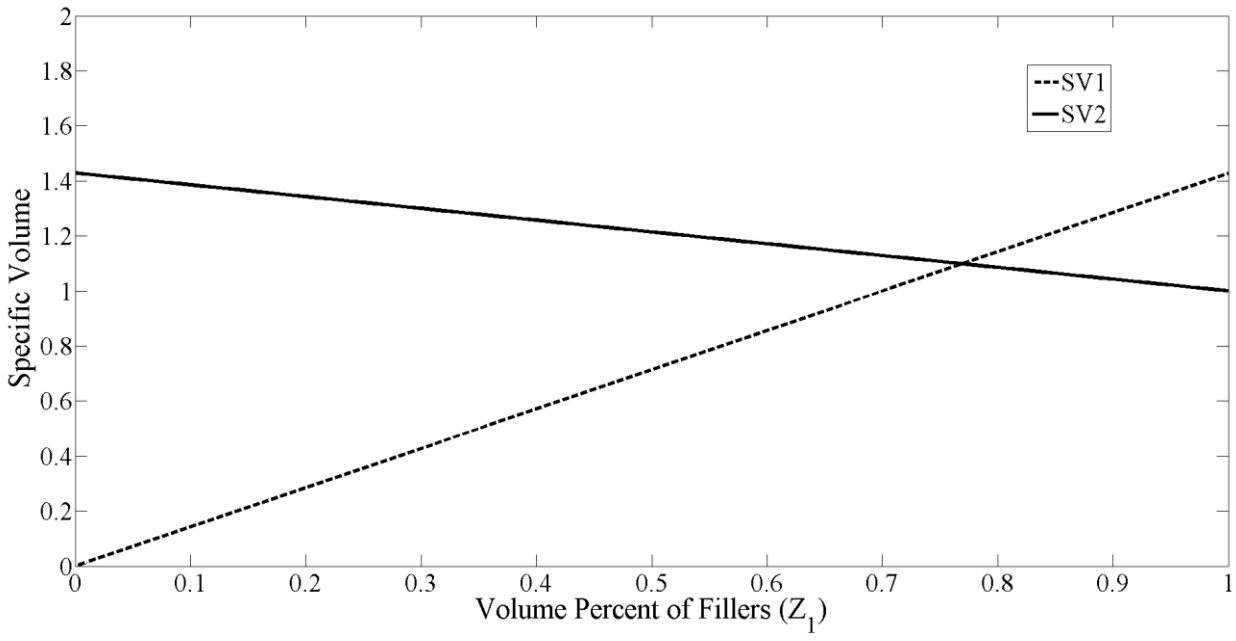

Figure 1: Furnas Specific Volume Relationship

Furnas extended these same principles to aggregates that combined more than two particle sizes, specifically a trimodal system with three sizes. The same principles of void fractions and material densities apply to all the materials, but the dimensions of the materials are of more interest. Furnas makes the assumption that the density of all the materials is the same, as is the void percent. This assumption leads to the conclusion that the size of the particle necessary for maximum composite density is a ratio of large to small sizes (equation 3.4.10). If the largest and smallest particle sizes are known, the middle size can be determined by equation 3.4.11.

$$\frac{d_2}{d_1} = \frac{d_3}{d_2} = \frac{d_{n+1}}{d_n} \tag{3.4.10}$$

$$d_2 = \sqrt{d_1 d_3} \tag{3.4.11}$$

Using the same assumptions of equal densities and void percentages, the same ratio of particle sizes can be applied to the mass fractions (equation 3.4.12). This can then be solved for the mass fraction for any sequential particle size, as seen in equation 3.4.13.

$$\frac{Z_2}{Z_1} = \frac{Z_3}{Z_2} = \frac{Z_{n+1}}{Z_n} \tag{3.4.12}$$

$$Z_x = (1 - Z_1)\left(\frac{1-Z_1}{Z_1}\right)^{x-2} \quad (3.4.13)$$

When all the mass percentages are combined, the total percent is over 100%, so the final ratios must be normalized.

If we now look at a system where the largest and smallest particle sizes are fixed, the issue of finding the maximum possible density of that system is one that determines the number of intermediate sizes of particles to include in the composite. As more component sizes are added to the system the total volume of the system, S, increases but the value of the volume of the packing factor, y, decreases. Therefore, we are dealing with two competing factors for finding a maximum value of Equation 3.4.14.

$$D = \frac{G_a}{1-\frac{y(S-Z)}{S}} \quad (3.4.14)$$

This competition can be resolved by introducing a new variable, n, that represents the number of component sizes added to the system of only large particles. To find the number of particle sizes needed to maximize the density we need note that Equation 3.4.14 is a maximum when the quantity $\frac{y(S-Z)}{S}$ is a maximum. So by differentiating this quantity with respect to n the maximum density of the system can be determined. Therefore,

$$\frac{d\left[\frac{y(S-Z)}{S}\right]}{dn} = \frac{\frac{yd(S-Z)}{S}}{dn} + \left(\frac{S-Z}{S}\right)\left(\frac{dy}{dn}\right) \quad (3.4.15)$$

Now, setting Equation 3.4.15 equal to zero we have

$$\left(\frac{Z}{S(S-Z)}\right)\frac{dS}{dn} = -\frac{dy}{ydn} \quad (3.4.16)$$

In order to completely define Equation 3.4.16 it is necessary to solve for the quantities S and y in terms of the system variables Z, V, n, d_n, where d_i is the diameter of particle size i. Solving S in terms of the system variables is a matter of noting that S is equal to the right hand side of Equation 3.4.17**,** which is a geometrical progression. The general form of this progression is seen in equation 3.4.18.

$$T = \frac{1+V+V^2+V^3\ldots}{1+V} \quad (3.4.17)$$

$$S = \frac{1-V^{n+1}}{1-V^2} \tag{3.4.18}$$

Where, in order to be consistent with the definition of n, the exponent n+1 is the total number of particle sizes in the system.

The factor y must be determined through experimental means. However, y represents the ratio of the decrease in the total volume of the system upon mixing to the volume decrease if infinitely small particles were used. Therefore, we know y must vary as some function of the diameter of the smallest particle size. If the diameter of the smallest particle size in the system is d_{n+1} and the diameter of the largest particle size d_1, then the ratio between these sizes can be given by

$$K = \frac{d_{n+1}}{d_1} \tag{3.4.19}$$

As discussed previously the percentage of voids in a system of sized material is independent of the size of the particles as long as the density of each particle size is the same if the container for the particles is really small. This means the ratio between successive sizes for maximum packing in one part of the system is the same in any other part of the system. So in an ideal system

$$\frac{d_2}{d_1} = \frac{d_3}{d_2} = \frac{d_{n+1}}{d_n} = K^{\frac{1}{n}} \tag{3.4.20}$$

where $K^{\frac{1}{n}}$ is the ratio between adjacent sizes. The value for y was given by Furnas in his 1929 paper [17]. In this paper, he describes the value of y as

$$y = 1.0 - 2.62K^{\frac{1}{n}} + 1.62K^{\frac{1}{n}} \tag{3.4.21}$$

which can be differentiated with respect to n to give

$$\frac{dy}{dn} = \frac{2.62K^{\frac{1}{n}} \ln K}{n^2} - \frac{3.24K^{\frac{1}{n}} \ln K}{n^2} \tag{3.4.22}$$

Using these equations, we can now calculate how the density of a system of packed particles changes for given values of K, V, and n. Figure 2, Figure 3, and Figure 4 show how the percentage of voids in the system decreases with a decrease in K for V values of 30%, 40%, and 50% respectively.

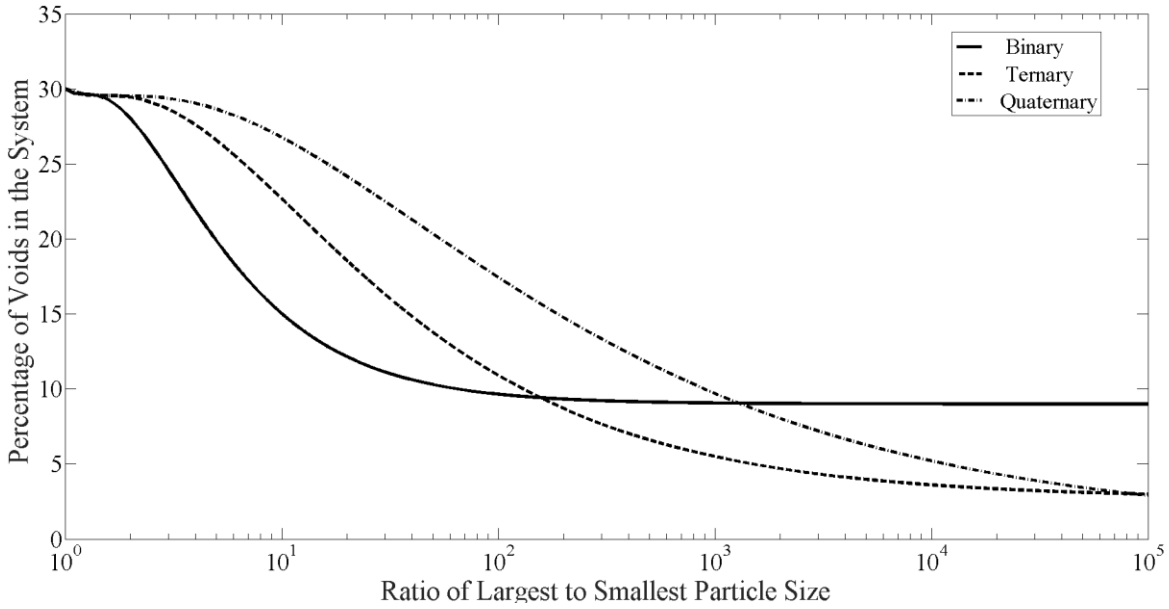

Figure 2: Percentage of Voids in a system of packed particles as a function of the ratio between the largest and smallest particles size when the void percentage of the unpacked system is 30%

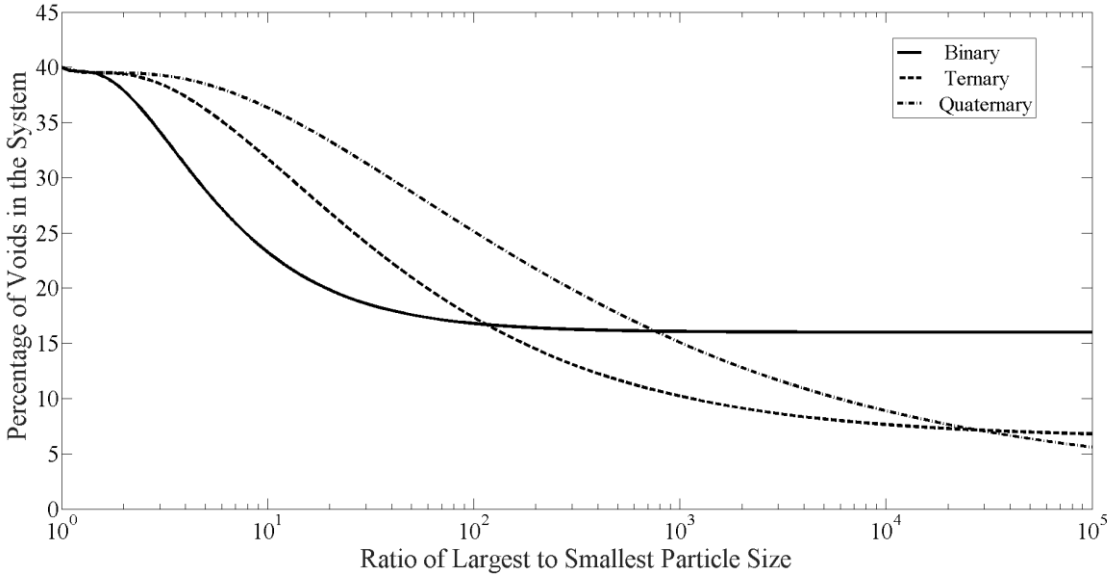

Figure 3: Percentage of Voids in a system of packed particles as a function of the ratio between the largest and smallest particles size when the void percentage of the unpacked system is 40%

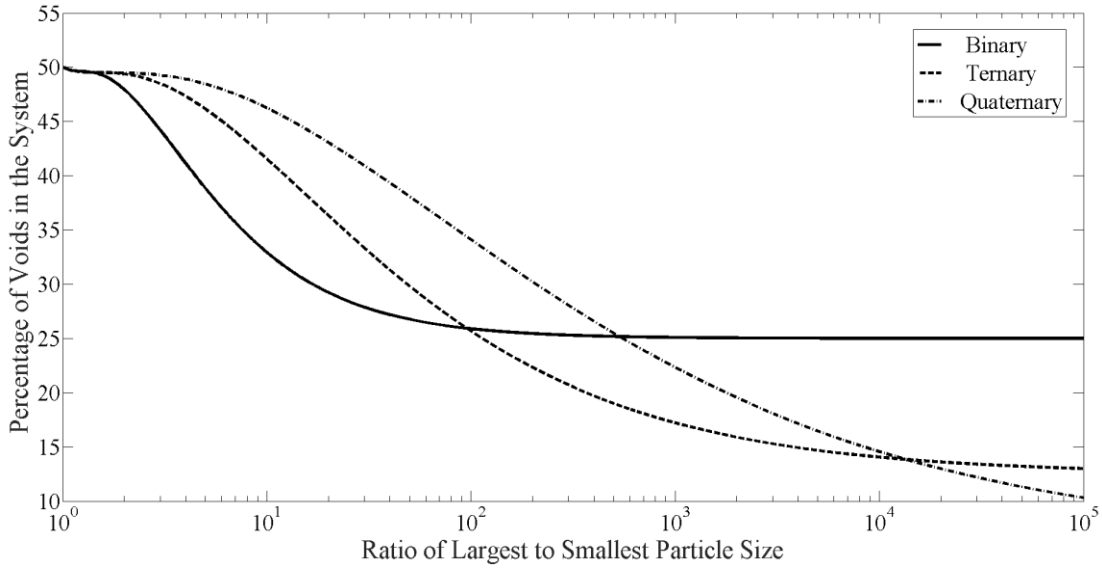

Figure 4: Percentage of Voids in a system of packed particles as a function of the ratio between the largest and smallest particles size when the void percentage of the unpacked system is 50%

It is apparent from review of these figures that as the size difference between the largest sized particles and smallest sized particles increases, we see a general reduction in the percent of the system volume that could be considered void. It is important to note two key points however. First, we see that in all three figures the void percentage in binary system stabilizes when the large particles are about $7\ to\ 10$ times larger than the smallest particles. Beyond this point there is no noticeable benefit in increasing the size differential further. Second, the particle size differential determines the number of particle sizes needed to achieve maximum density. Below $7\ to\ 10$ for a binary system is best. Between $7 to 10$ and 10^4, a ternary system gives the maximum possible density. Above 10^4 a quaternary system starts to have the advantage, especially for systems with higher initial void percentages.

From the preceding discussion, a general algorithm can be developed for creating a composite system of maximum density. This algorithm is outlined as follows: First the size of largest and smallest particles are selected, then the particle size differential and initial volume percentage of voids are calculated; these data are used to reference Figure 2, Figure 3, and Figure 4 to determine the number of intermediate particles needed, and finally Equation 3.4.11 allows the calculation of the diameter of each intermediate size.

For the composites developed in this work, the maximum particle size attainable was 35 μm, and the minimum available was 100 nm. Using equation 3.4.11, the middle particle size was determined to be 1.87 μm. Table 1 shows the material and apparent densities of the ferrite and barium titanate ferrite composite powders and their resulting void percentages. These were then used to determine the necessary mass percentages presented in Table 2 and Table 3.

Table 1: Particle Densities and Void Percentages

Particle Size [μm]	Material Density [g/cm^3]	Apparent Density [g/cm^3]	Void Percent
Ferrite: 35	4.60	2.106	0.542
Ferrite: 3 ·	4.60	1.584	0.656
Ferrite: 100 ·	2.81	0.374	0.867
BTF: 35 ·	4.91	1.765	0.641
BTF: 3 ·	4.04	1.684	0.583
BTF: 100 ·	3.39	1.342	0.604

Table 2: Bimodal Composite Mass Percentages

Material	Z_1	Z_2
Ferrite	0.866	0.134
BTF	0.683	0.317

Table 3: Trimodal Composite Mass Percentages

Material	Z_1	Z_2	Z_3
Ferrite	0.6358	0.2588	0.1054
BTF	0.5042	0.3078	0.1880

4. Material Synthesis and Testing Material Preparation

4.1 Powder Preparation

The ferrite material that is used to make both the ferrite composites and the barium-titanate ferrite composites (BTF) is purchased as a solid core piece. Ceramic Magnetics, Inc. makes the nickel-zinc ferrite and sells them as large cubic or toroidal cores. The primary ferrite used in the

BTF composites is the C2050 ferrite that has a bulk relative permeability of 100 and density of 4.6 g/cm^3. This same ferrite was used in the production of the ferrite composites, to keep a constant material for comparison of material properties.

The solid cores had to be broken down into the specific particle sizes necessary to fabricate the composites. First, the solid ferrite blocks were broken into smaller, more manageable chunks using an air hammer. This tool uses compressed air to force the tool head to move similar to a jackhammer. After the cores had been fractured into smaller pieces, these were sealed in vacuum bags and pressed between steel plates of a hydraulic press. This process broke the ferrite into even smaller pieces, about 1 to 5 cm in length. The small ferrite pieces were then placed in granite jars with milling balls and milled for 45 minutes in a planetary mill. The planetary mill seen in Figure 5 can hold up to four grinding jars and uses a wheel to move the grinding wheels in the opposite direction of the milling balls inside the jars. This allows for optimal grinding and significant size reduction and takes the ferrite material from small chunks to small powders.

Figure 5: Planetary Ball Mill

The powders are separated into specific size ranges using metal sieves. The sieves were originally placed on a sieve shaker that used vibrational motion to shake the powders through the different sizes. This process was efficient, but it could not separate particles with a diameter below 45 μm consistently and the size range needed to make the composites was between 45 and 25 μm. A sonic sieve system was then adopted to separate the smaller particle sizes. The sonic sieve (Figure 6) uses speakers that apply a vibration at 60 Hz as well as mechanical taps to move the particles through the different sieves. The only drawback of this system is the large amount of

noise that is generated by the speakers. The sonic sieve was moved to an isolated trailer separate from the lab to reduce noise and keep the material preparation in one space.

Figure 6: Sonic Sieve

The 45 μm to 25 μm particle size range was fabricated using the milling and sieving procedure. Any particles that were smaller than 25 μm were assumed to be within the <5 μm size range needed for the medium particle size. This was not a sound assumption, as was confirmed later using SEM analysis. The particles ranged anywhere from 15 μm to 1 μm in diameter and most were on the large end of the spectrum. Ceramic Magnetics, Inc. was then contracted to provide the medium particles without having to mill and sieve the particles further in the lab.

The nanometer particles could not be fabricated in the lab without intense milling or chemical synthesis. It was decided that purchasing nanometer ferrite would be more time and cost effective. The nanometer ferrite used in the composites is 100 nm Nickel-Zinc Iron Oxide from Sigma Aldrich. This ferrite has a density of 2.81 g/cm^3 which is about half of the density of the other particle sizes. This change in density does make a difference in some particle properties of the

bimodal and trimodal mixed composites, but was the only powder available given the program schedule.

4.2 Chemical Synthesis of Core-Shell Material

To increase the permittivity of the metamaterials, additional layers of dielectric material were chemically developed around the ferrite cores. Two chemical methods were investigated to synthesize the barium titanate layers. The first process involved volatile chemicals and fast pressurized reactions, while the second used inexpensive materials reacted at lower temperatures for a longer amount of time.

This first chemical synthesis process used titanium-IV chloride ($TiCl_4$) and barium nitrate ($Ba(NO_3)_2$) as precursors for the barium titanate and was based off a similar reaction from "Hydrothermal synthesis and properties of NiFe2O4@BaTiO3 composites with well-matched interfaces"[20]. To produce barium titanate ($BaTiO_3$) with this method a 1:1.8 molar ratio of titanium and barium was needed. The $Ba(NO_3)_2$ is the limiting reactant in this reaction so it was used to calculate the amount of chemicals needed. It was mathematically determined that 2.1 g of $Ba(NO_3)_2$ and 1.563 g of $TiCl_4$ would be reacted. The $TiCl_4$ is highly reactive to water, including water in the air. When it reacts with water the $TiCl_4$ creates a toxic hydrochloric gas. To limit this reaction and create a safe laboratory environment, the $TiCl_4$ was isolated in a nitrogen filled bag (Figure 7) and dissolved in ethanol. Not all of the water could be removed from the air inside the containment bag so some HCl gas was generated, but was isolated from the laboratory given the enclosure procedures used during the process (Figure 7).

Figure 7: Nitrogen Isolation Bag

Once the titanium is dissolved into ethanol it is no longer reactive. The $Ba(NO_3)_2$ was dissolved into water and then combined with the dissolved $TiCl_4$. Sodium hydroxide is a strong base that was added to the dissolved titanium and barium to decrease the reaction time and allow the reaction to favor the products over the reactants. Ferrite was combined with the dissolved ions and the mixture was placed in a high-pressure reaction chamber, as seen in Figure 8. This chamber was heated to 350 °C with a ceramic heating ring and temperature controller that was monitored with a high-temperature probe inserted into the reaction chamber. This reaction was done inside a pressure vessel since one of the byproducts of the reaction is chlorine gas, nitrogen gas, and oxygen which increased the pressure as the reaction progressed. Keeping the reaction under pressure also decreased the necessary reaction time. The whole reaction was completed in 6 hours. The powder produced was then rinsed with water multiple times to lower the pH to 7 and remove the unreacted ions out of the solution and on the surface of the particles. The powders were then dried with vacuum filtration.

Figure 8: High-Pressure Reaction Vessel

The second process used titanium dioxide (TiO_2) and barium hydroxide octahydrate ($Ba(OH)_2 * 8H_2O$) as precursors for the barium titanate and is based off a barium titanate synthesis reaction from [21]. This reaction used a 1:1 molar ratio of barium and titanium so the TiO_2 and

$Ba(OH)_2$ are both the limiting reactants. Both chemicals are in powder form and are soluble in water, so 19.75 g of $Ba(OH)_2$ and 5 g of TiO_2 are combined with 4 g of ferrite and mixed into 40 mL of water. The solution is then reacted in a stirring water bath (Figure 9) that is heated to 90 °C for 72 hours. The stirring motion keeps the ferrite particles from settling to the bottom of the solution and allows the barium titanate to form around them. The final product is rinsed with water and acetone to clean the excess unreacted ions from the powder and then vacuum filtered to dry. When large amounts of the BTF composite powder are synthesized, the drying method creates large pieces of the product and must be milled and sieved to be deagglomerated. The same method of milling and sieving the ferrite powders is used to break up the synthesized BTF powders.

Figure 9: Stirring Water Bath

The two processes produce the same barium titanate ferrite powder through very different methods. The first reaction is faster, but uses much more volatile reactants that are also more expensive. The reaction is also limited by the space of the pressure chamber. The second reaction takes more time, but the reactants are easy to handle and less expensive. The water bath also allows for more powder to be produced at one time. After confirming that the products of the reactions were the same with scanning electron microscopy (SEM) and electron dispersive spectroscopy (EDS) the first reaction was no longer used to produce the BTF powders. The second reaction was determined to be more cost and time effective due to the scalability of the product.

4.3 Preparation of Test Composites

The ferrite and BTF powders must be made into solid composites to test specific material properties such as permittivity, permeability, and voltage breakdown strength. To prepare these composites, the powders are combined with a dielectric, silane-based binder and are pressed into solids using a hydraulic press.

The binder is a unique polymer that is used to add another layer of dielectric material to the composites. It holds the powders together while they are under pressure and creates a strong polymer matrix that also increases the voltage strength of the materials. This addition makes the powders into metamaterial composites and alleviates the need for additional sintering to strengthen the mechanical hardness of the composites.

Before the binder can be added to the powders, the binding sites of the polymer must be activated. This is achieved by combining the binder with water and heat generating an evaporation reaction that separates the excess ethanol from the binding reagent. Once activated the binder is combined with the powders in specific ratios depending on the size of the test solids.

When the powders are combined with the binder, a Resodyn acoustic mixer is used to ensure adequate coating and mixing of the composite. The mixer uses sound waves to match the resonant mixing frequency of the materials in the composite. This mixing method allows for quick, high intensity mixing without stirring bars or added heat.

For the high-voltage strength tests, 2.54 cm diameter discs were fabricated. These discs consist of 6 g of powder and 3 mL of the binder. This mixture is combined using the Resodyn acoustic mixer for 2 minutes. The composite is then placed inside a steel 2.54 cm diameter die and placed in a hydraulic press. Prior to adding the material to the die, the base and plunger are sprayed with a boron-nitride mold release spray that keeps the material from binding to the inside of the die. The material is then pressed to ensure maximum density of the composite. Some of the excess binder is pressed out in this process. The composite is held under pressure for 15 minutes and then removed from the die and placed in a 100 °C oven for 24 hours. The heat cures the binder, removes any excess water, and increases the density of the composite further.

Test samples for the permittivity and permeability measurements are made in a similar fashion, but a 7 mm diameter die is used and 3 g of material is mixed with 1.5 mL of binder. This composite is only pressed with a few tons of pressure. For the permittivity and permeability measurements, a 3 mm hole must be drilled through the 7 mm discs to hold the center conductor of the airline used for measurements. This is done using a mini-lathe that bores a 3 mm hole while turning the material

instead of the drill bit. Figure 10 shows a 7 mm disc that is pressed and then processed with the lathe to make the 3 mm center hole.

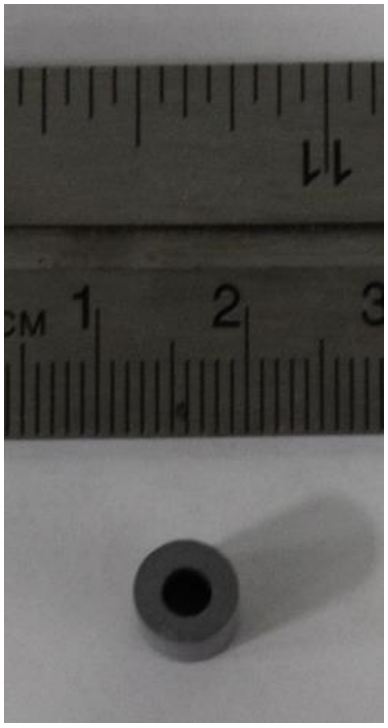

Figure 10: Photograph of 7 mm test disc

The high-voltage tests require an electrode to be placed on the test material. Before applying the electrodes, the composites must be surfaced and polished. A CNC mini-mill is used to take off incremental layers of the 2.54 cm discs. The discs are held in the CNC mill with a vacuum chuck, and then the mill is programmed to cut in a circular motion to reduce stress on the material. The composites are milled to different thicknesses depending on the desired test. This process is done to each side of the discs to ensure they are level. The composites are then polished by sanding each side with increasing grit sandpaper. The sandpaper utilized starts with 220 grit, followed by 600, then 2000, and polishing is then completed with 12,000 grit paper. Once polished, platinum electrodes are sputtered onto the test discs with a sputter coater. Then a layer of conductive silver paint is added to increase the conductivity of the electrodes. To ensure even coating of the silver electrodes, an air brush system is used. The electrodes are then cured in a vacuum oven for at least 4 hours. Figure 11 shows a 2.54 cm test disc with electrodes applied.

Figure 11: The 2.54 cm test disc with electrodes

5. Test and Measurements

5.1 Scanning Electron Microscopy

To confirm particle sizes and the synthesis of the barium titanate ferrite composites, scanning electron microscopy (SEM) was used. The SEM generates an electron beam that interacts with the sample and generates images from the electron-sample interaction. The most useful images come from secondary electrons that are generated when the electron beam excites the atoms in the sample. The secondary electron detector, usually an Everhart-Thornley detector, can ascertain the angle of electron motion and the energy at which they are excited and forms an image based on these characteristics. The electrons are first attracted by a bias-grid and then accelerated using a scintillator [22]. This energizes the electrons enough to construct an image. Another useful image can be constructed from back-scattered electrons. These electrons are generated by the electron beam, but are backscattered towards the detector from elastic collisions with the sample. Elements with higher atomic number create more collisions and appear brighter in the back-scattered image.

A separate detector is used for these electrons since they have a higher energy than secondary electrons [23].

Electron dispersive spectroscopy (EDS) can be used in combination with SEM to determine the atomic makeup of samples. The EDS analysis uses the same electron beam in the SEM to excite the samples. When the secondary electrons are emitted from the sample, electrons from a higher atomic level drop into the hole created from the emitted electron and release x-rays. The energy of the x-ray is dependent on the material that it is emitted from [24]. An x-ray detector analyzes the emitted x-ray energies and generates an atomic spectrum.

The SEM images of the BTF composites show larger, jagged pieces of ferrite surrounded by spherical nanometer size particles of barium-titanate. Figure 12 and Figure 13 show the BTF composites with secondary electrons and backscattered electrons. The back-scattered images are more distinct since iron and titanium are heavier atoms that scatter more electrons rather than emitting secondary electrons. Figure 14 confirms the existence of barium titanate surrounding ferrite particles using a 4-point EDS analysis. Points 1 and 4 in the image correspond to the spectra showing iron (Fe), nickel (Ni), zinc (Zn), as well as some titanium (Ti) and barium (Ba) indicating these particles are nickel-zinc ferrite with some barium titanate layered on top. Points 2 and 3 in the image correspond to the spectra with large peaks of Ti and Ba indicating areas of barium titanate. Oxygen is present in both ferrite and barium titanate compounds but cannot be detected well with EDS.

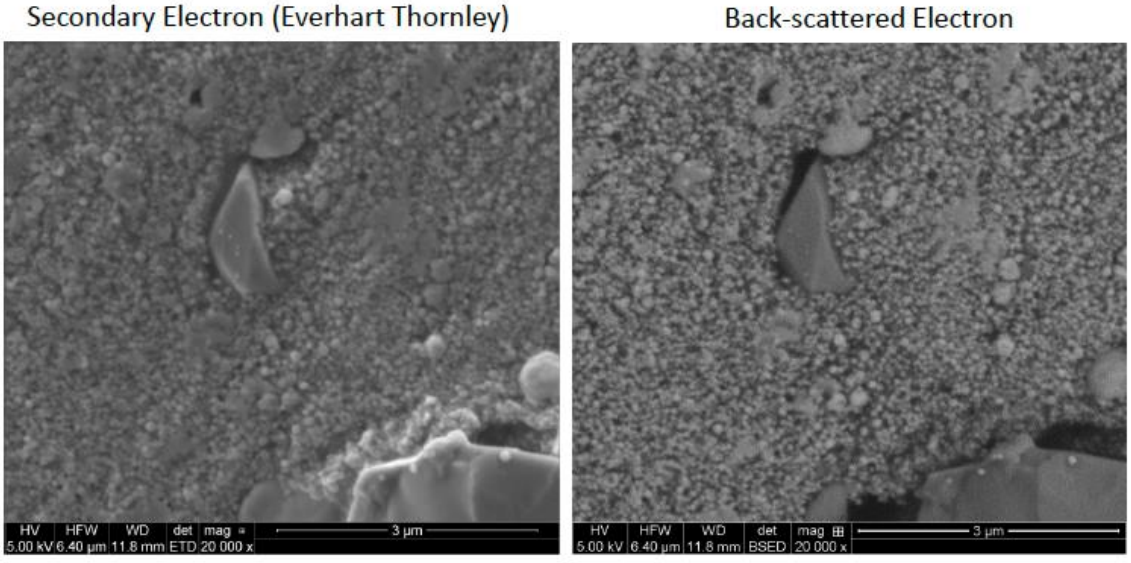

Figure 12: SEM image of 3 µm BTF Composite Sample

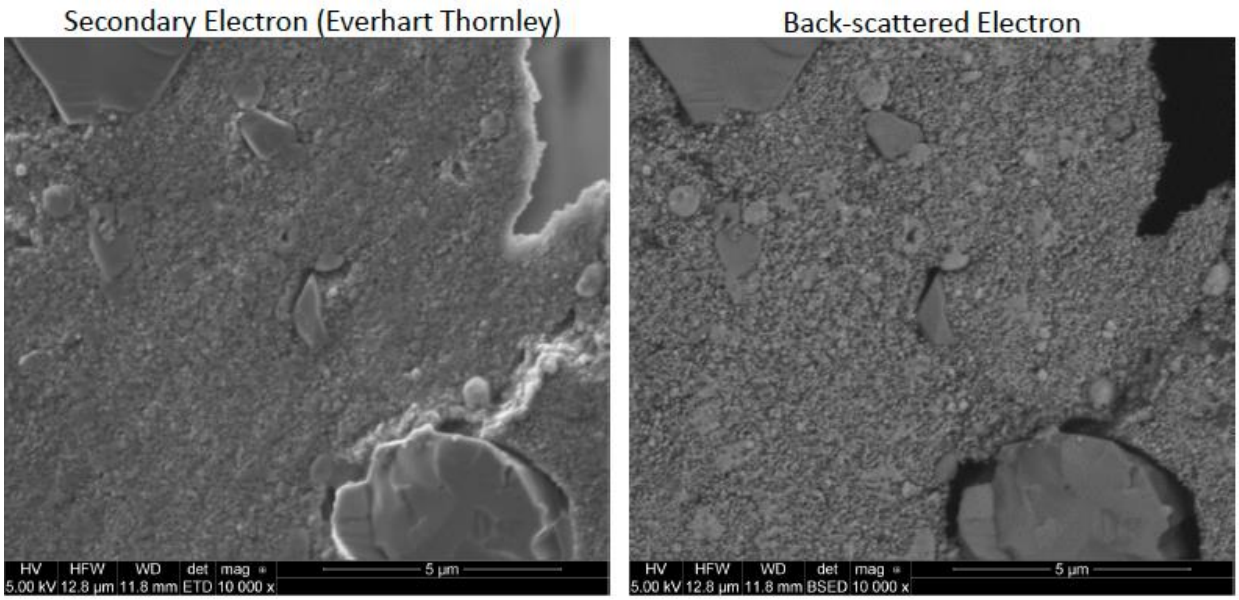

Figure 13: SEM image of 5 μm BTF composite sample

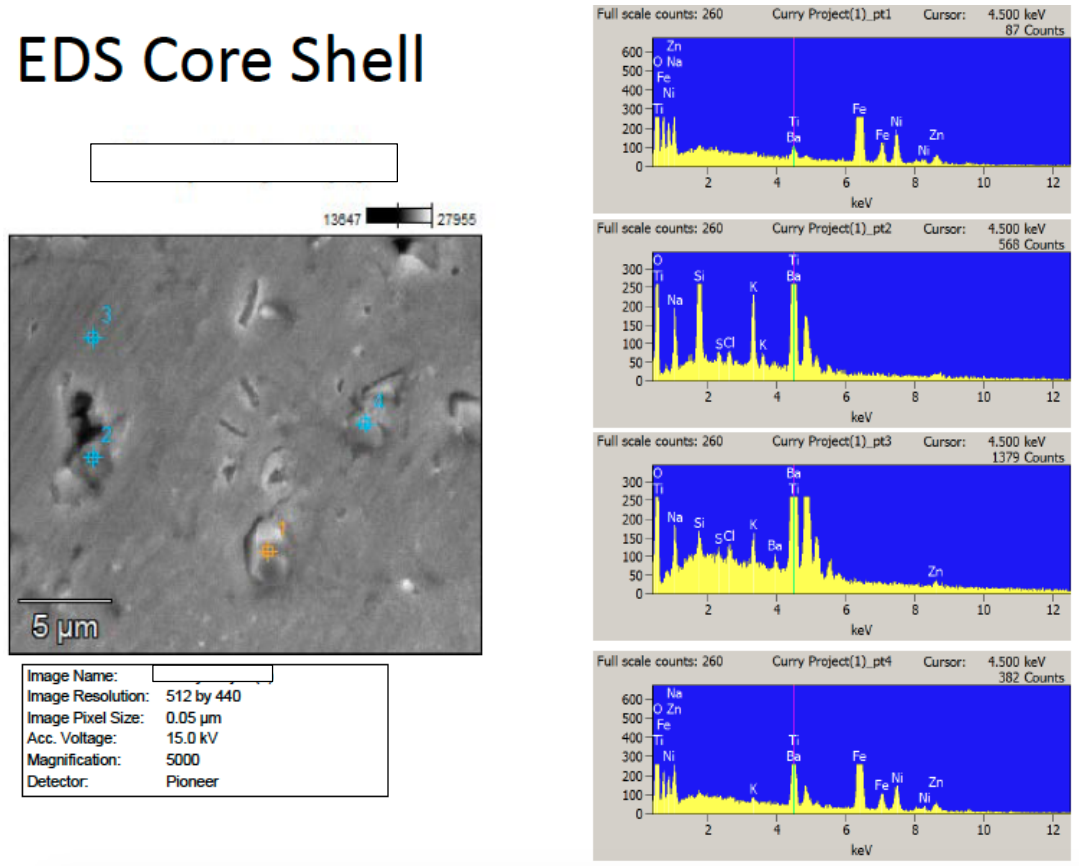

Figure 14: EDS 4-point SEM Analysis

Transmission electron microscopy (TEM) is another form of microscopy for more detailed imaging of small complex samples. The TEM uses an electron beam similar to SEM, but instead of only reacting with the surface of the sample it passes through specially prepared specimens and creates an image based on the electrons passing through the sample. The TEM samples are prepared by slicing very thin layers of the desired structure with a diamond knife and then placing the layers in the TEM chamber. The electron beam then passes through the specimen and the electrons are collected on the other side of the slice by a detector or fluorescent screen to form the image [25]. This kind of spectroscopy allows for more detailed images and has the ability to collect information about the bulk of the material.

To prepare the BTF composites for TEM, the particles had to be suspended in a resin, cured, and then sliced with a diamond knife. Figure 15 shows a TEM image of the BTF composites. The hardness of the ferrite and barium titanate in comparison to the resin created a few holes in the

slices when cut with the diamond knife. These holes can be seen as light spots in the image, so the benefits of TEM imaging could not be applied to the composites.

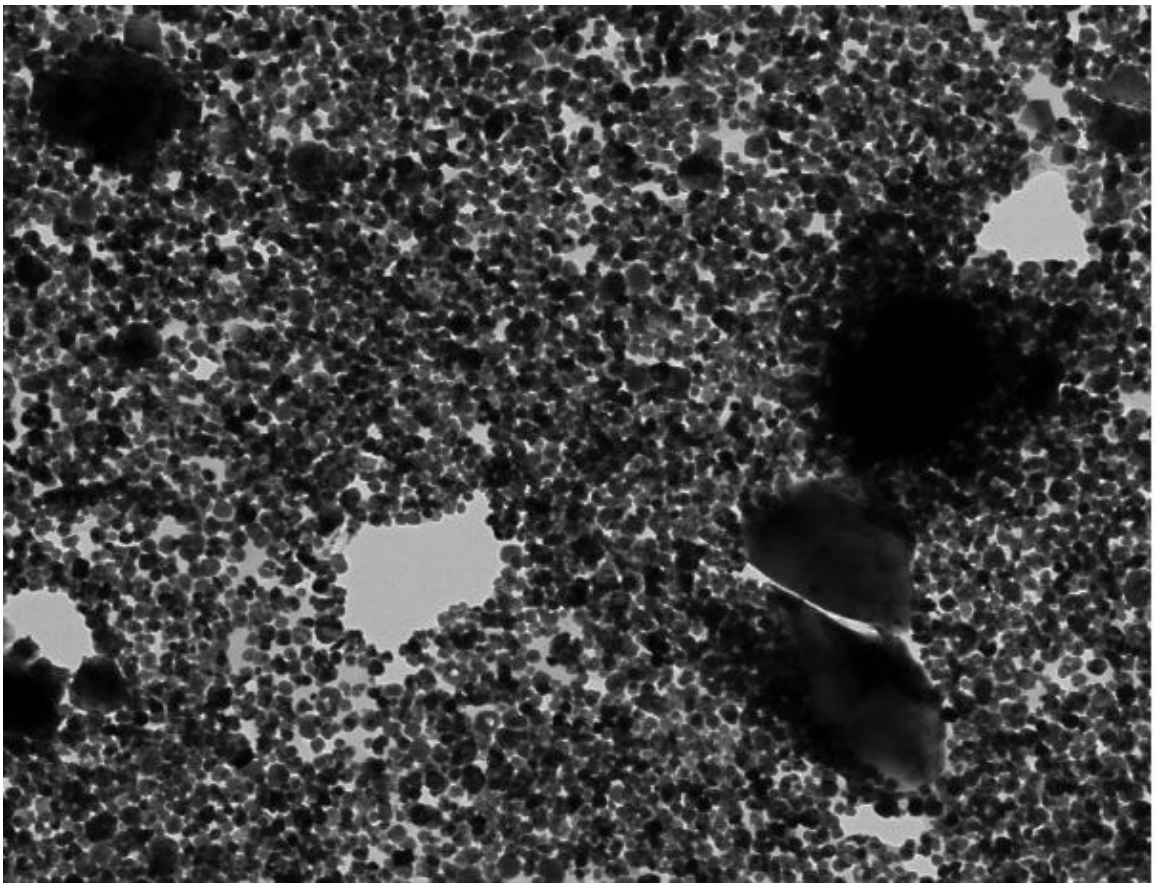

Figure 15: TEM image of BTF Composite in Resin

5.2 Inductively Coupled Plasma Atomic Emission Spectroscopy Analysis

Inductively coupled plasma atomic emission spectroscopy (ICP-AES) analysis was performed on the barium-titanate ferrite composites. ICP-AES analysis generates a plasma with an RF source in argon consisting of high-energy charged particles. A sample, which has been dissolved into liquid form, is added to the plasma with a nebulizer and immediately collides with the charged particles breaking the sample into ions as well. When the ions recombine with electrons in the plasma, light spectrums that correspond to the constituent metals can be measured and identified. The energy of the radiation or light is indicative of the type of atoms in the sample and the ratio of that atom in the sample [26].

Analysis was done on each particle size (100 nm, 5 μm, and 45 μm) to determine the amount of barium titanate that is synthesized during the hydrothermal reaction. The solid particles had to be dissolved into a liquid to be nebulized into the plasma. This step meant that the powders had to be digested with sulfuric acid since the samples were heavier metals. Table 4 shows the elemental analysis of each size and the amount of elements detected in parts per million (ppm). Barium is hard to detect with ICP-AES done with sulfate digestions, so the results were not conclusive. In each size sample the amount of titanium detected is similar, so the same amount of barium titanate can be measured and is not dependent on the particle size. The amount of barium titanate may be the same, but the thickness of the layers will not be the same due to the different surface areas.

Table 4: ICP-AES Elemental Analysis of different BTF particle diameters

Mean concentration	A - 30 nm	B - 5 μm	C - 45 μm
Fe	89440.85	87657.07	73903.85
Ni	21554.16	23772.86	19805.20
Zn	29180.65	12490.82	10989.48
Ti	145584.78	125582.52	141379.99

5.3 Relative Permittivity and Permeability Measurement

In order to calculate the frequency dependent relative permittivity and relative magnetic permeability of the composites, an algorithm described by Nicolson, Ross, and Weir was used to interpret the results of the measurements [27][28]. As part of this algorithm a low power voltage pulse is sent through a cavity that contains a sample of the material to be tested. Figure 16 shows a diagram of this setup.

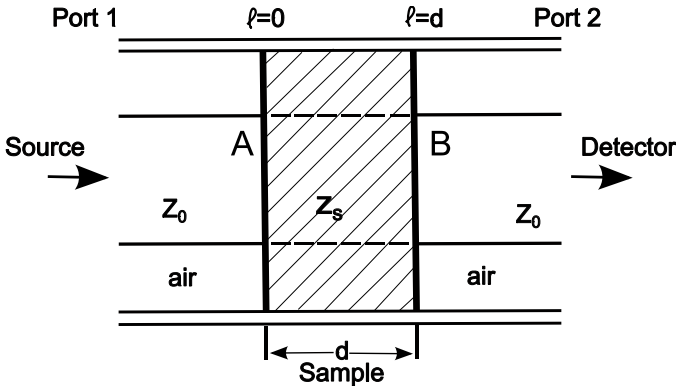

Figure 16: Representation of a sample material in a cavity.

This pulse is partially transmitted and partially reflected when it enters and exits the material. Two ports are connected to either side of the cavity and measure the magnitude and phase of the voltage pulse received. These results are used to calculate the time dependent scattering parameters $S_{11}, S_{21}, S_{22}, S_{12}$. A Fourier transform is used to convert these parameters to their frequency dependent forms. It is from these frequency dependent scattering parameters that the relative permittivity and permeability can be calculated [27][28].

The cavity used for these tests was a Type-N 50Ω Keysight coaxial airline. The airline model used in the experiments is shown in Figure 17.

Figure 17: Type-N 50Ω Keysight Airline and corresponding center conductor that was used for high frequency measurements.

This airline required disks with an outer diameter of 0.7cm and inner diameter of 0.3cm.

5.3.1 Determination of Optimal Sample Length

The length of the samples were chosen to be 0.8 cm. This length was chosen due to the fact that the Nicolson-Ross-Weir method is known to become unstable at frequencies that equal multiples of one-half the wavelength in the material. In order to reduce this instability, the sample can be reduced in length but at the expense of measurement resolution [29]. It is also known that the error of measurements depends on the magnitudes of S_{11} and S_{21} [28]. Since the magnitude and phase values are optimized for a $S_{11}\omega$ approaching 1, we need to maximize $S_{11}\omega$. By utilizing $\frac{(2n+1)\lambda_m}{4}$ transformer effects, where λ_m is the wavelength in the material, the maximum value of $S_{11}\omega$ occurs when the length of the sample is $\frac{\lambda_m}{4}$. The wavelength in the sample material can be calculated for a dispersive waveguide by

$$\lambda_m = Re\left(\frac{1}{\sqrt{(\epsilon_r\mu_r/\lambda_0^2)}} - \frac{1}{\lambda_c^2}\right) \qquad (5.3.1.1)$$

which for a coaxial geometry $\lambda_c = \infty$:

$$\lambda_m = Re\left(\frac{\lambda_0}{\sqrt{\epsilon_r \mu_r}}\right) \quad (5.3.1.2)$$

It was experimentally determined that a length of 0.8 cm allowed for test and measurement of the samples between the frequencies of 20 MHz and 4 GHz with minimal errors and no instabilities. This range was selected to highlight the frequencies that are most applicable for the intended application of the developed material.

5.3.2 Ferrite Continuous Distribution

Samples with ferrite only and no ceramic coating were tested with a continuous distribution. We tested five different ferrites labeled MMU1-MMU5 as shown in Figure 18 and Figure 19. Table 5 shows the nickel-zinc ferrite material from CMI that corresponds to the composites fabricated and Appendix A contains the material data sheets. Based on these tests for the barium titanate tests we down selected the two most promising materials. Figure 18 shows the dielectric constant of each material and Figure 19 shows the corresponding loss tangents. The ferrite particles when interconnected with the silane network produced a dielectric constant that was relatively high for a composite and stable across the entire frequency band. We believe that this result is due to the dielectric properties of the ferrite lattice. Figure 19 shows that the real part of the relative permittivity is also dominant over all frequencies tested.

Table 5: CMI Ferrite Key

Composite Identification	CMI Ferrite
MMU1	C2050
MMU2	C2075
MMU3	CMD5005
MMU4	N40
MMU5	XCK-14

Figure 20 and Figure 21 show the results for μ_r' and the magnetic loss tangent respectively for each type of metamaterial composite. Since each material was optimized for its magnetic content, the magnetic response over the tested frequency range is very similar to that of a bulk ferrite material. Above 1 GHz, the imaginary part of the relative permeability becomes dominant. The

values of ϵ_r' and μ_r' along with Equations 3.3 and 3.4 were used to calculate both the impedances as well as the relative wave velocity of each material.

$$V = \frac{c}{\sqrt{\epsilon_r \mu_r}} \qquad (4.3.2.1)$$

$$Z_m = Z_0 \sqrt{\frac{\mu_r}{\epsilon_r}} \qquad (4.3.2.2)$$

The results are shown in Figure 22 and Figure 23. The impedances are within 50% of free space up until about 2 GHz, following a similar curve to μ_r'. At this frequency we observe a relative wave velocity of between .13 and .06 corresponding to a size reduction factor of between 7.7 and 16.7.

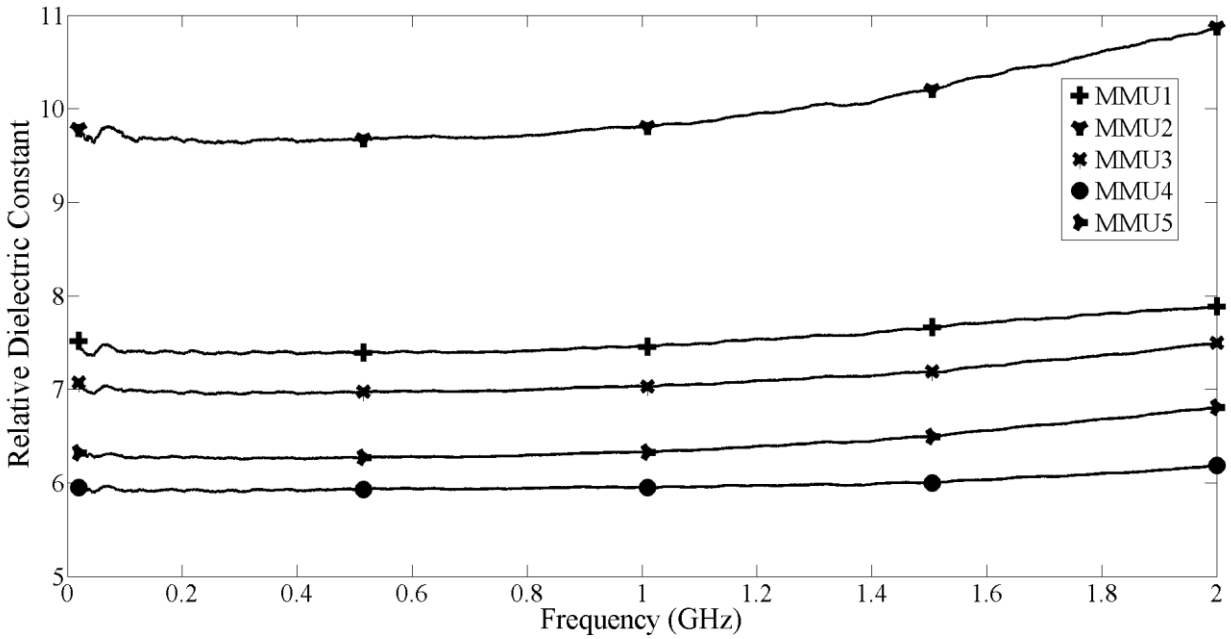

Figure 18: Relative permittivity as a function of frequency for each of the five ferrite composites.

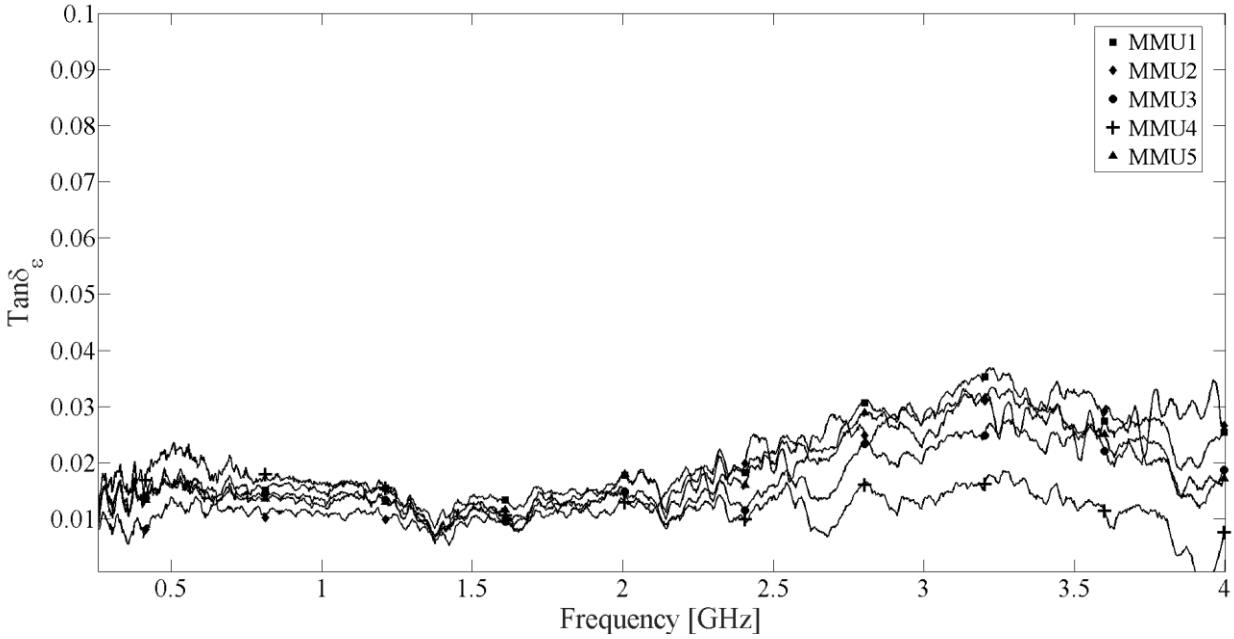

Figure 19: Dielectric loss tangent as a function of frequency for each of the five ferrite composites.

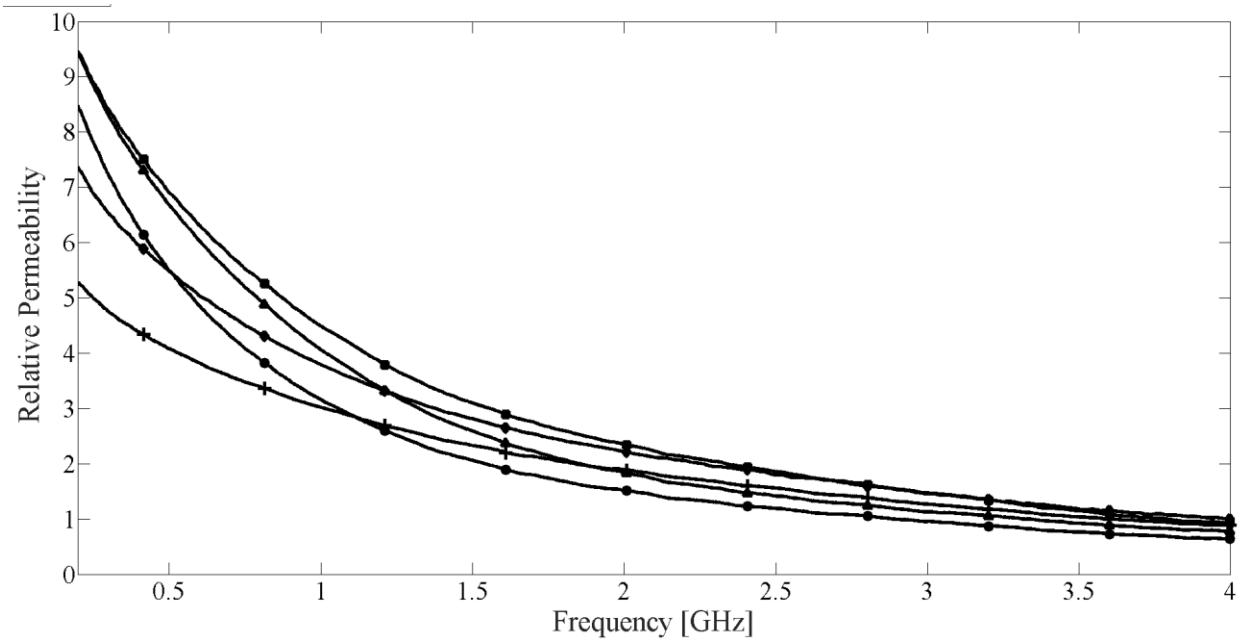

Figure 20: Relative permeability as a function of frequency for each of the five ferrite composites.

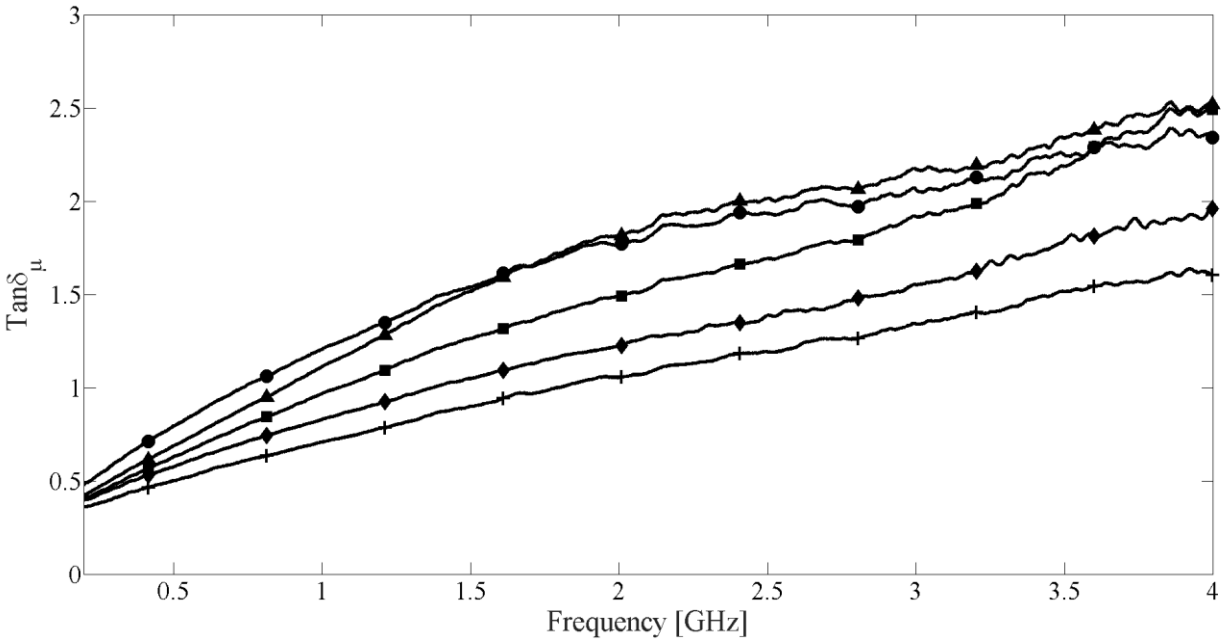

Figure 21: Magnetic loss tangent as a function of frequency for each of the five ferrite composites.

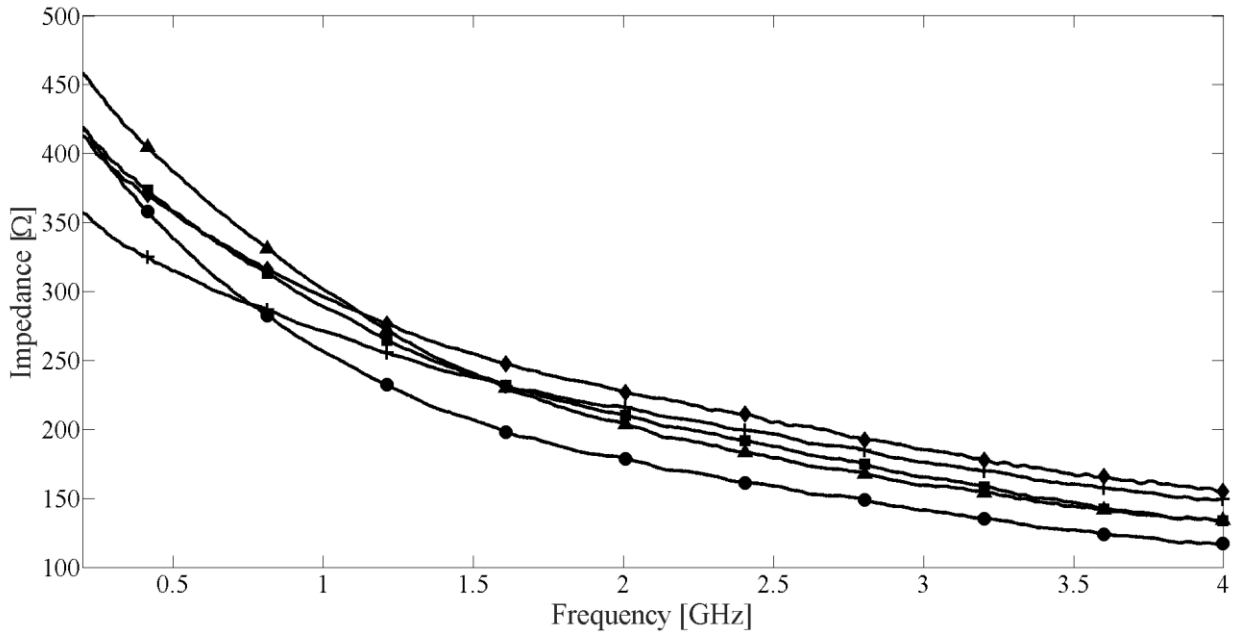

Figure 22: Impedance as a function of frequency for each of the five ferrite composites.

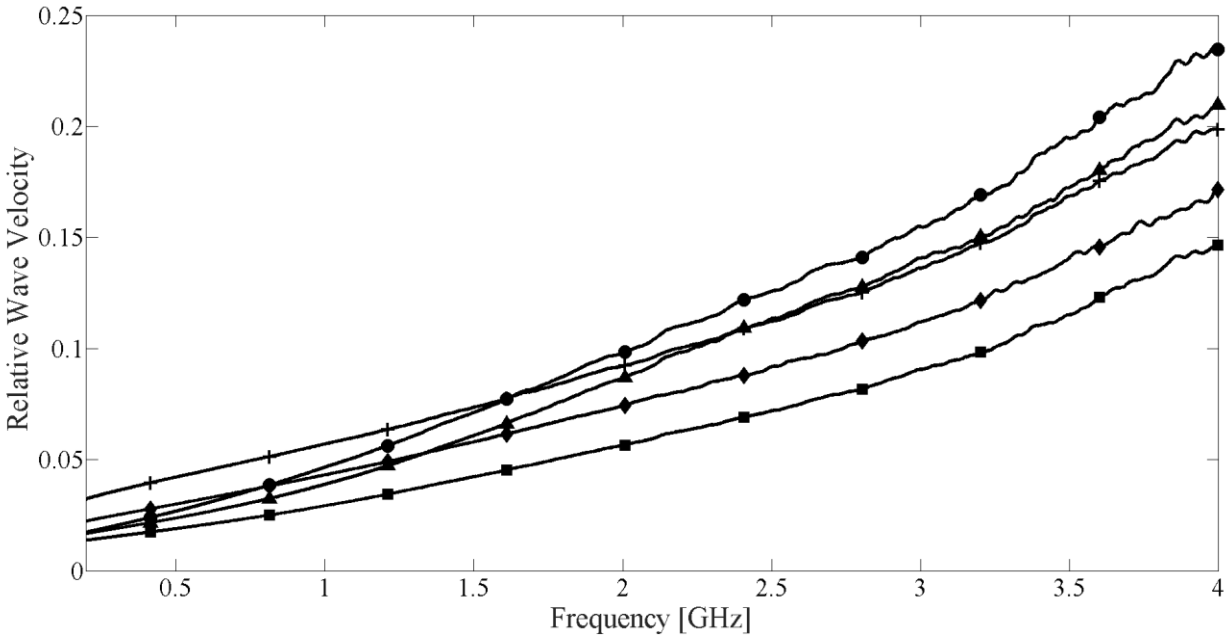

Figure 23: Relative wave velocity as a function of frequency for each of the five ferrite composites.

5.3.3 Bimodal Distribution

For the bimodal distribution, MMU1 and MMU3 were selected for study due to their high performance in the breakdown tests. Also, both of these ferrite powders showed strong electromagnetic properties for the continuous distribution. Figure 24 and Figure 25 show the MMU1 values obtained for the complex relative permittivity and permeability, respectively.

Figure 24 and Figure 25 show that using a bimodal distribution results in the permittivity of the material increasing over most of the frequency range tested. We believe that this result is due to an increased order of the distribution, which leads to increased polarization due to a more even dispersal of the electric field energy. It is also interesting to note that the permittivity value increases above 2 GHz. This effect is most likely due to a resonance within the material but test equipment limitations make a solid conclusion difficult. In any case, the effect is beyond the usable range of the material, causing little impact on the analysis. The decrease in the magnetic permeability is expected since the bimodal distribution is less dense than the continuous distribution, reducing the ferromagnetic material content. Figure 26 and Figure 27 show, respectively, the impedance and relative wave velocity values obtained for MMU1. Figure 26 shows that the impedance of the wave is within 50% of the free space value up to 2.5 GHz. Figure 27 shows that at 2 GHz a size reduction of 4.8 can be expected.

As with the MMU1 case, Figure 28 and Figure 29 show the MMU3 values obtained for the complex permittivity and permeability respectively. Again we see a slight increase in the permittivity value and a decrease in permeability value. Figure 30 shows an impedance within 50% of free space up to about 700 MHz. At 2 GHz, Figure 31 shows a size reduction of 4.

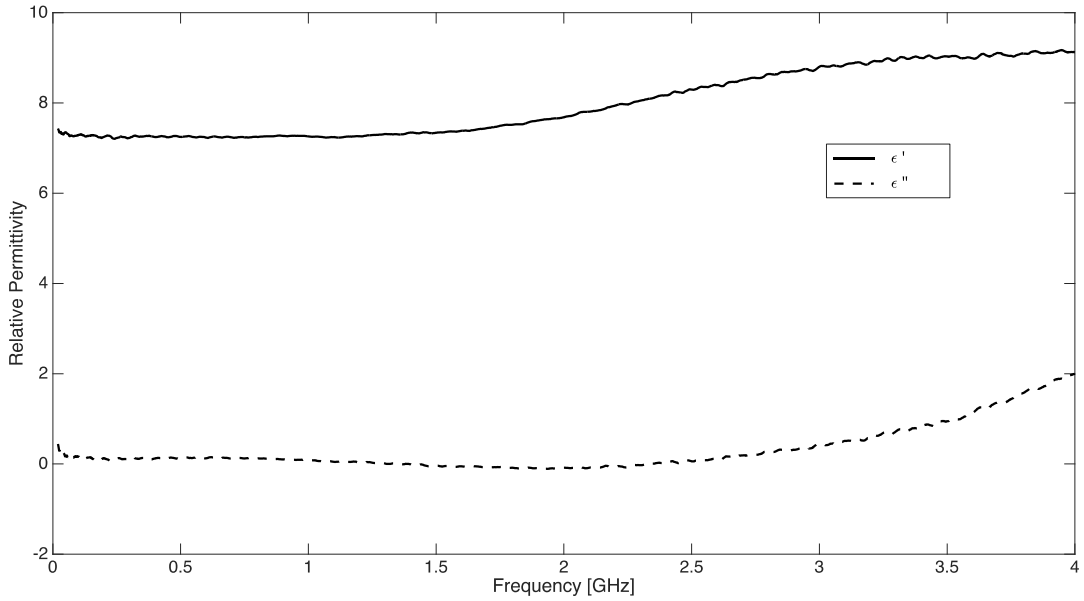

Figure 24: Complex relative permittivity as a function of frequency for bimodal MMU1.

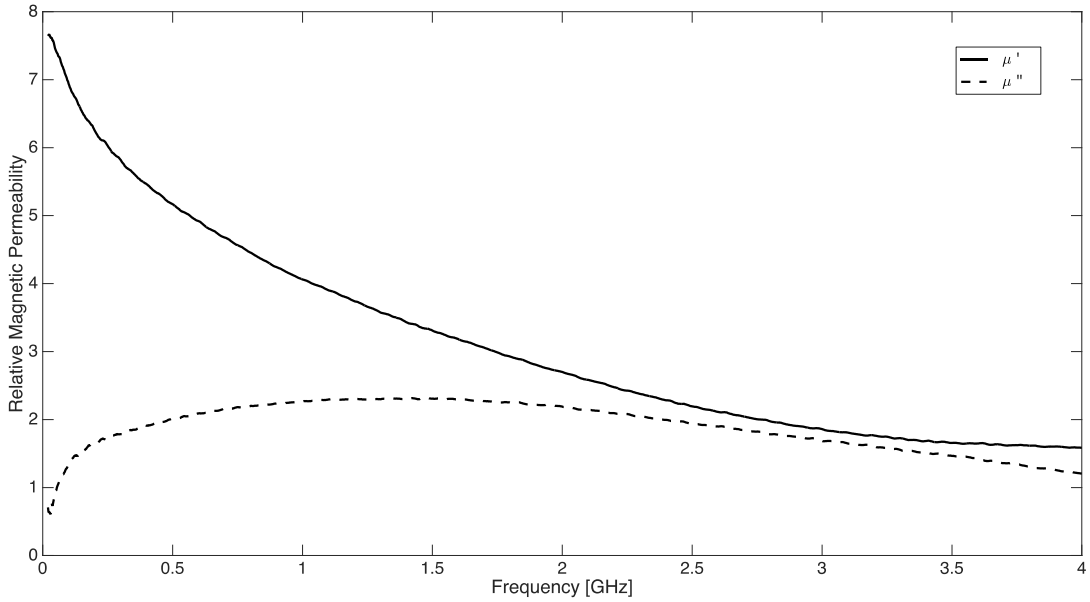

Figure 25: Complex relative magnetic permeability as a function of frequency for bimodal MMU1

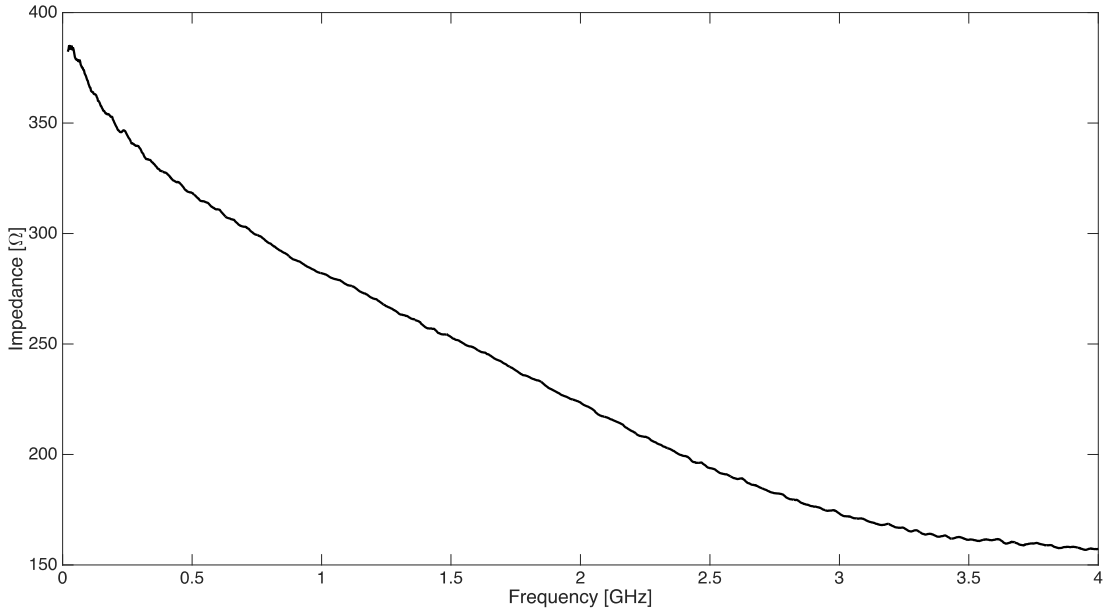

Figure 26: Impedance as a function of frequency for bimodal MMU1

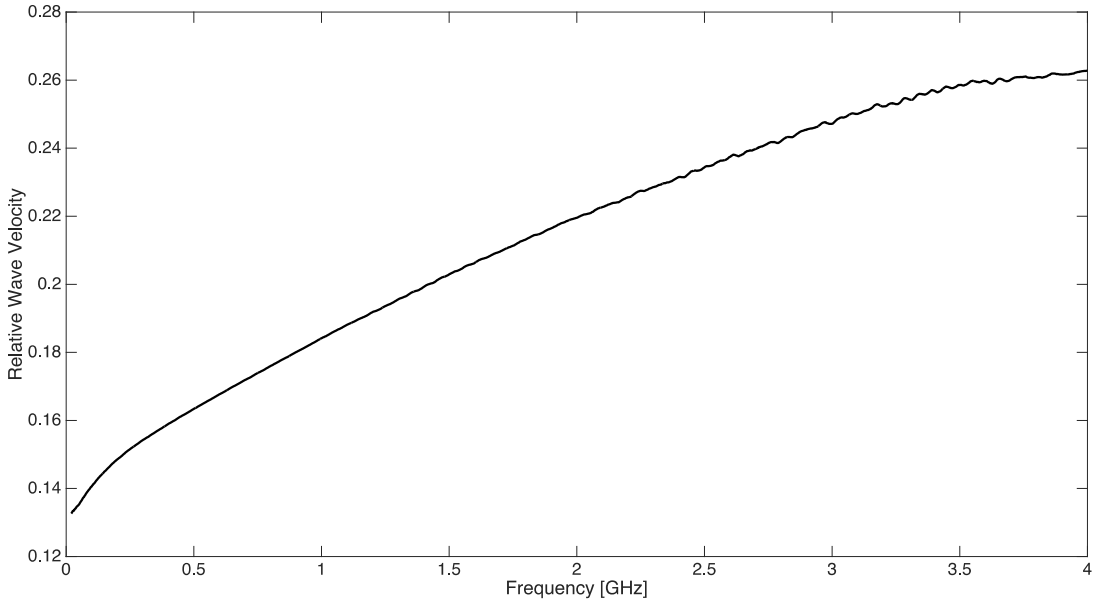

Figure 27: Relative wave velocity as a function of frequency for bimodal MMU1

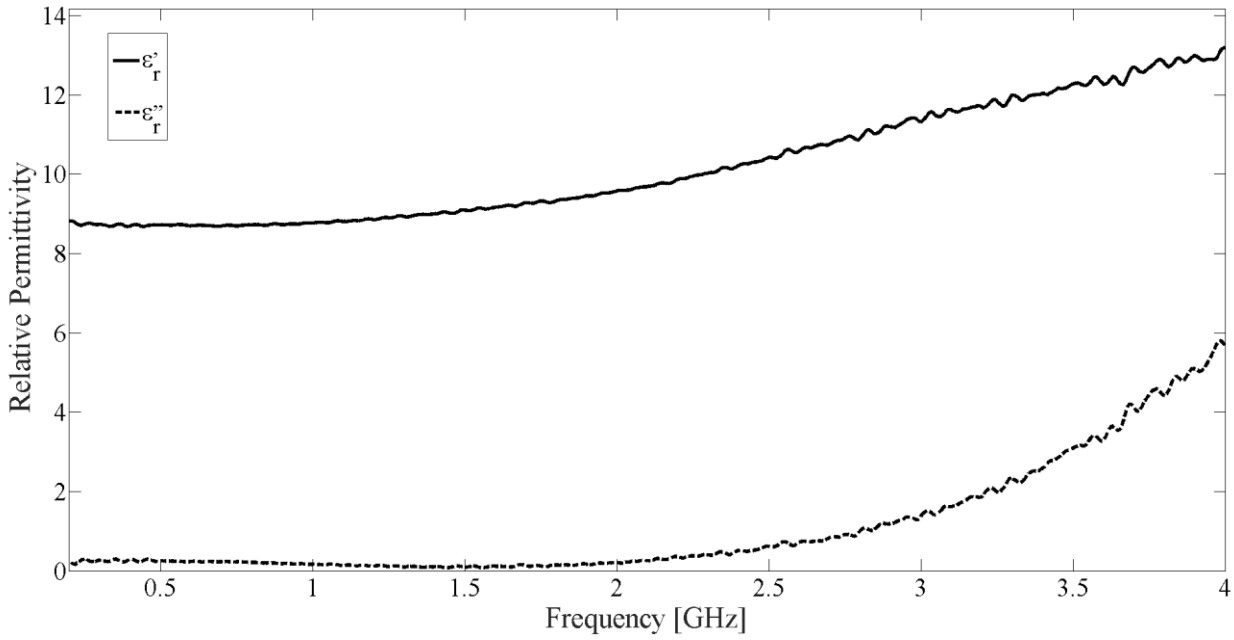

Figure 28: Complex relative permittivity as a function of frequency for bimodal MMU3

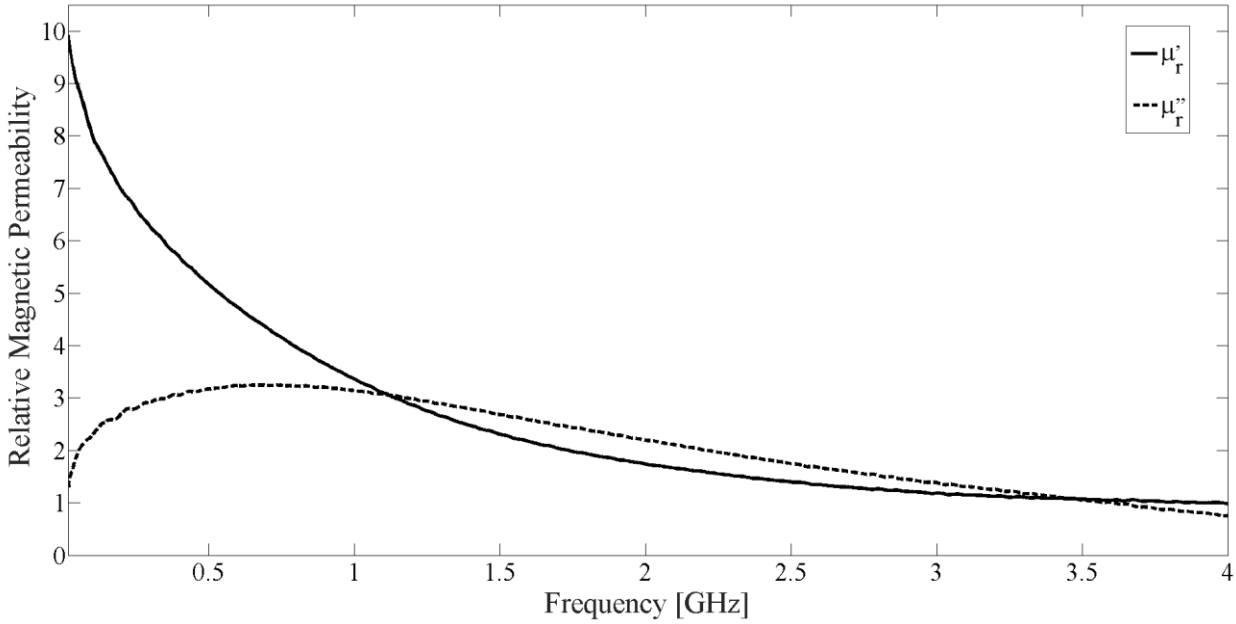

Figure 29: Complex relative magnetic permeability as a function of frequency for bimodal MMU3

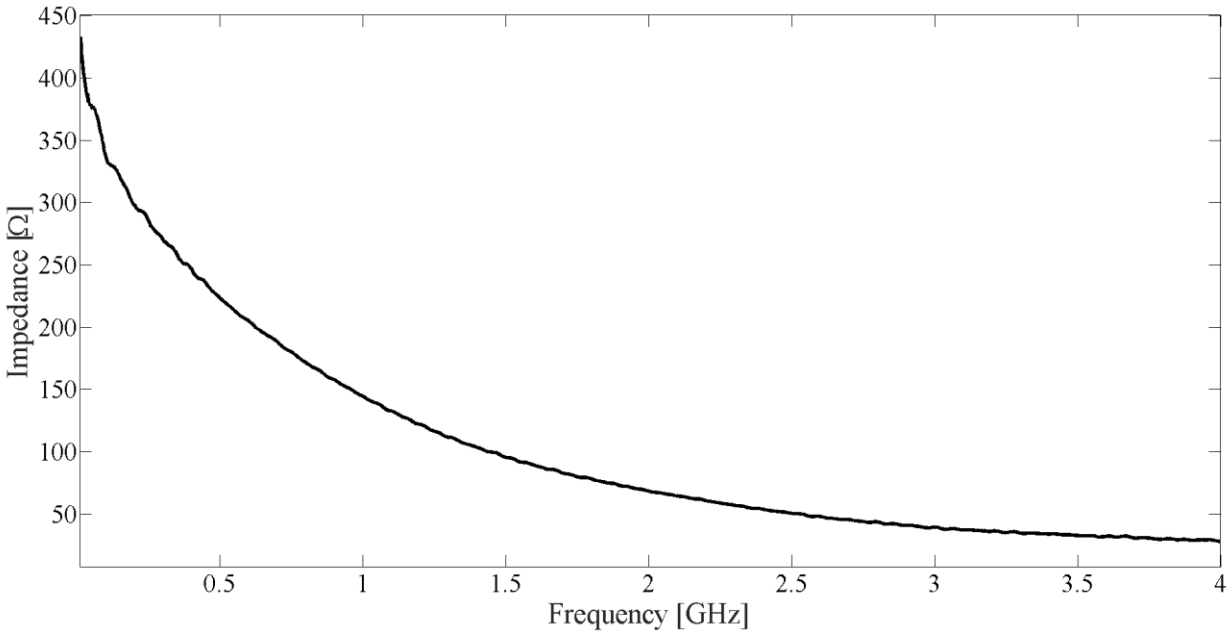

Figure 30: Impedance as a function of frequency for bimodal MMU3

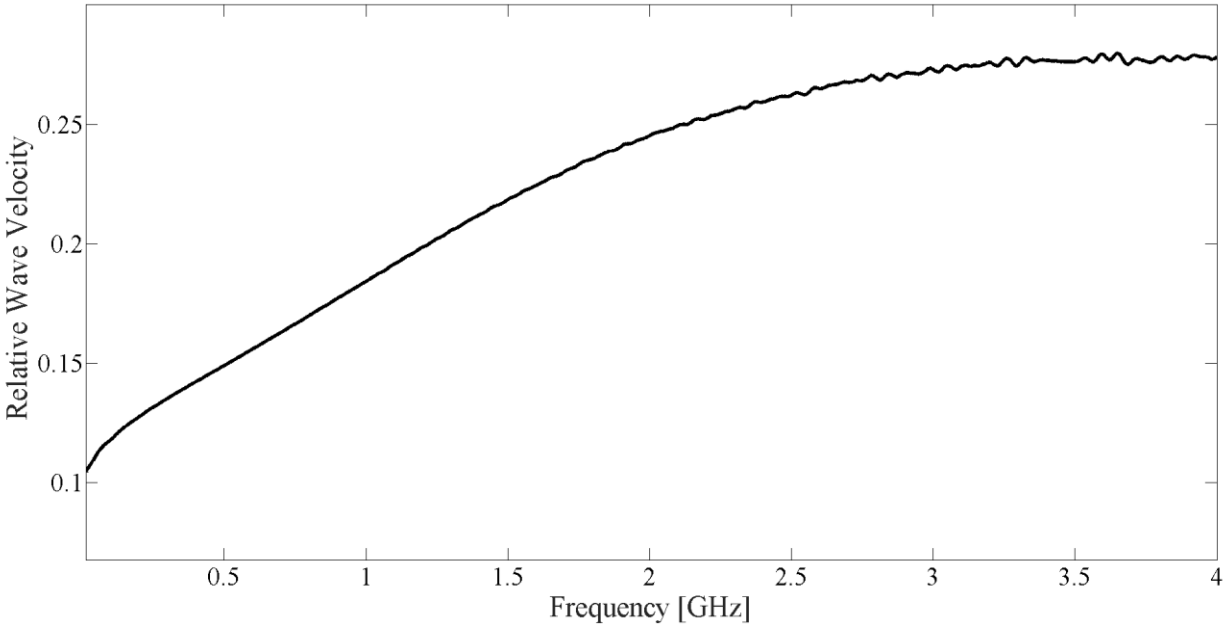

Figure 31: Relative wave velocity as a function of frequency for bimodal MMU3

5.3.4 Trimodal Distribution

For the trimodal distribution tests, MMU1 was selected due to its high breakdown strength and superior electromagnetic properties in the bimodal distribution as compared to MMU3. Figures 32-35 show the MMU3 values of the complex permittivity, complex magnetic permeability, impedance, and relative wave velocity, respectively. The frequency range is restricted to 2 GHz in order to highlight the region that this material has shown the most interesting electromagnetic properties. We see that the permittivity value increased substantially over the bimodal case. On average the permittivity value increased by about 4. The permeability also increased by about 0.5 while the magnetic losses increased about 2. Both of these increases can be explained by the increased density of the magnetic material in the trimodal distribution as compared to the bimodal. Figure 34 shows the material being within 50% of the free space impedance up until 1.5 GHz, and at 2 GHz Figure 35 shows a size reduction of 5.1 if a traveling wave antenna is built using MMU1 material.

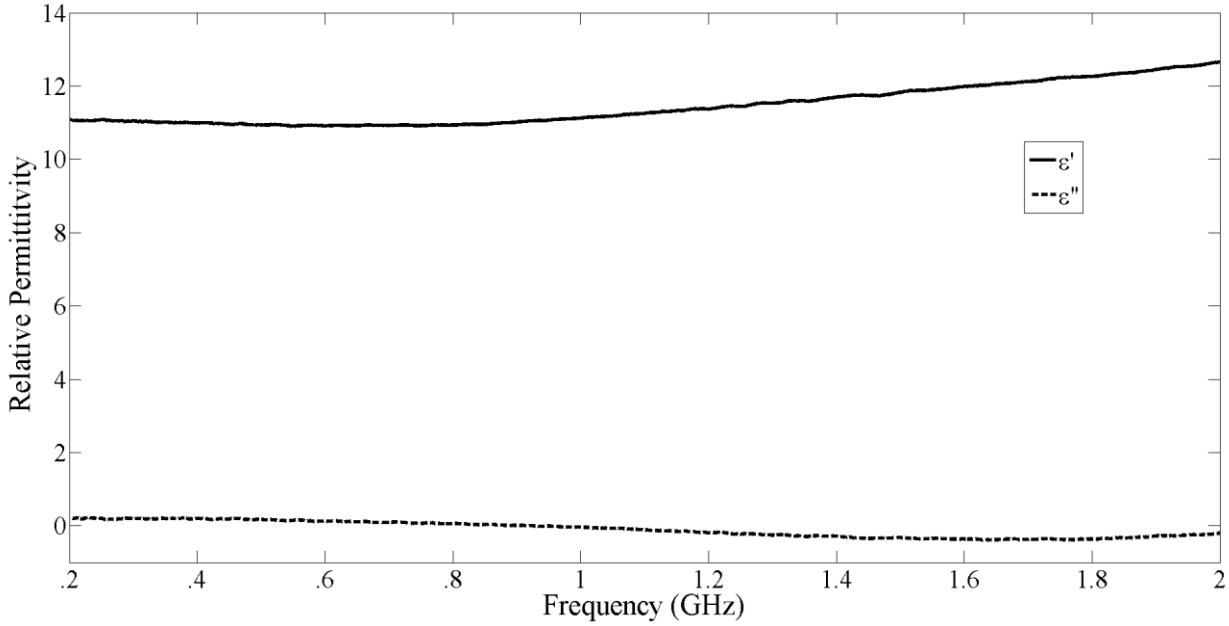

Figure 32: Relative permittivity as a function of frequency for trimodal MMU1

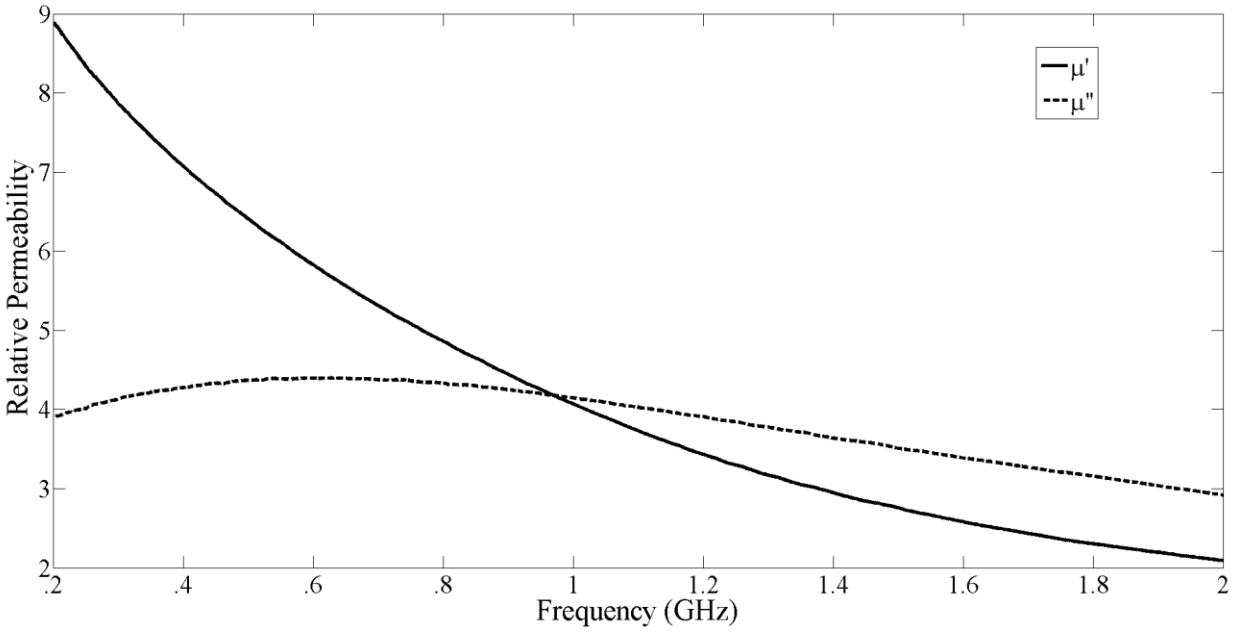

Figure 33: Relative magnetic permeability as a function of frequency for trimodal MMU1

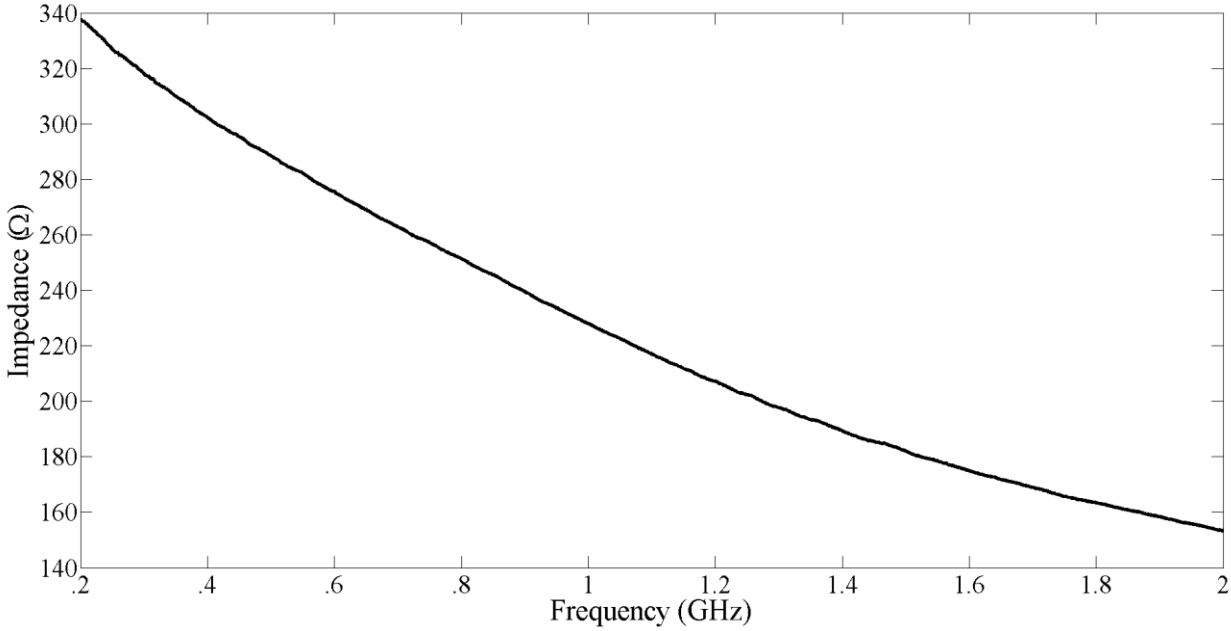

Figure 34: Impedance as a function of frequency for trimodal MMU1

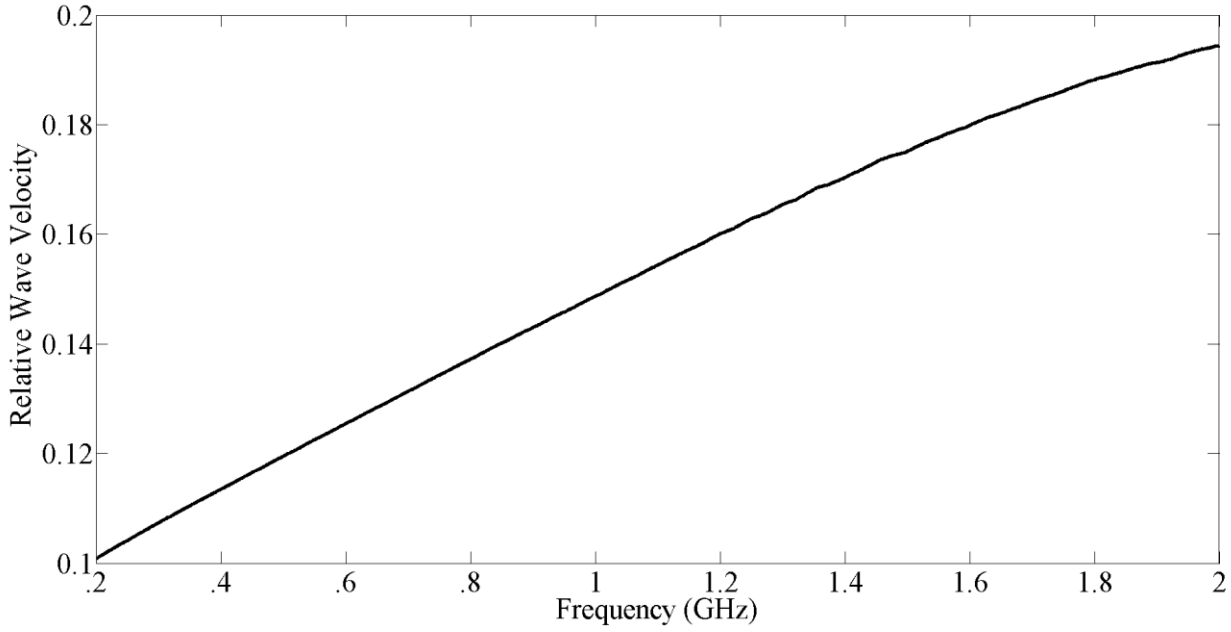

Figure 35: Relative wave velocity as a function of frequency for trimodal MMU1

5.3.5 Barium Titanate Ferrite Composites

The relative permittivity and permeability of the BTF composites were measured and then compared to ferrite composites. The dielectric constants are seen in Figure 36 and the process increases the dielectric constant of the ferrite metamaterials by about 9%. The permeability of the BTF composite, seen in Figure 37, is lower than the ferrite but does not drop as quickly at higher frequencies. This effect is a result of the amount of magnetic material in the BTF particles which can be 50% less. The barium titanate shell also forms an air gap between the particles reducing the permeability.

The barium titanate that is synthesized around the ferrite particles was calculated to form a 1:1 molar ratio of ferrite to $BaTiO_3$. The BTF composites have distinctly less ferrite material than the ferrite only composites, which is the reason for the decreased permeability.

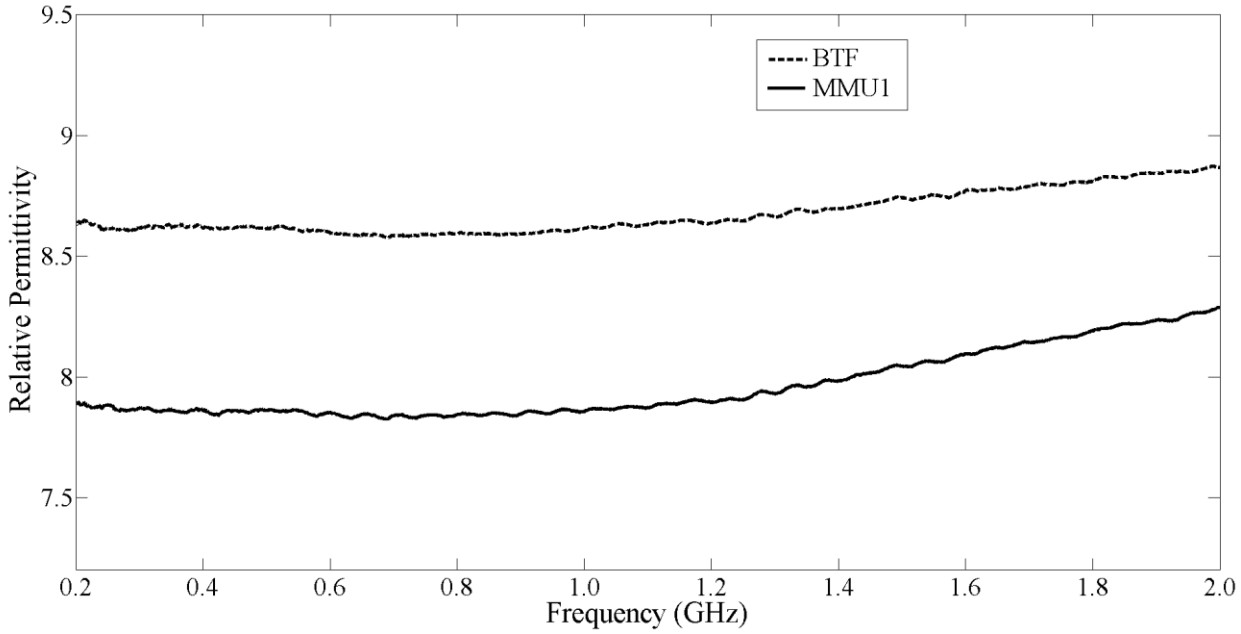

Figure 36: Effective Permittivity of BTF Single Mode Composite

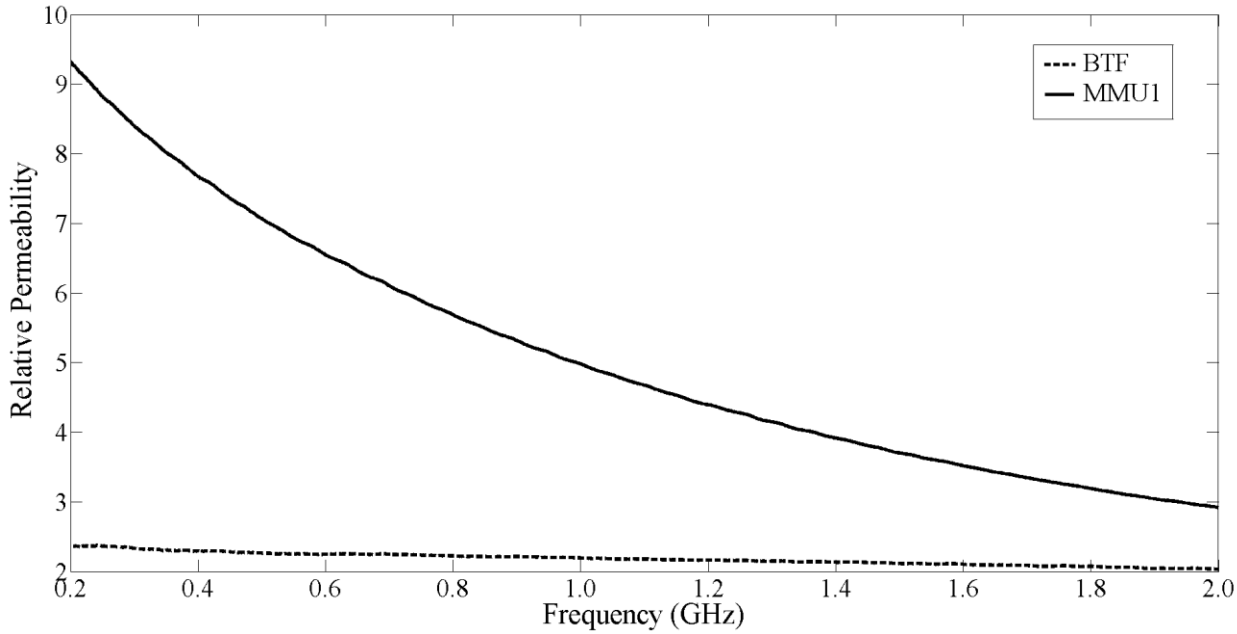

Figure 37: Effective Permeability of BFT Single Mode Composite

The losses of the barium titanate-ferrite composites are also compared to ferrite composites. Figure 38 and Figure 39 show the dielectric and magnetic losses of both materials. The dielectric losses of the BTF composites are higher than the ferrites, but both materials still have rather low dielectric loss. The magnetic loss of the BTF material is much less than ferrite composites. By separating the individual magnetic domains with dielectric material, the interaction between the ferrite particles lessens, thus decreasing the loss. If the particle size of the magnetic core contains a partial magnetic domain, the magnetic field will extend into the $BaTiO_3$ [29] [30].

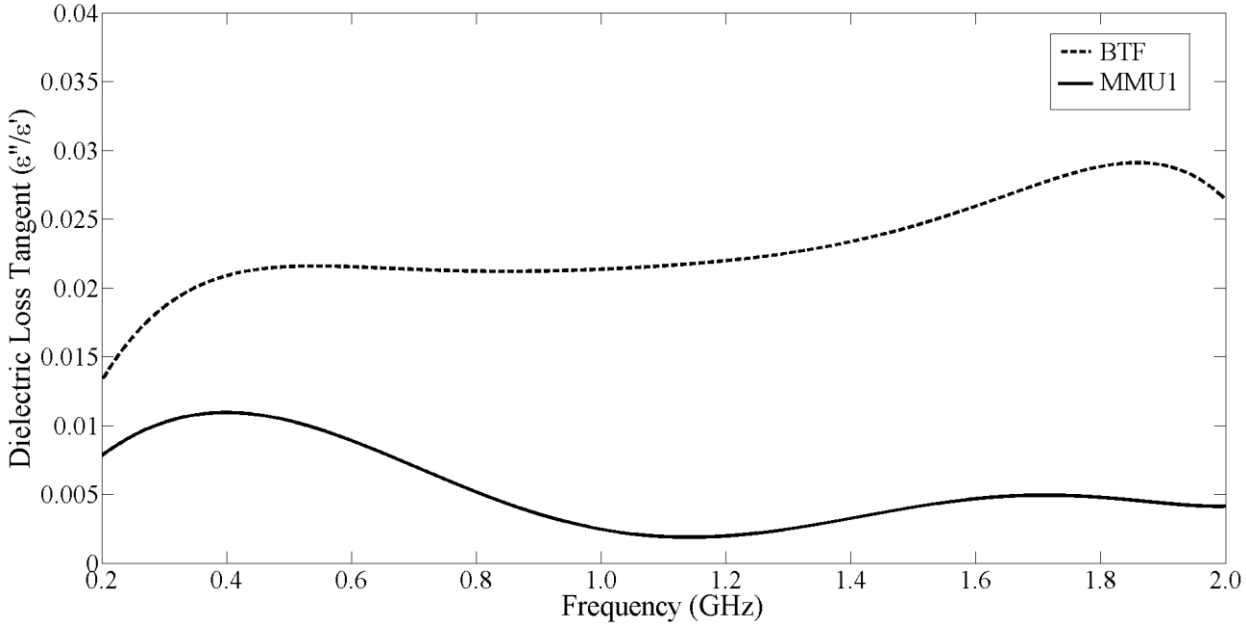

Figure 38: Dielectric Loss of BTF Single Mode Composite

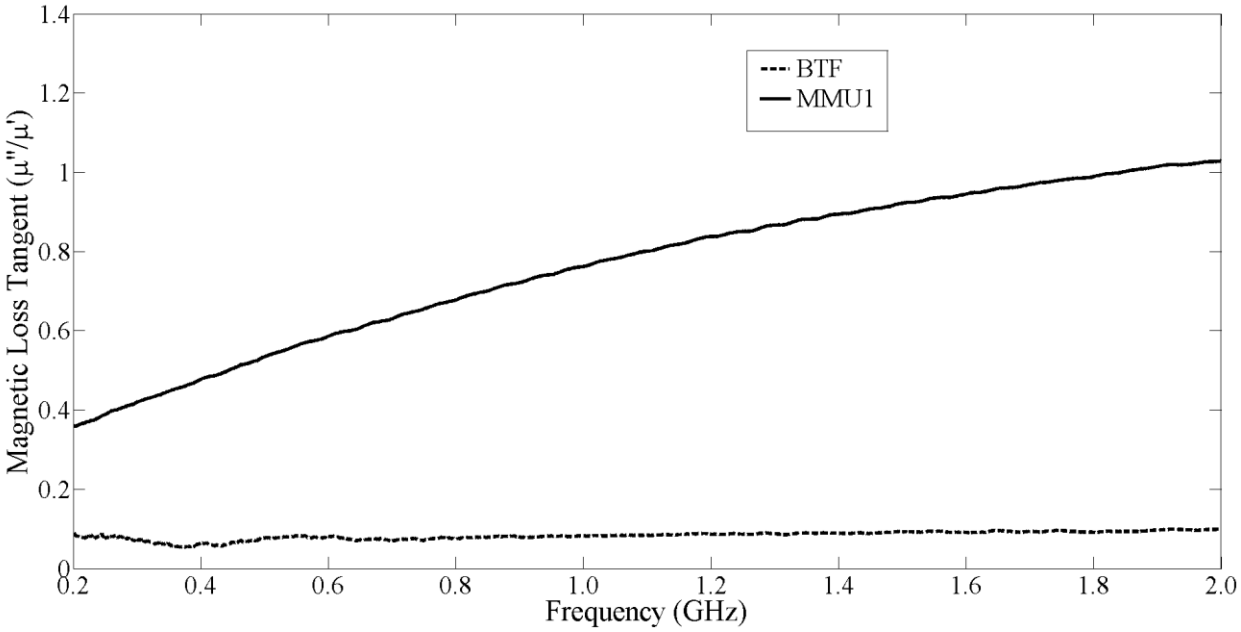

Figure 39: Magnetic Loss of BTF Single Mode Composite

The impedance and relative wave velocities can be calculated from the permittivity and permeability of the composites using Equations 5.3.1.1 and 5.3.1.2. Figure 40 shows the

impedance of the BTF composite and the ferrite composites while Figure 41 shows the relative wave velocities. The ferrite composites match free space impedance around 400 MHz but decreases significantly due to the decrease in permeability as the frequency increases. The BTF composites have a constant impedance around 200-180 Ω. The relative wave velocities have an inverted trend compared to their impedances, so the ferrite composites increase from 12% to 20% of the speed of light while the BTF composites stay around 22%.

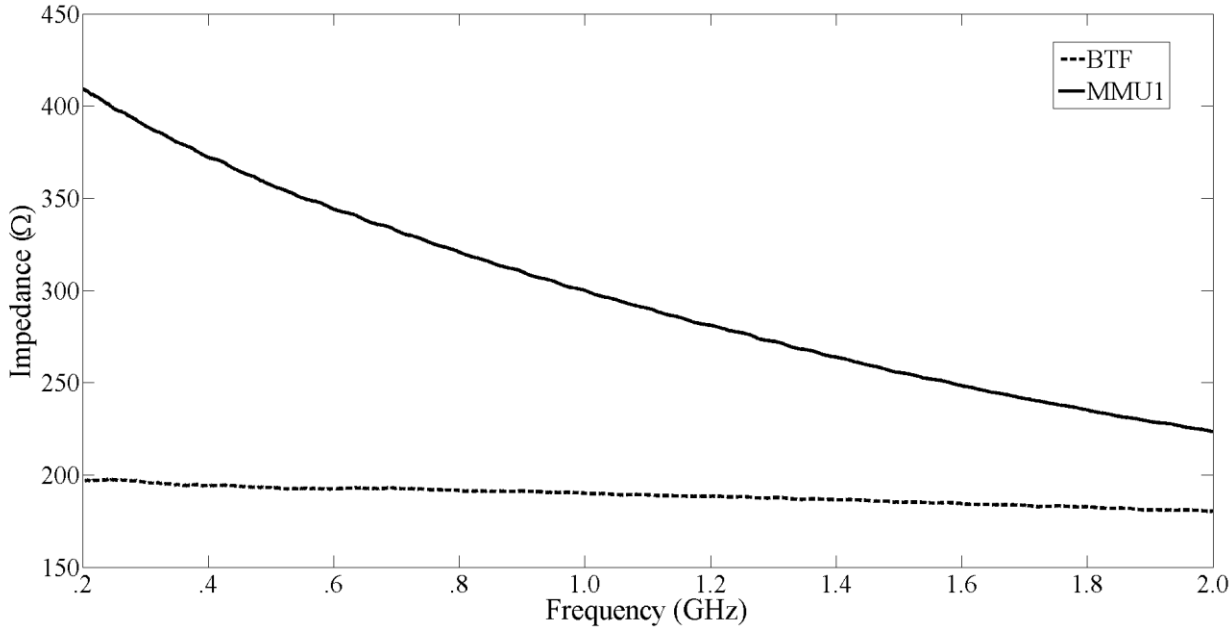

Figure 40: Impedance of BTF Composites

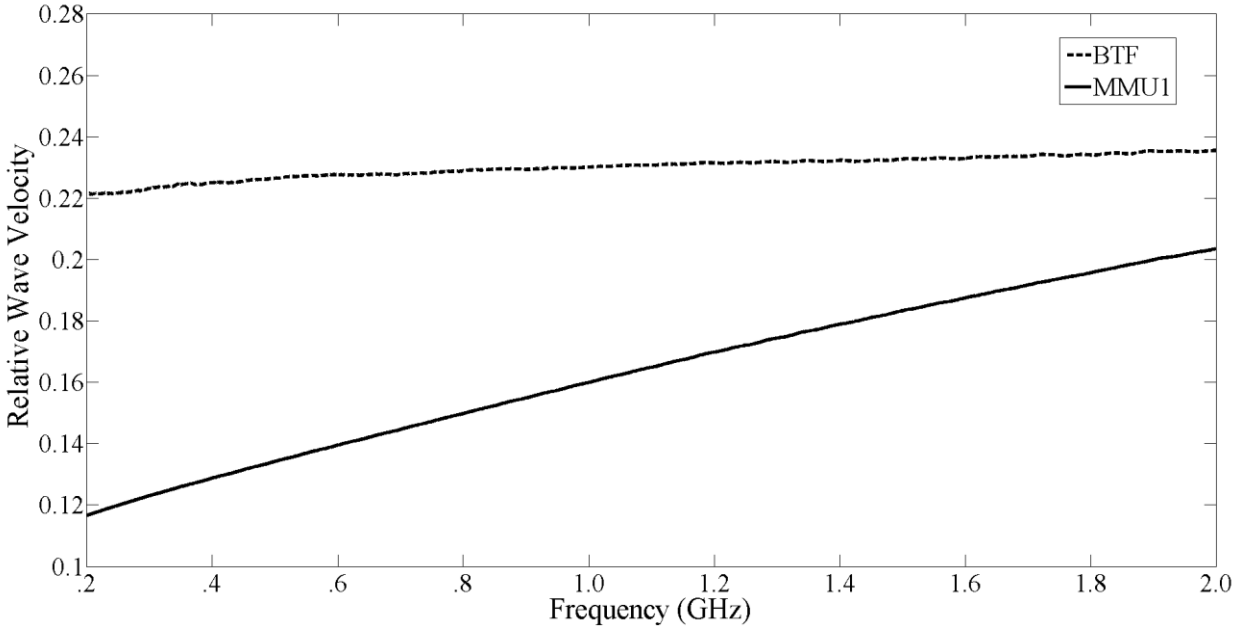

Figure 41: Relative Wave Velocity of BTF Composites

The bimodal and trimodal mixes discussed earlier were also analyzed with the airline and compared with bimodal and trimodal mixes of ferrite composites. The core shell material with a trimodal mix shows a resonance around 3.2 GHz, as seen in Figure 46. This occurs from using sample length that is a quarter wavelength at the resonant frequency. Figure 42 and Figure 43 show bimodal permittivity and permeability with shorter samples without the resonance. The bimodal ferrite composites have a permittivity and permeability that are very similar to each other, resulting in better impedance matching. The addition of barium titanate again increases the permittivity of the BTF composites, and the transition to bimodal and trimodal distributions lowers the dielectric loss as seen in Figure 44 and Figure 45: Bimodal BTF Magnetic Loss. The drawback of the ferrite composites is that the magnetic losses, seen in Figure 45, are much higher than the magnetic loss of the BTF composites.

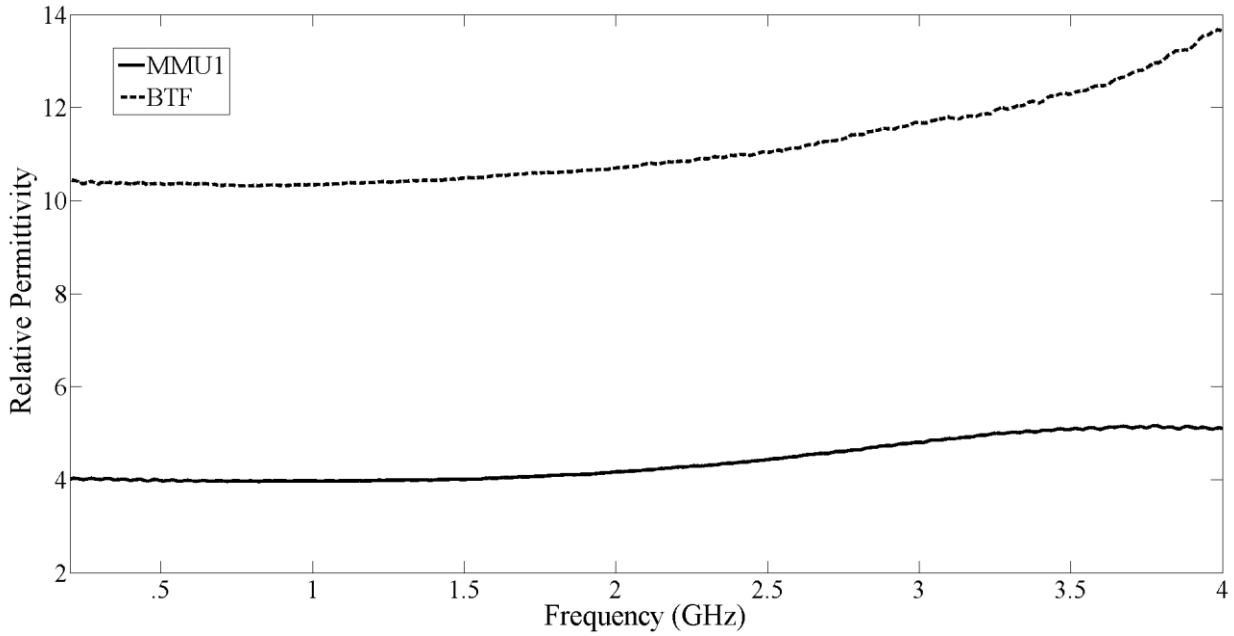

Figure 42: Bimodal BTF Relative Permittivity

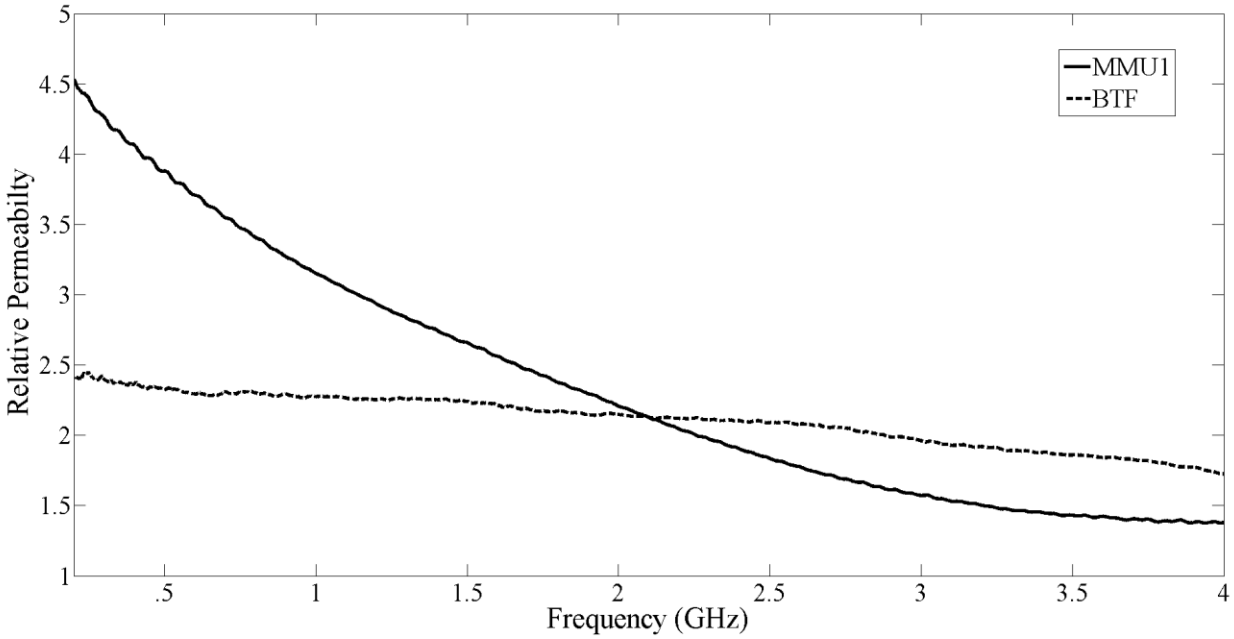

Figure 43: Bimodal BTF Relative Permeability

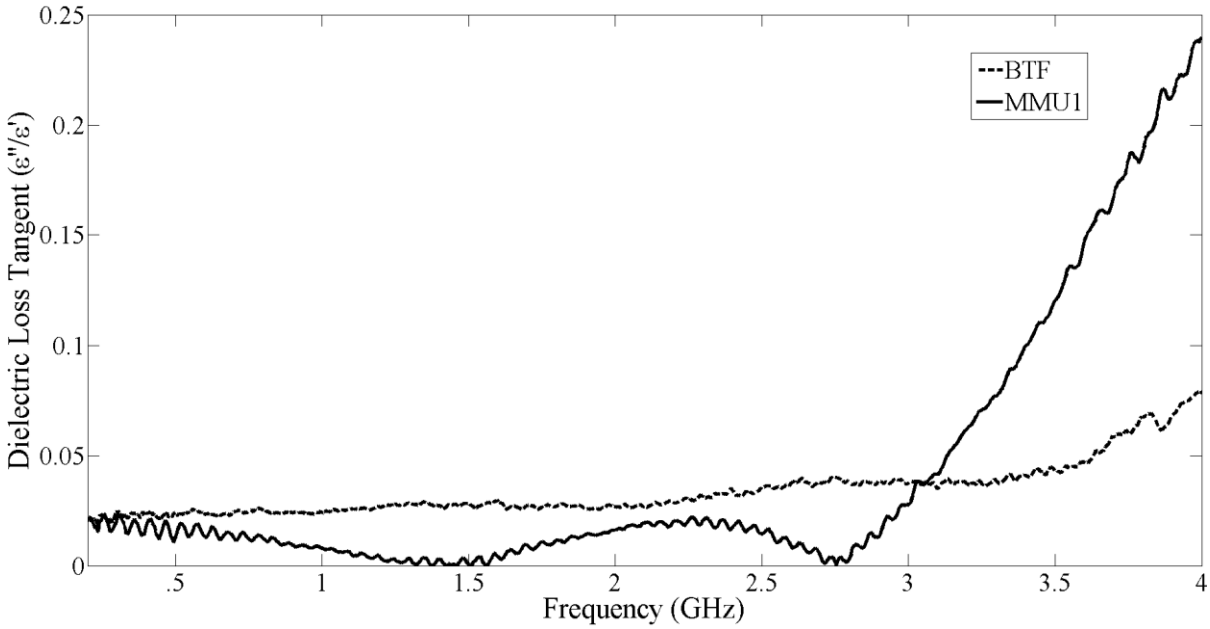

Figure 44: Bimodal BTF Dielectric Loss

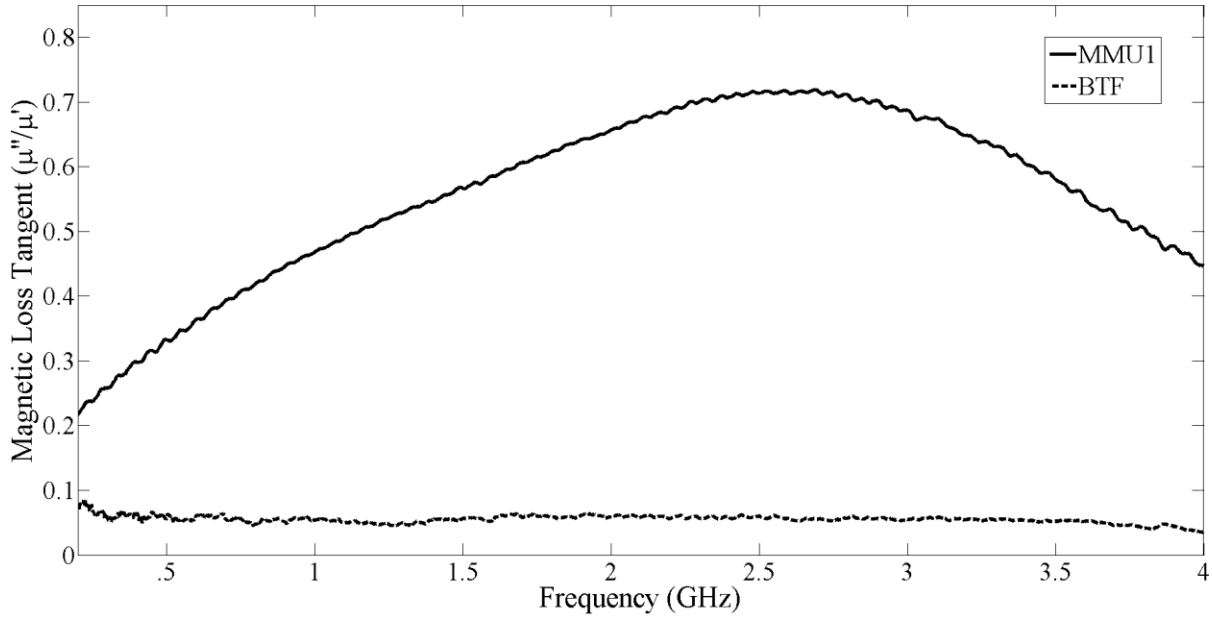

Figure 45: Bimodal BTF Magnetic Loss

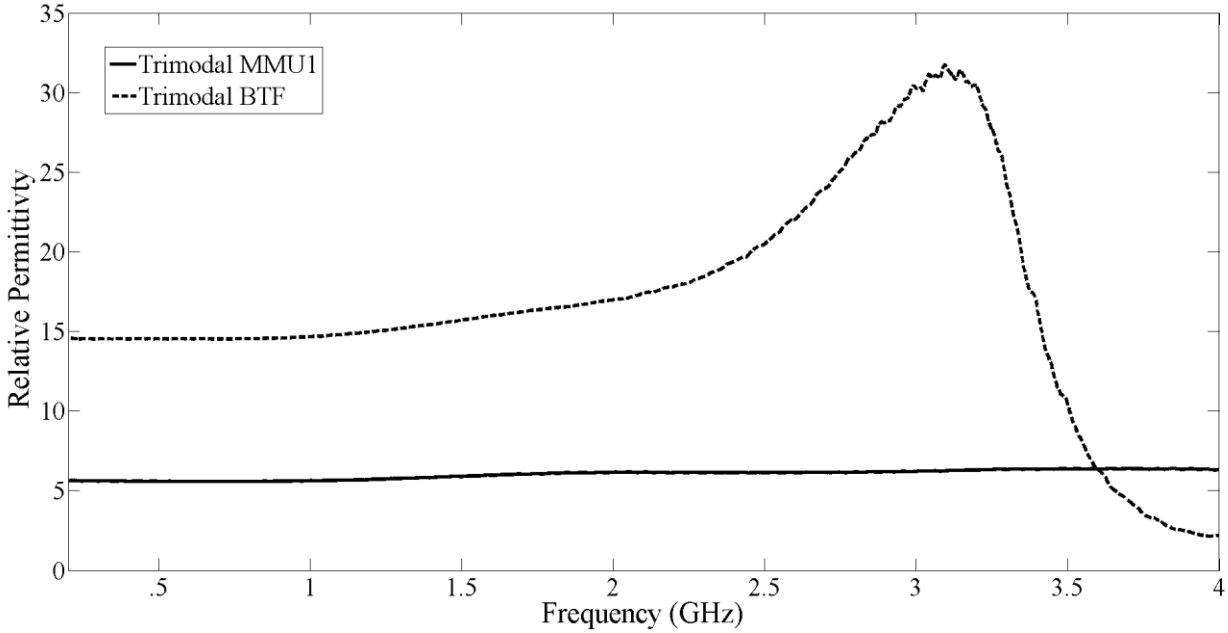

Figure 46: Trimodal BTF Relative Permittivity

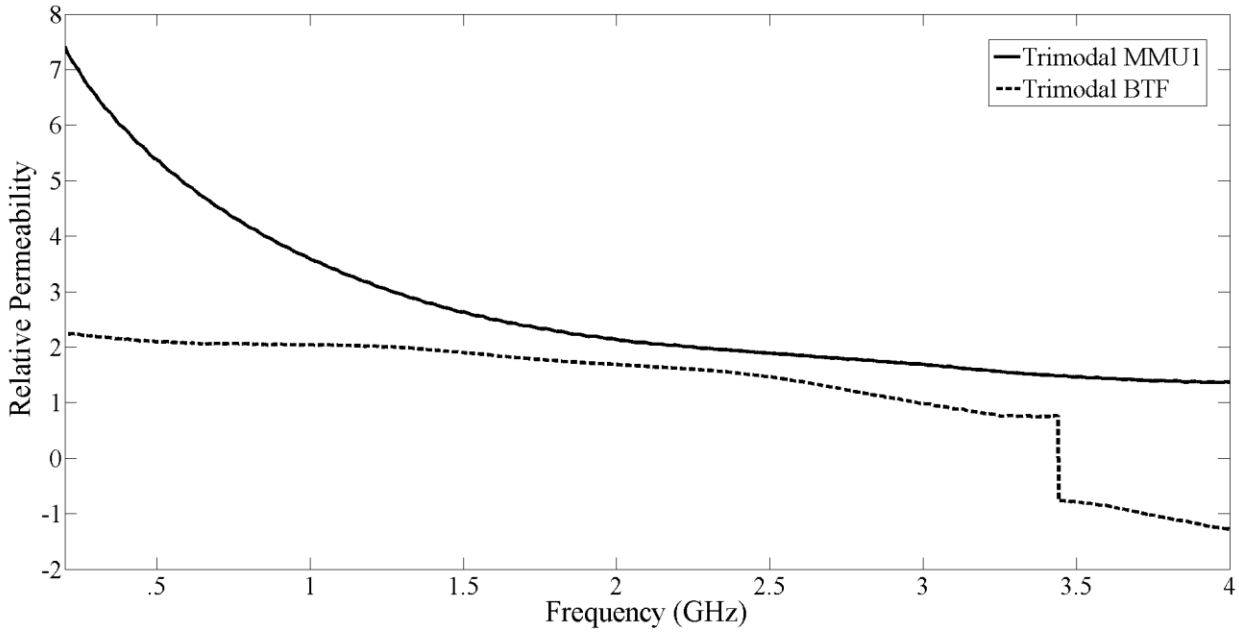

Figure 47: Trimodal BTF Relative Permeability

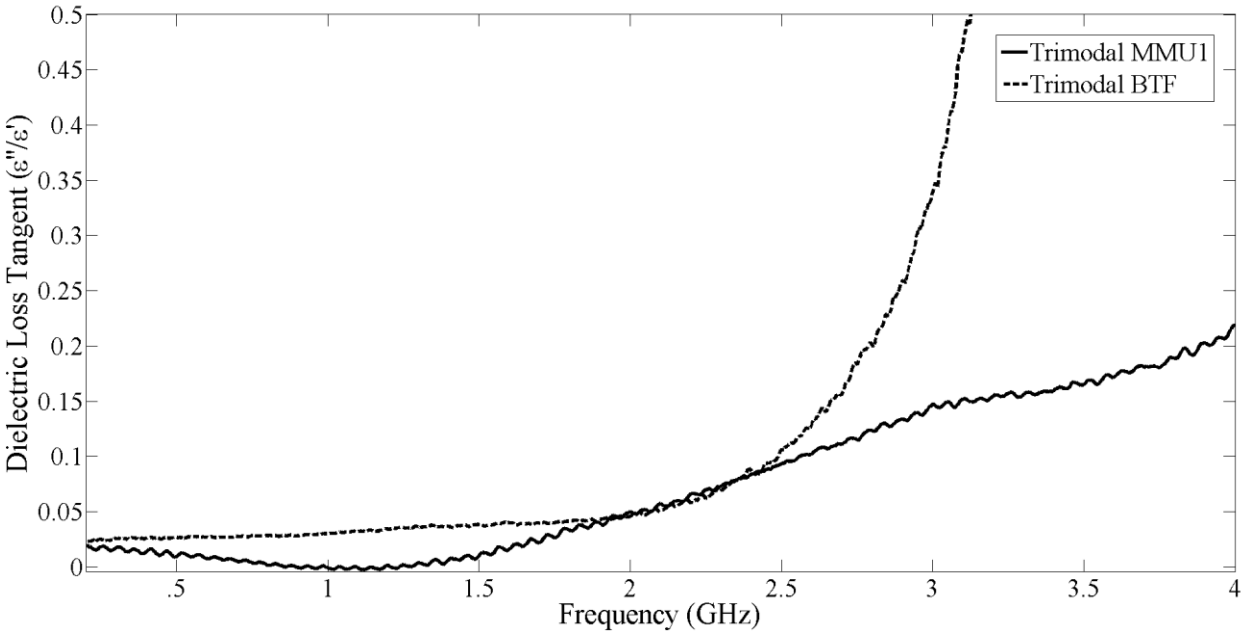

Figure 48: Trimodal BTF Dielectric Loss

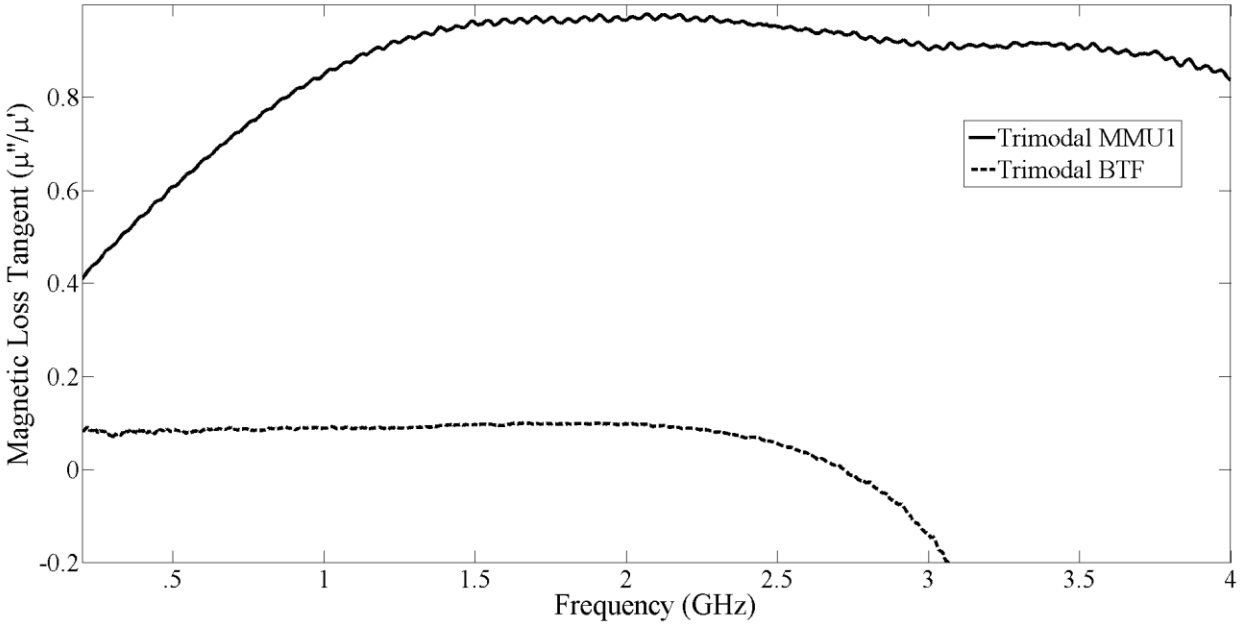

Figure 49: Trimodal BTF Magnetic Loss

6. Dielectric Strength Measurement

6.1 Design of Pulsed Dielectric Breakdown Test Stand

An important factor in determining the survivability of a material for use in a high power antenna system is its dielectric strength. The ability of a material to withstand extremely high electric fields is often a limiting factor in the power handling capability of this type of antenna. Also, since the desired application is to hasten the development of compact systems in which the energy density is high as compared to the system volume, measurement and characterization of the material's ability to withstand such fields is of the upmost interest.

There are a number of different methods for evaluating the dielectric strength of a material. Many involve the application of a DC voltage or with a pulsed slow rise-time voltage to be placed across the sample. In these types of tests the voltage is increased until destructive breakdown is observed. The attractiveness in such tests is that the test apparatus is relatively simple to design and build, as well as the results being easy to interpret. However, it was determined that such an experiment would be less than insightful. This is due to the fast rise time of the applied voltage seen in high power antennas. For this reason, it was decided that the composite material needed to be tested under pulsed conditions, allowing for the characterization of the material in an environment closest its desired application.

Such a test is also useful for establishing peak electric field values in pulsed ring-down antennas and other transient RF applications due to the high $\frac{dV}{dt}$ values that can be present. The down side to testing under pulsed conditions is two-fold. First, the practical rise time of the applied voltage pulse is limited by the speed of diagnostic equipment. The rise time must be slow enough that the diagnostics can accurately measure the peak voltage across the sample. Second, stray inductances become a serious concern in any pulsed power system and controlling these inductances complicates the design process.

A PA-80 pulse generator from L-3 Communications Pulse Sciences was used as the high voltage source for the dielectric strength test stand [31]. Figure 50 shows a schematic of the circuit.

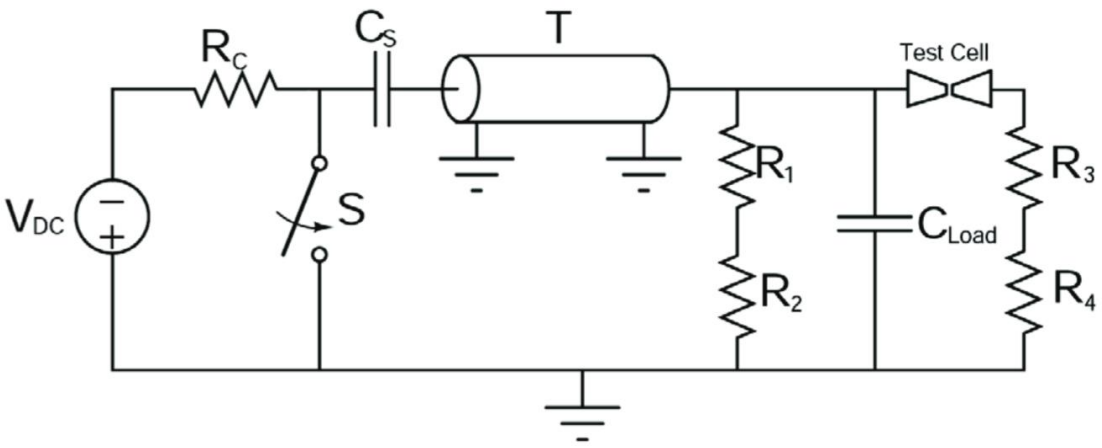

Figure 50: Circuit diagram for PA-80 pulse system

A 75 nF capacitance C_s was resistively charged. Once charging is complete, switch S is closed. This results in C_s discharging into a 50Ω, RG-218/U coaxial transmission line. The transmission line is terminated into a high impedance load consisting of parallel arrangement of the dielectric test cell, a capacitance C_{load} of 0.54 nF and a high resistance, $R_1 + R_2$. Since C_{load} is much smaller and the resistance is very high, the voltage across the test cell was able to reach a max peak of around 100kV [32]. The 10% to 90% rise time of the system has been measured to be approximately 60 ns. Figure 51 shows a photograph of the pulse generator, left, and the test cell, right. The test cell consists of an acrylic housing in which Shell Diala dielectric oil was used as the high voltage insulator.

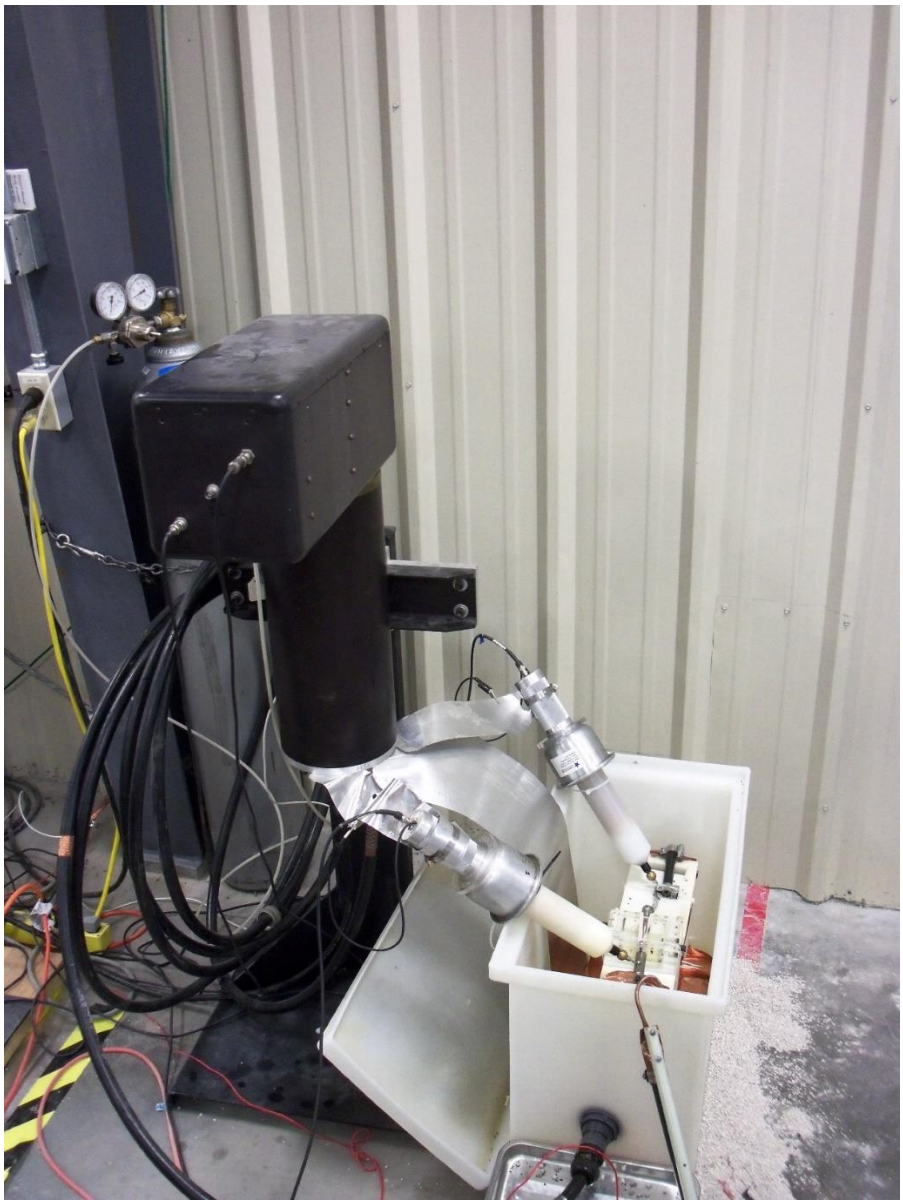

Figure 51: Pulse generation system (left) and test cell (right) used for dielectric breakdown experiments

The voltage diagnostics consisted of two North Star high voltage probes with a 1000:1 ratio. One probe measures each side of the test cell with a Tektronix DPO7254 Digital Phosphor Oscilloscope [33]. To protect the sensitive electronics in the scope, a Faraday cage was built to isolate the scope from the electric fields generated by the high voltage supply and PA-80 pulser.

Figure 52 shows a close up of the test cell and the high voltage probes. Tests utilized samples of disks 2.54 cm diameter and 0.2 cm thick with four test sites prepared on each disk.

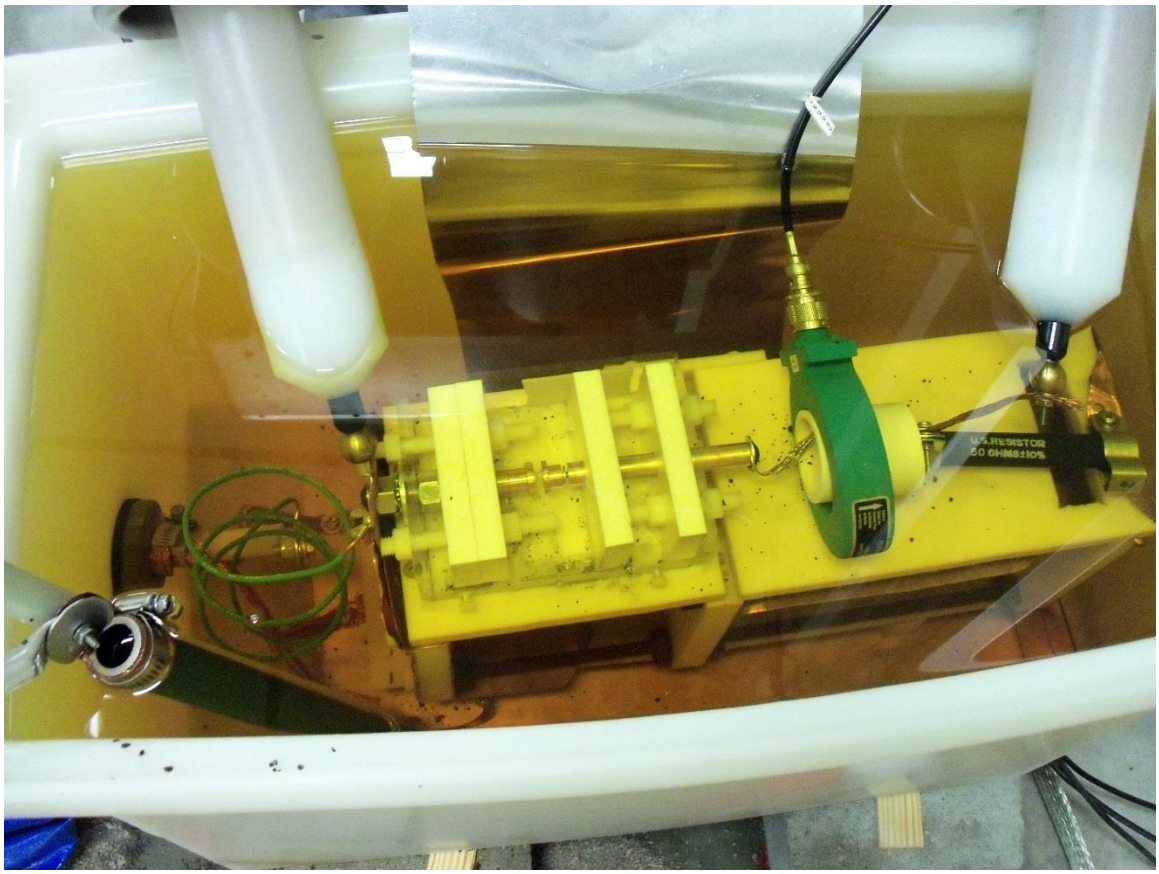

Figure 52: Close up view of the test cell used for dielectric breakdown experiments

6.2 Dielectric Strength Test Material Preparation

Once the disks were pressed and the silane was polymerized, further machining and processing was required before the disk could be evaluated for pulsed breakdown testing. In the tests we accounted for the thickness of each disk, field enhancement factors that were a result of inconsistencies on the disk surface, and the size of the test site electrodes. This led to a post-pressing procedure being developed where each disk was machined via a CNC mill, sanded, and then electrodes were applied to the surface.

After pressing, each disk had a thickness that varied by 0.2 cm on average across the entire surface. Each disk was machined with a CNC mill on each surface, resulting in disks with thickness that varied 0.01 cm on average. This refined degree of variance was considered manageable for our experimental parameter space. The use of the CNC mill also allowed for each

disk to be initially pressed to around 0.3 cm and then machined down to a consistent 0.2 cm to allow for easily comparing the breakdown results between disks.

Field enhancements due to the uneven surfaces of each disk surface were mitigated by repetitive sanding using progressively finer grit sand paper. Initially, 600 grit paper was used followed by 1200, 2000, and polishing with 12000 grit paper. This reduced defects at the surface of each disk to be on the order of 1μm. Another benefit of sanding the surface of each disk was that it standardized the surface bonding of the electrodes.

The last step in preparing the disks for breakdown tests was the addition of electrodes to the disk's surface. The electrodes were applied with a standard laboratory DC sputter coater and were platinum in composition. The sputtering process embedded the highly conductive platinum atoms into the surface, ensuring efficient energy transfer to the test site. Two electrode geometries were used as part of this experiment, with the geometry being the same on both sides of the disk. Each type is shown in Figure 53. The electrode geometry shown in the left side of the figure was used in order to assess any quality control issues in the material manufacturing process. Once it was determined that each disk produced a consistent result, the electrode geometry on the right was used for dielectric strength breakdown collection. All the graphs and data shown in this paper are taken from disks utilizing the electrode geometry shown on the right of Figure 53.

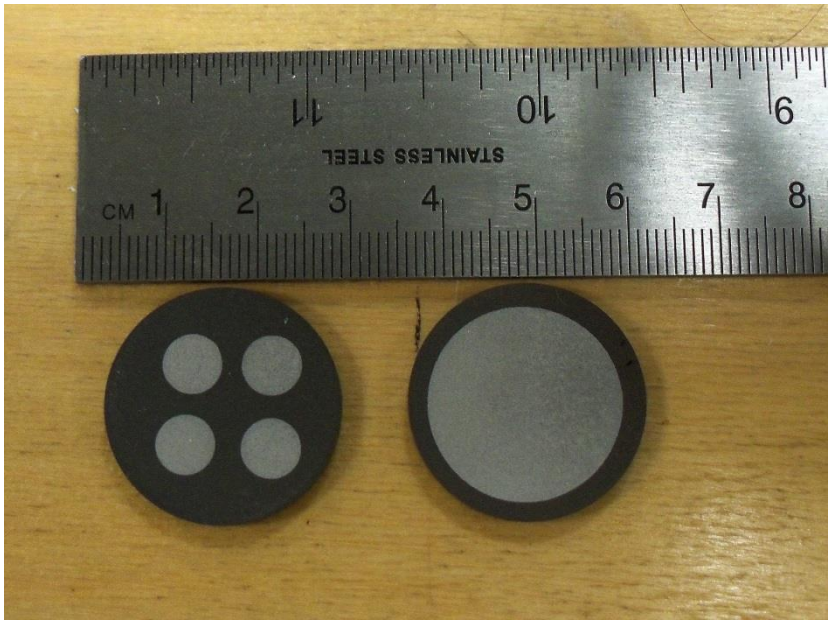

Figure 53: Metamaterial disks with each of the platinum electrode geometries used for dielectric breakdown tests

6.3 Results and Analysis

Figure 54 shows an example of a typical voltage plot that was observed during breakdown. The trace labeled "High Voltage Side" is the signal observed at the output of the PA-80 pulse generator. The other trace is the voltage measured at the low side of the test stand. The dielectric strength of the composites is characterized by analyzing the potential difference between these two signals, which is the voltage drop across the metamaterial composite. Figure 55 shows the plot that is formed when the two signals in Figure 54 are subtracted.

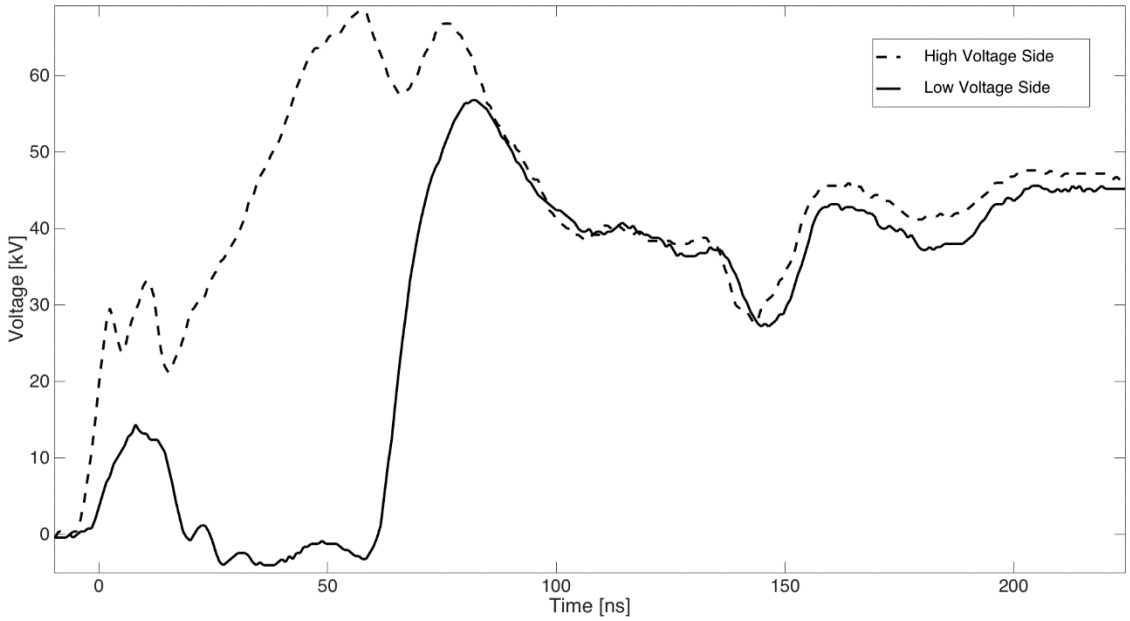

Figure 54: Typical voltage plot observed during pulsed dielectric breakdown of a .2 cm thick ferrite composite test disk.

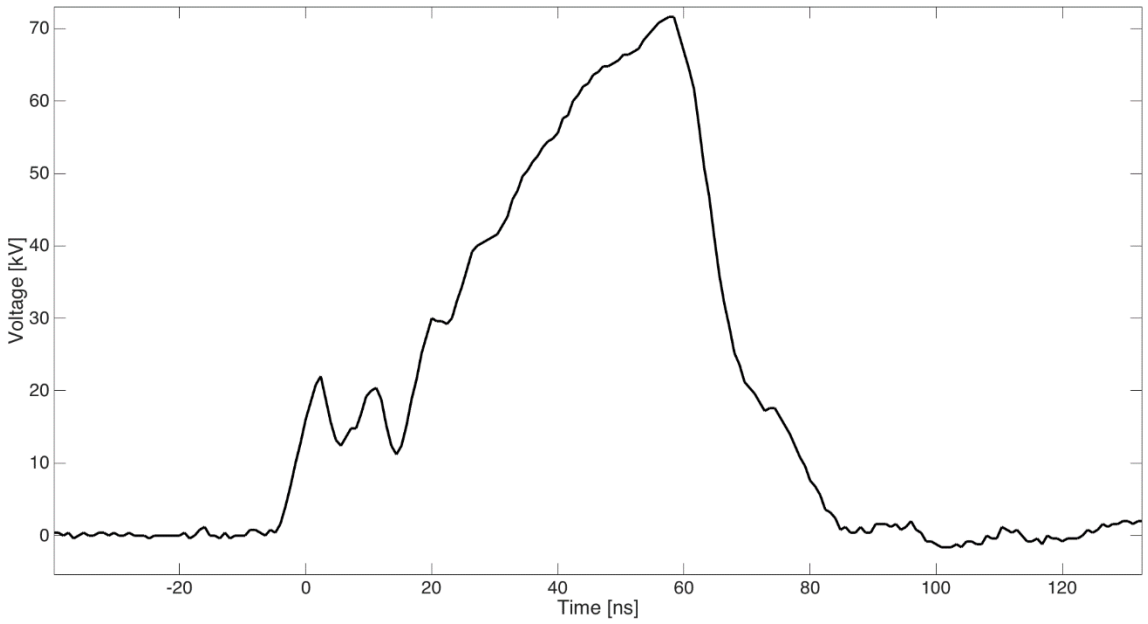

Figure 55: Typical voltage drop across the .2 cm thick ferrite metamaterial composite

6.3.1 Ferrite Continuous Distribution

Initially, breakdown tests were performed on disks made with a continuous distribution, with each disk containing one of the five type of ferrites used in this study. Table 6 shows the average breakdown voltage and maximum electric field measured for each material. MMU1 shows the highest breakdown voltage of 32.76 kV and a maximum electric field of 163.79 kV/cm. MMU3 was the second highest with the other three materials having breakdown voltage around 25kV.

Table 6: Breakdown and field properties for each type of .2 cm metamaterial composite made with a continuous distribution

Material	Average Breakdown Voltage [kV]	Maximum Electric Field [kV/cm]
MMU1	32.76	163.79
MMU2	24.80	124.00
MMU3	29.79	148.93
MMU4	24.82	124.11
MMU5	23.98	119.89

Figure 56 shows a plot of Weibull statistics for each of the five types of ferrite composites. MMU1 has demonstrated the best ability to hold off higher voltages as compared to the other materials. However, the cumulative probability of breakdown for MMU2 composites show a Weibull plot with a much higher slope than any of the others. This increased slope indicates that as higher voltages are applied to MMU2, its probability of breakdown only increases marginally. For the continuous distribution, the variance in breakdown characteristics between each material is best described by a change in the lattice structure that is a result of the varying ratio of Ni to Zn content.

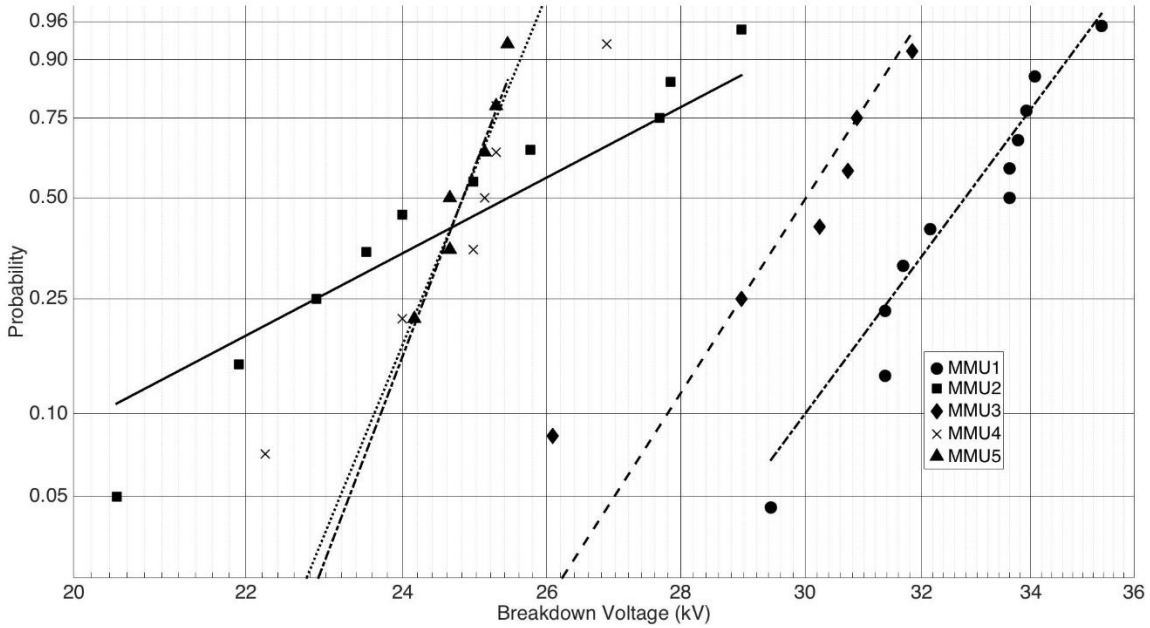

Figure 56: Weibull statistics for all five ferrite types with a continuous distribution .2 cm in thickness

6.3.2 Bimodal Ferrite Distribution

In extending the study to a bimodal distribution only, MMU1 and MMU3 were investigated. This down selection was due to limited time and resources. Since MMU1 and MMU3 showed the best breakdown characteristics in the continuous distribution it was believed that they would show the greatest increase in the bimodal case. Figure 57 shows the Weibull plot obtained from testing multiple MMU1 disks that were .2 cm thick on average. It is also interesting to note that a very similar pattern is seen in the bimodal data for MMU1 as was seen in the continuous distribution

data. The clumping of the breakdown on the Weibull plot can be interpreted as there being multiple breakdown modes [34].

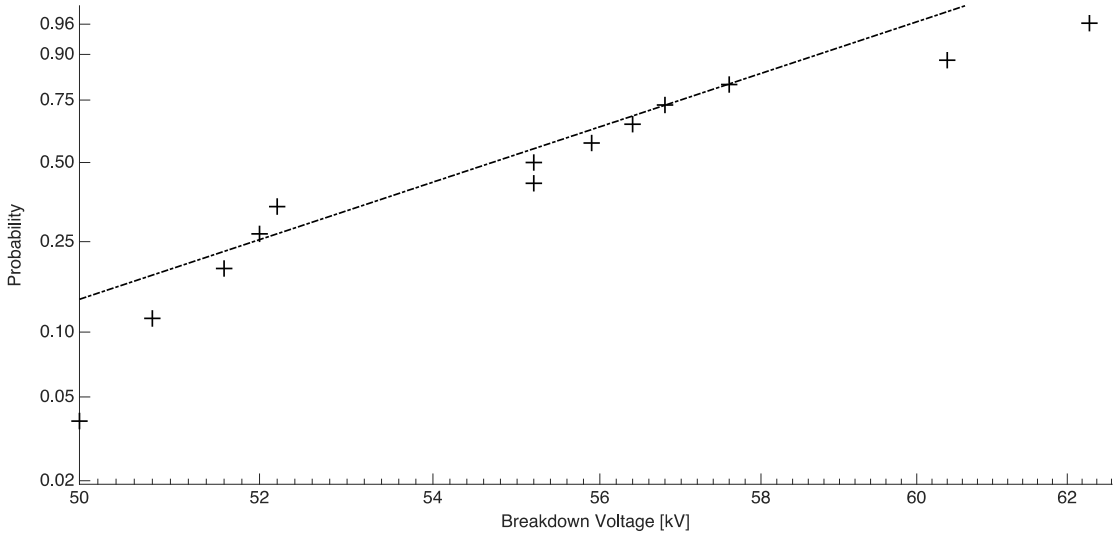

Figure 57: Weibull statistics for bimodal distribution of MMU1 ferrite .2 cm thick.

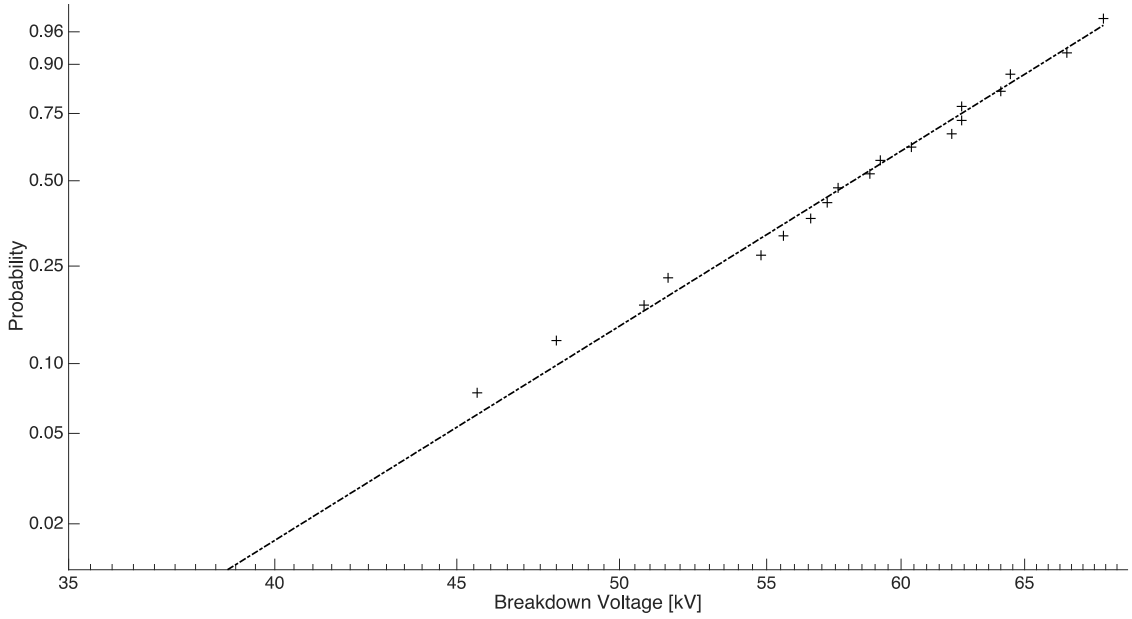

Figure 58: Weibull statistics for bimodal distribution of MMU3 ferrite .2 cm thick

Table 7 shows the average breakdown voltage, average electric field, and maximum electric field measured during testing. Comparing these results to Table 6 we see that the average breakdown voltage for MMU1 and MMU3 have increased by 56% and 90% respectively. This substantial increase in voltage hold off is attributed to the increased structure in the composite. The use of an ordered distribution with fixed particle sizes allows for the assurance of a homogeneous mixture of silane binder and ferrite particles. This mixture allows the electric field energy to spread more evenly throughout the composite and due to the high dielectric strength of the silane, high breakdown voltages can be achieved.

Table 7: Average breakdown voltage, average electric field, and maximum electric field measured for bimodal MMU1 and MMU3 composites

Material	Average Breakdown Voltage [kV]	Average Electric Field [kV/cm]	Maximum Electric Field [kV/cm]
MMU1	55.11	275.55	294.63
MMU3	56.59	266.01	309.50

6.3.3 Trimodal Ferrite Distribution

As in the bimodal case, for the trimodal distribution we further narrowed our use of ferrite. MMU1 was the only ferrite that was tested at this stage. The selection was made based on evaluating each of the design goals for the material. While MMU1 and MMU3 had similar breakdown strengths at the bimodal level, the electromagnetic properties that will be discussed in the next chapter highlighted MMU1 as the best path forward.

Figure 59 shows the Weibull plot that was obtained from disks made with a trimodal distribution of MMU1 ferrite. This plot shows that the overall voltage hold-off has decreased from the bimodal case. The average breakdown voltage is 33.89 kV and the average electric field sustained is 169.44 kV/cm which are both comparable to the results seen in the continuous distribution case. The decrease in breakdown voltage can be attributed to the decrease in silane density in the trimodal composite. At the size ratio of $10^{3,}$ a void percentage of less than 5% can be expected, which means that less than 5% of the composite is silane. Therefore, even though the particle distribution is highly ordered, the lack of dielectric binder results in a reduction in the electric field breakdown in the bulk of the material. Table 8 shows the average breakdown voltage, average electric field, and maximum electric field measured during testing.

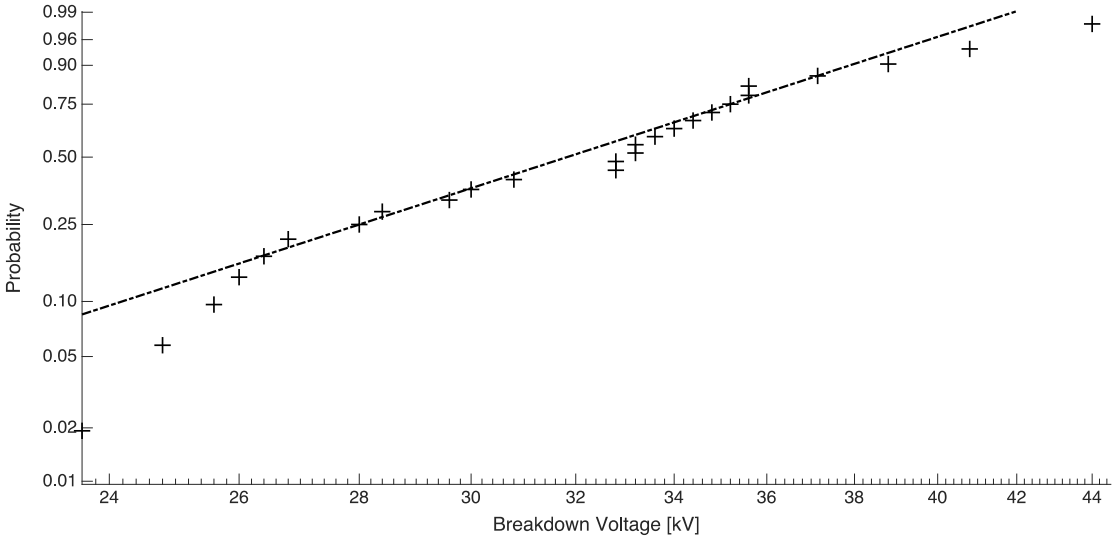

Figure 59: Weibull statistics for a trimodal distribution of MMU1 ferrite powder .2 cm thick

Table 8: Average breakdown voltage, average electric field, and maximum Electric field measured for trimodal MMU1 composites .2 cm thick.

Material	Average Breakdown Voltage [kV]	Average Electric Field [kV/cm]	Maximum Electric Field [kV/cm]
MMU1	33.89	169.45	262.62

In this work, the dielectric strength of the composites was characterized under pulsed conditions which is required to ensure the composites can survive the very high electric fields present in high power antennas. In many cases, the dielectric strength of the composites can be the limiting factor in the power handling capability of the antenna. A high dielectric strength is also critical for compact systems in which a high volumetric energy density is required. Several dielectric strength test methods involve the application of nearly DC voltage or a slowly rising voltage waveform across the sample. In this work, the dielectric strength of the composites was characterized under pulsed conditions. The fast rise time of the applied voltage more accurately replicates the conditions of application in a high power antenna. In particular, a very fast rise time pulse would be applied in an impulse radiating antenna (IRA), so the test method most directly

approximates composite incorporation into an IRA. An antenna driven by a high power resonant signal will also encounter very high dV/dt values, so the test conditions are also relevant for establishing peak electric field values in pulsed ring-down antennas and other transient RF applications. The diagnostics measuring the voltage across the sample limit the practical rise time of the applied pulse. The rise time must be slow enough that the diagnostics can accurately measure the peak voltage across the sample.

6.3.4 Barium Titanate Ferrite Composites Voltage Breakdown tests

Multiple discs of barium-titanate ferrite composite were made with varying thickness (.1 cm, .15 cm, .2 cm, and .25 cm) and tested with the PA-80 pulser. All of the tests were plotted with a Weibull probability fit to show probability of breakdown as a function of voltage. Figure 60 shows the Weibull statistics of all four thicknesses. The .1 cm, .15 cm, and .2 cm tests all follow similar probability patterns, with increased voltage breakdown as the thickness increases. The .25 cm testing does not fit the probability as well as expected due to outliers and faults in the test samples. On average the discs showed a breakdown voltage around 241.6 kV/cm.

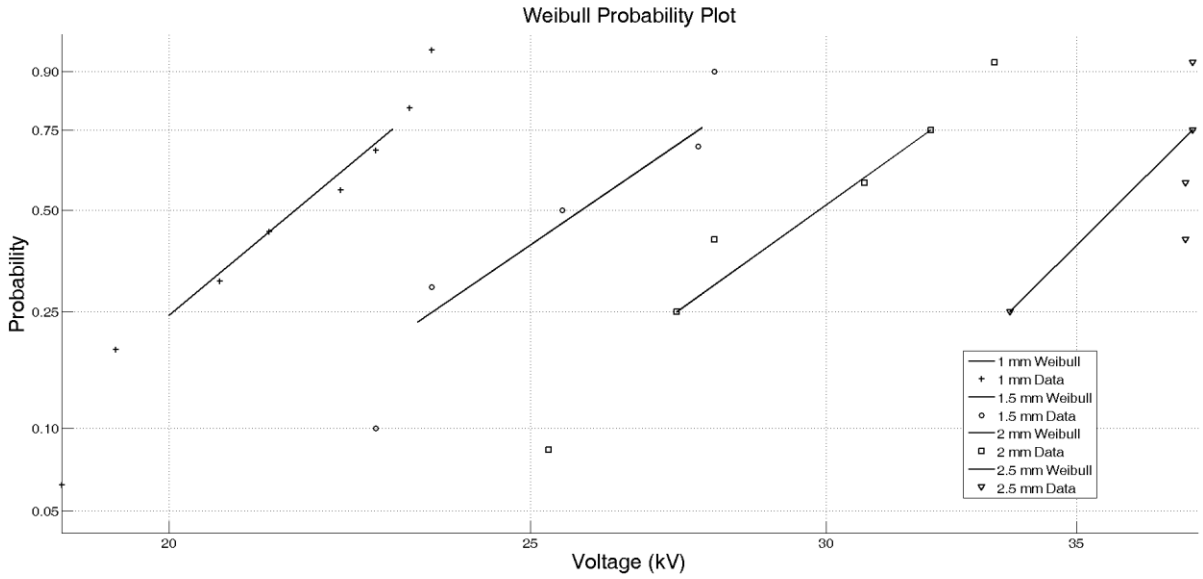

Figure 60: Test Sample Thickness Comparison

The first set of voltage test disks were made using 45 μm powder, but for increased voltage hold-off more particle sizes are necessary. The three particle sizes to be used in multiple mode samples are 100 nm (small), 5 μm (medium), and 25-45 μm (large) particles. These three sizes were then tested individually to assess their single-mode voltage strength. The results of the single-

mode testing with disks that were .2 cm thick on average can be seen in Figure 61. The medium and large particles have similar slopes, while the smaller particles have a less pronounced slope. This occurs because the nanometer particles are made of a different ferrite material with different density and fractions of nickel and zinc. All three particle sizes breakdown between 50 and 150 kV/cm. The small particles hold off more voltage, and the large particles hold off the least. This is consistent with the theory that denser composites will hold off more voltage. The smaller particles fill more of the total volume than the large particles, so the density is higher.

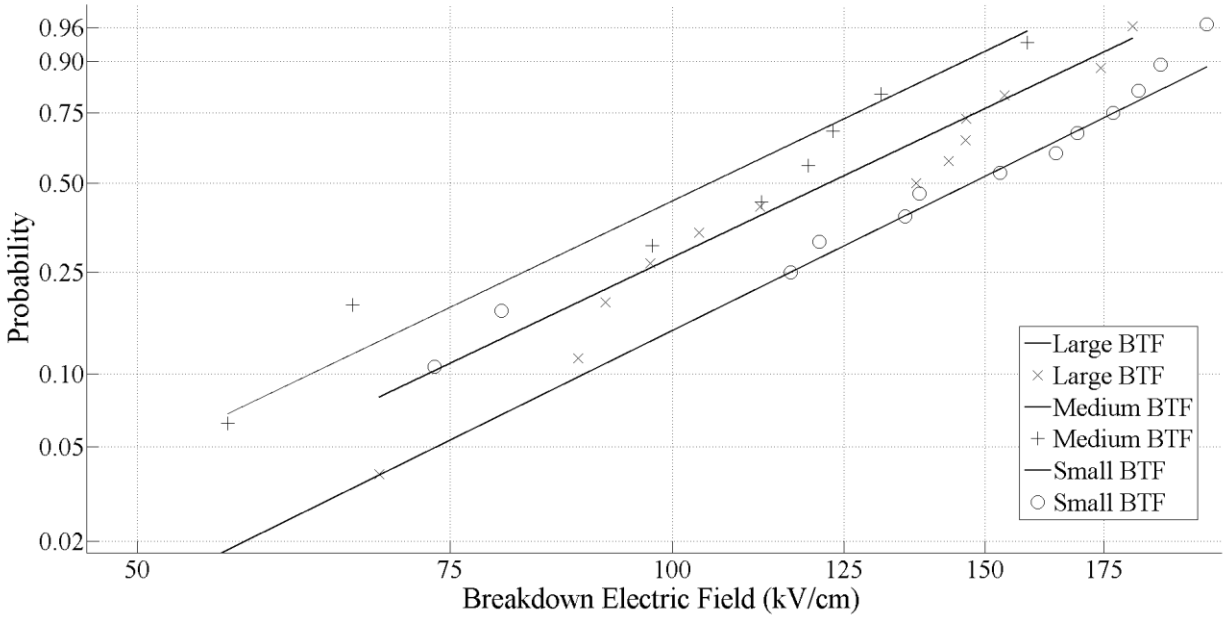

Figure 61: Single Mode Particle Size Comparison of BTF Composites .2 cm thick

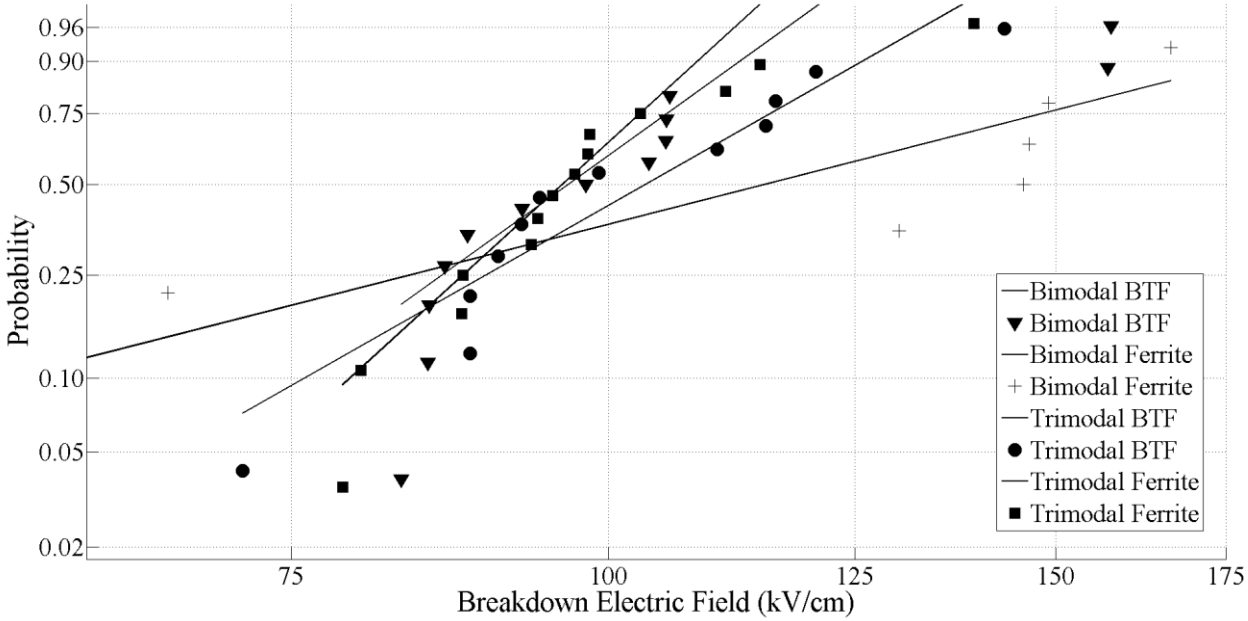

Figure 62: Trimodal and Bimodal Breakdown of BTF Composites .2 cm thick

The composites were prepared and tested with bimodal and trimodal mixes and samples .2 cm thick. Figure 62 shows the voltage breakdown comparison of all the multiple mode composites. The bimodal BTF composite is the only composite that shows a significant change from bimodal mix to trimodal mix. The density of the composite is increased, and the voltage hold-off also increases. The ferrite composites do not significantly increase the voltage strength with the increased density.

An optical microscope was used to visually analyze the breakdown of the composites. Most of the breakdown of the material occurred through the bulk of the test discs, as seen in Figure 63. There is branching across the material, not one single column of breakdown which is expected in a composite material that is not extremely dense. Some breakdown tests do break at the electrode edge (Figure 64), meaning the resistivity of the electrodes is too low but the material hold past the voltage strength of the electrodes.

Figure 63: Bulk Material Breakdown

Figure 64: Electrode Edge Breakdown

7. Conclusion

The scope of this work was to develop a multiferroic metamaterial with permittivity and permeability values above one with high breakdown voltage. The metamaterial was developed using ferromagnetic phase of nickel-zinc ferrite and a ferroelectric phase of barium titanate and confirmed with SEM, TEM, and ICP-AES analysis. Composites of this material were then developed forming barium-titanate ferrite discs (BTF) and compared to ferrite composites.

Five different types of Ni-Zn ferrite powders were used as the magnetic inclusion into a low-dielectric constant silane binder. This combination formed a double-positive metamaterial composite. The five types of ferrites differed only in their ratios for Ni to Zn in the ferrite lattice. This new type of composite was specifically engineered to present values of both permittivity and permeability greater than unity while also demonstrating high dielectric strength. Such parameters allow for improved impedance matching over typical dielectric materials that have only a positive permittivity component. This material was shaped by common mold pressing and is fully machinable.

Three different particle distributions were investigated in order to examine how density and composite order effected the dielectric strength and electromagnetic frequency response. The dielectric strength of each composite was tested under pulsed conditions and the electromagnetic frequency response was tested using a standard transmission/reflection method.

Initially a continuous distribution was utilized and samples tested were .2 cm on average. MMU1 shows the highest breakdown voltage of 32.76 kV and a maximum electric field of 163.79 kV/cm. MMU3 was the second highest with the other three materials having breakdown voltage around 25kV. For these materials the impedances are within 50% of free space up until about 2 GHz. At this frequency we observe a relative wave velocity of between .13 and .06 corresponding to a size reduction factor of between 7.7 and 16.7.

The bimodal distribution showed a significant increase in the voltage hold off of the materials tested. The average breakdown voltage for MMU1 was 55.11 kV for a 0.2 cm thick disk, which translates to an electric field of 275.55 kV/cm. It was shown that average breakdown voltage for MMU1 and MMU3 increased by 56% and 90% respectively compared to the continuous distribution tests. For the electromagnetic frequency response size reductions of 4.8 and 4 at 2 GHz were observed for MMU1 and MMU3 respectively.

The trimodal distribution showed a reduction in breakdown voltages as compared to the bimodal tests. This is believed to be due to the decreased silane density in the trimodal composite. The average breakdown voltage is 33.89 kV and the average electric field sustained is 169.44 kV/cm, with a sample .2 cm thick, which are both comparable to the results seen in the continuous distribution case. This material presents an impedance that is within 50% of the free space value up until 1.5 GHz, and at 2 GHz a size reduction of 5.1 can be obtained.

The BTF composites show increased permittivity and reduced permeability in comparison to the ferrite composites. The magnetic losses decrease drastically with the separation of magnetic domains. When bimodal and trimodal mixtures were used to fabricate the composites, the densities increased, pushing the permittivity and permeability higher in both composites. The increased density also lowered the dielectric loss of the BTF composites while keeping the magnetic losses much lower than the ferrite composites.

The high-voltage testing of the composites was also completed on both BTF composites and ferrite composites. These discs were tested at high voltage with a PA-80 pulser and high-voltage probes. The average voltage breakdown for the BTF metamaterial was shown to be 214.6 kV/cm while the ferrite composites were higher around 300 kV/cm. The ferrite composites have a higher breakdown voltage because of the single phase of material present in the composites. The barium titanate adds an extra dielectric layer in the composite. Increasing the density of the composites using bimodal and trimodal mixing methods does not show increased material breakdown strength, but the improved electromagnetic properties are substantial.

The BTF composite does present a unique method for insulating the ferromagnetic particles and lowering magnetic loss. For this material to be viable in high-powered and high-frequency applications, the permeability and permittivity properties need to be closer to the same value. This could be achieved by tailoring the amount of $BaTiO_3$ layered onto the ferrite powders with better control of the precursors in the chemical reactions.

Additional work also needs to be done to incorporate the material into antennas. Large, high peak power antennas could potentially be built with both of the materials developed on this program. However, substantial electromagnetic modeling is required to understand the interaction of the material with the antenna structure. Based on the single shot breakdown tests, compact antennas that could potentially radiate 10-60 GW/cm^2 peak power levels can be reduced in size by factors of 5-8 times, and at this time are theoretically possible. If a long lifetime antenna is required, gigawatt class antennas that are well matched to the free space impedance can potentially be built with these materials. However, additional work is required to optimize the antenna geometries,

and determine the fields that can be radiated into free space without breakdown of the ambient atmosphere.

8. References

[1] http://ieeexplore.ieee.org/xpls/abs_all.jsp?arnumber=1368916&tag=1

[2] Engheta, Nader; Richard W. Ziolkowski (June 2006).*Metamaterials: Physics and Engineering Explorations*.Wiley & Sons. pp. xv, 3–30, 37, 143–150, 215–234, 240–256. ISBN 978-0-471-76102-0.

[3] Q. Q. Wang, Z. Wang, X. Q. Liu, and X. M. Chen, "Improved structure stability and multiferroic characteristics in CaTiO3-modified BiFeO3 ceramics," *Journal of the American Ceramic Society*, vol. 95, pp. 670-675, 2011.

[4] Balanis – antenna theory

[5] C. A. Balanis, Advanced Engineering Electromagnetics, 2nd ed. John Wiley &

Sons, Inc., 2012.

[6] John S. Seybold (2005) Introduction to RF propagation. 330 pp, eq.(2.6), p.22

[7] V. G. Harris, "Modern microwave ferrites," *IEEE Transactions*

on Magnetics, vol. 48, no. 3, pp. 1075–1104, March 2012.

[8] Handbook of Modern Ferrite Materials (pg 213)

[9] Ullah, Zaka; Atiq, Shahid; Naseem, Shahzad (2013). "Influence of Pb doping on structural, electrical and magnetic properties of Sr-hexaferrites". *Journal of Alloys and Compounds* **555**: 263–267

[10] Robert E. Collin, Foundations for Microwave Engineering. New York: McGraw-

Hill Book Company, 1966.

[11] A. Goldman, Modern Ferrite Technology, 2nd ed. Springer, 2006.

[12] R. F. Soohoo, Theory and Application of Ferrites. Prentice Hall Inc., 1960.

[13] Langmuir, Irving (1919). "The Arrangement of Electrons in Atoms and Molecules" (PDF). *Journal of the American Chemical Society* **41** (6): 868–934.doi:10.1021/ja02227a002. Retrieved 2008-09-01

[14] 1] G. Schileo, "Recent developments in ceramic multiferroic composites based on core/shell and other heterostructures obtained by sol–gel routes", *Progress in Solid State Chemistry*, Volume 41, Issue 4, December 2013, Pages 87-98, (http://www.sciencedirect.com/science/article/pii/S0079678613000186)

[15] Mitoseriu L, Buscaglia V. "Intrinsic/extrinsic interplay contributions to the functional properties of ferroelectric-magnetic composites." *Phase Trans* 2006; 79(12):1095e121

[17] Fiebig M. Revival of the magnetoelectric effect. J Phys D-Appl Phys

2005;38(8):R123**e**52.

[18] R. Simpkin, "A derivation of Lichtenecker's logarithmic mixture formula from Maxwell's equations," *IEEE Transactions on Microwave Theory and Techniques*, vol. 58, pp. 545-550, 2010.

[19] C. Furnas, "Voids in Binary Systems: Normal Packing," 1929.

[20] C. Furnas, "Grading Aggregates," Industrial and Engineering Chemistry, vol. 23,

no. 9, pp. 1052-1058, (1931.)

[21] Aderegg, F.O. and Hubbell, D.S., *Proc. Am. Soc. Testing Materials*, 29, Pt 2 (1929)

[22] Jian-Ping Zhou et al, 2012. "Hydrothermal synthesis and properties of NiFe2O4@BaTiO3 composites with well-matched interface" Sci. Technol. Adv. Mater. 13 045001

[23] Everhart, T. E.; Thornley, R. F. M. (1960). "Wide-band detector for micro-microampere low-energy electron currents". *Journal of Scientific Instruments* **37** (7): 246–248. Bibcode:1960JScI...37..246E. doi:10.1088/0950-7671/37/7/307.

[24] Goldstein, G. I.; Newbury, D. E.; Echlin, P.; Joy, D. C.; Fiori, C.; Lifshin, E. (1981). *Scanning electron microscopy and x-ray microanalysis*. New York: Plenum Press. ISBN 0-306-40768-X.

[25] Joseph Goldstein (2003). *Scanning Electron Microscopy and X-Ray Microanalysis*. Springer.ISBN 978-0-306-47292-3. Retrieved 26 May 2012.

[26] Jaung, Mao; Hieftje, Gary (1989). "Simultaneous measurement of spatially resolved electron temperatures, electron number densities and gas temperatures by laser light scattering from the ICP". *Spectrochimica Acta Part B: Atomic Spectroscopy* **44** (8): 739–749

[27] A. M. Nicolson, "Measurement of the Intrinsic Properties of Materials by Time-Domain Techniques," IEEE Transactions on Instrumentation and Measurement, vol. IM-19, no. 4, Nov 1970.

[28] "HP Product Note 8510-3 - Measuring Dielectric Constant with the HP 8510 Network Analyzer.pdf."

[29] J. Baker-Jarvis, E. J. Vanzura, and W. a. Kissick, "Improved Technique for Determining Complex Permittivity with the Transmission/Reaction Method," IEEE Transactions on Microwave Theory and Techniques, vol. 38, no. 8, pp. 1096{1103, 1990.

[30] "PA-80 and PA-100 Trigger Generators," San Leandro, CA.

[31] K. A. O'Connor and R. D. Curry, "High Voltage Characterization of High Dielectric Constant Composites," Power Modulator and High Voltage Conference, 2010.

[32] "DPO7000C Series Digital Phosphor Oscilloscope Quick Start User Manual," 2013. [Online]. Available: http://www.tek.com/oscilloscope/dpo70000-mso70000-manual/mso70000dx-dpo70000dx-mso70000c-dpo70000c-dpo7000c-mso5000b-an

[33] R. B. Abernethy, the New Weibull Handbook, 2006.

Appendix A: Ceramic Magnetics, Inc. Ferrite Data Sheets

Ceramic Magnetics, Inc.
A National Magnetics Group Company

C2050

High Frequency Ni-Zn Ferrite

Typical applications for this general purpose ferrite are Broadband Amplifiers, low end 10 MHz, and H field antennas. Standard core geometries are toroids and baluns for inductive and transmission line coupled transformers.

Typical Properties

Initial Permeability	100
Maximum Permeability	600
Saturation Flux Density	3700 Gauss
Remanent Flux Density	2300 Gauss
Coercive Force	2.0 Oersted
Curie Temperature	340°C
dc Volume Resistivity	10^9 ohm-cm
Bulk Density	4.60 g/cc

Unless otherwise specified, all tests were performed at 10 KHz, 22°C
Bs tested at 1 KHz, 40 Oersted • Br, Hc at 1 KHz, 5 Oersted

Initial Permeability vs. Temperature

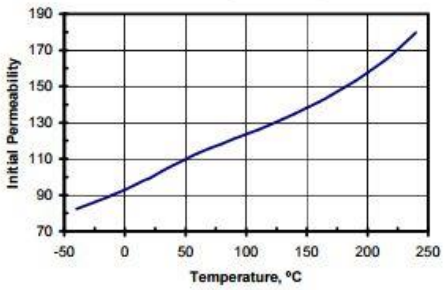

Permeability vs. Flux Density

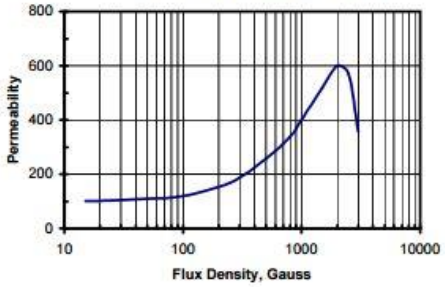

Quality Factor vs. Frequency

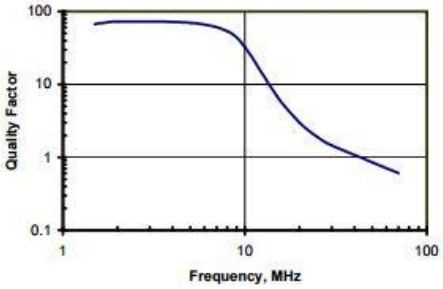

Complex Permeability vs. Frequency

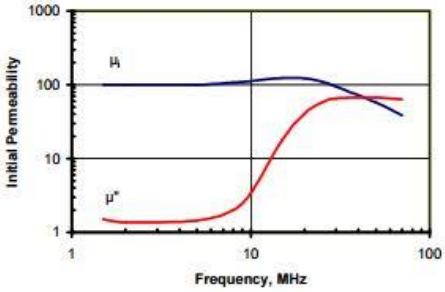

BH Loop Parameters vs. Temperature

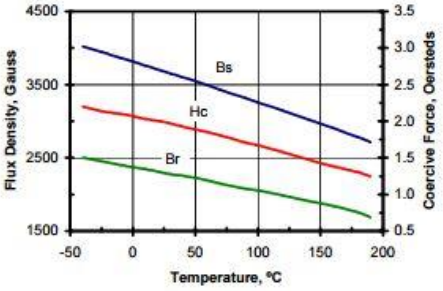

16 Law Drive • Fairfield • New Jersey • 07004 • USA
Phone: (973) 227-4222 • Fax: (973) 227-6735
http://www.cmi-ferrite.com

Rev. 1/15

Ceramic Magnetics, Inc.
A National Magnetics Group Company

C2075

High Frequency Ni-Zn Ferrite

Typical applications for this general purpose ferrite are Broadband Amplifiers, low end 30 MHz, and H field antennas. Standard core geometries are toroids and baluns for inductive and transmission line coupled transformers.

Typical Properties

Initial Permeability	50
Maximum Permeability	270
Saturation Flux Density	3000 Gauss
Remanent Flux Density	950 Gauss
Coercive Force	2.6 Oersted
Curie Temperature	420°C
dc Volume Resistivity	10^8 ohm-cm
Bulk Density	4.60 g/cc

Unless otherwise specified, all tests were performed at 10 KHz, 22°C
Bs tested at 1 KHz, 40 Oersted • Br, Hc at 1 KHz, 5 Oersted

Initial Permeability vs. Temperature

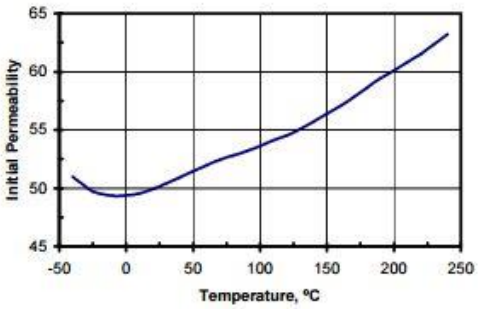

Permeability vs. Flux Density

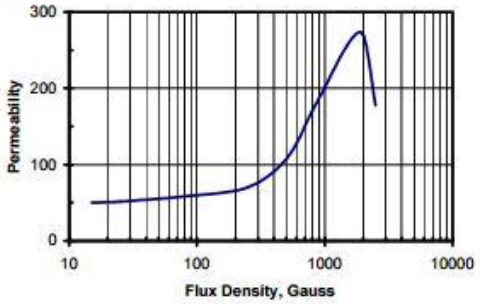

Quality Factor vs. Frequency

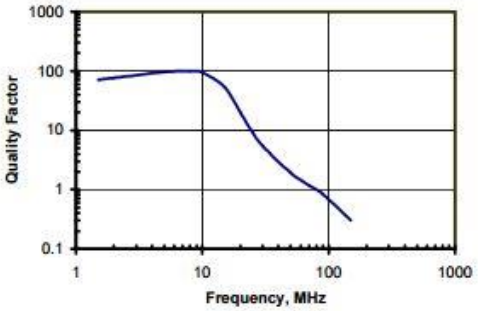

Complex Permeability vs. Frequency

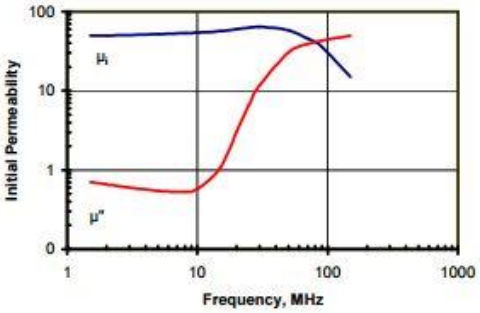

BH Loop Parameters vs. Temperature

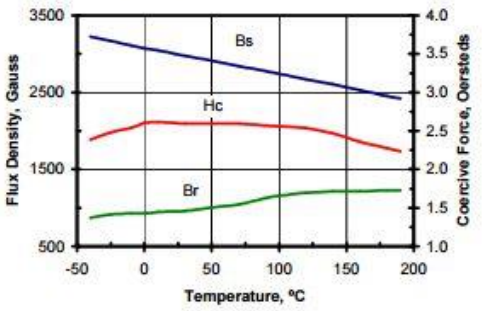

16 Law Drive • Fairfield • New Jersey • 07004 • USA
Phone: (973) 227-4222 • Fax: (973) 227-6735
http://www.cmi-ferrite.com

Rev. 1/15

Ceramic Magnetics, Inc.
A National Magnetics Group Company

CMD5005 General Purpose, High Frequency Ni-Zn Ferrite

The high permeability, high resistivity, narrow BH loop, and closed porosity of CMD5005 make it ideal for broadband transformer, vacuum, fast-pulse, inductive, and RF applications. An excellent choice for transformers in the frequency spectrum from 1 through 100 MHz, current transformers for EMP, and deflection magnets in particle accelerators.

Typical Properties

Initial Permeability	2100
Maximum Permeability	5500
Saturation Flux Density	3300 Gauss
Remanent Flux Density	1300 Gauss
Coercive Force	0.12 Oersted
Curie Temperature	130°C
dc Volume Resistivity	10^{10} ohm-cm
Bulk Density	5.27 g/cc

Unless otherwise specified, all tests were performed at 10 KHz, 22°C

Bs tested at 1 KHz, 20 Oersted • Br, Hc at 1 KHz, 5 Oersted

Initial Permeability vs. Temperature

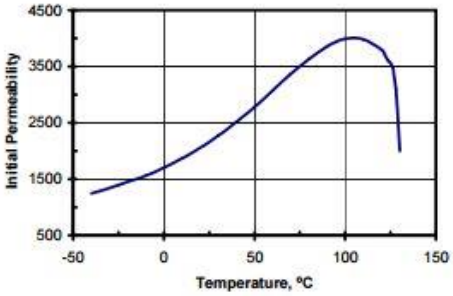

Permeability vs. Flux Density

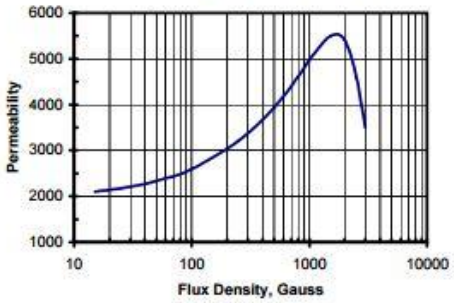

Quality Factor vs. Frequency

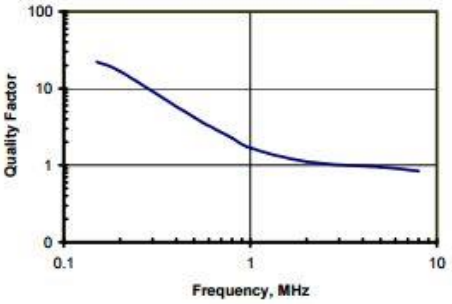

Complex Permeability vs. Frequency

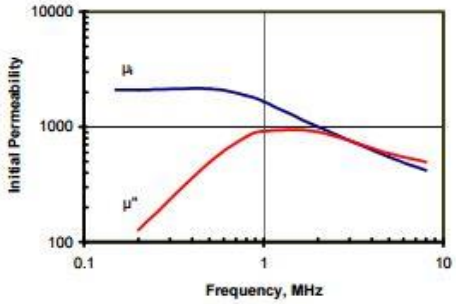

BH Loop Parameters vs. Temperature

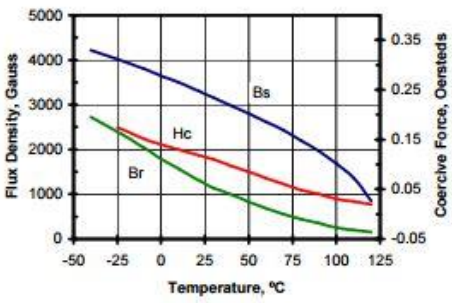

16 Law Drive • Fairfield • New Jersey • 07004 • USA
Phone: (973) 227-4222 • Fax: (973) 227-6735
http://www.cmi-ferrite.com

Rev. 1/15

Ceramic Magnetics, Inc.
A National Magnetics Group Company

N40

High Frequency Ni-Zn Ferrite

N40 is a Ni-Zn ferrite containing cobalt which has a suitable Q for inductive devices in the 1 to 100 MHz frequency range.

Typical Properties

Initial Permeability	15
Saturation Flux Density	2500 Gauss
Remanent Flux Density	950 Gauss
Coercive Force	8.0 Oersted
Curie Temperature	600°C
dc Volume Resistivity	10^{10} ohm-cm
Bulk Density	4.80 g/cc

Unless otherwise specified, all tests were performed at 10 KHz, 22°C
Bs, Br, Hc tested at 1 KHz, 40 Oersted

Initial Permeability vs. Temperature

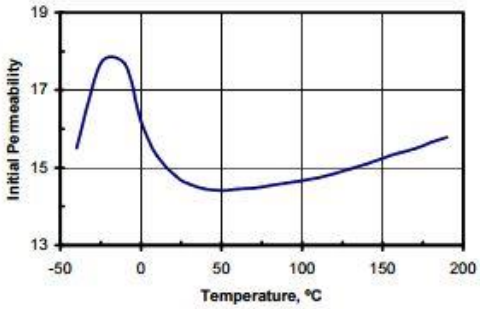

Permeability vs. Flux Density

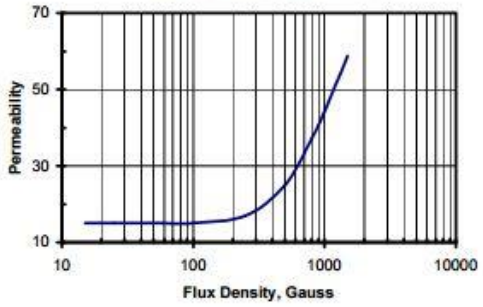

Quality Factor vs. Frequency

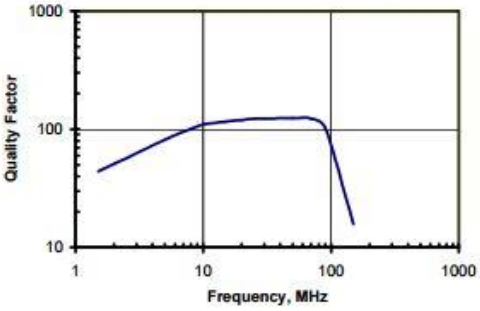

Complex Permeability vs. Frequency

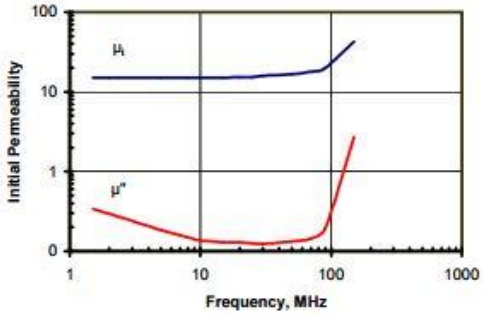

BH Loop Parameters vs. Temperature

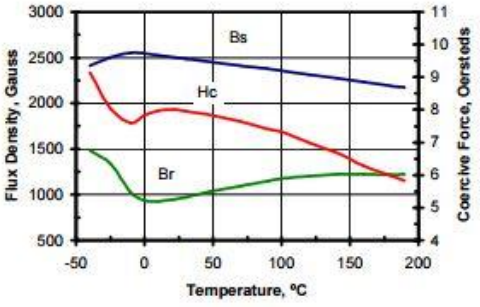

16 Law Drive • Fairfield • New Jersey • 07004 • USA
Phone: (973) 227-4222 • Fax: (973) 227-6735
http://www.cmi-ferrite.com

Rev. 1/15

Ceramic Magnetics, Inc.
A National Magnetics Group Company

XCK

High Frequency Ni-Zn Ferrite

This material is suitable for fixed frequency operation at 13.5 MHz with a high Q and permeability of 125. Standard core geometries are toroids and baluns for inductive and transmission line coupled transformers with bandwidth in the 5 to 50 MHz range.

Typical Properties

Initial Permeability	125
Maximum Permeability	350
Saturation Flux Density	2500 Gauss
Remanent Flux Density	650 Gauss
Coercive Force	0.95 Oersted
Curie Temperature	400°C
dc Volume Resistivity	10^9 ohm-cm
Bulk Density	4.25 g/cc

Unless otherwise specified, all tests were performed at 10 KHz, 22°C
Bs tested at 1 KHz, 40 Oersted • Br, Hc at 1 KHz, 5 Oersted

Initial Permeability vs. Temperature

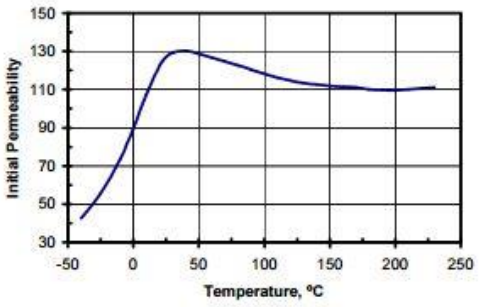

Permeability vs. Flux Density

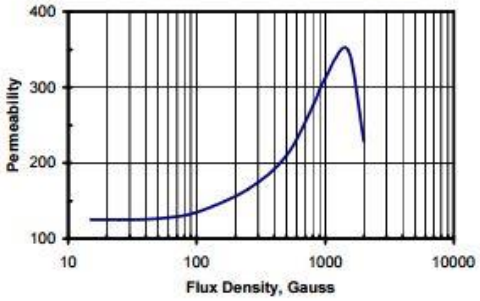

Quality Factor vs. Frequency

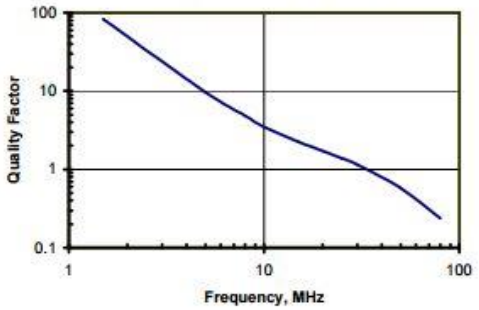

Initial Permeability vs. Frequency

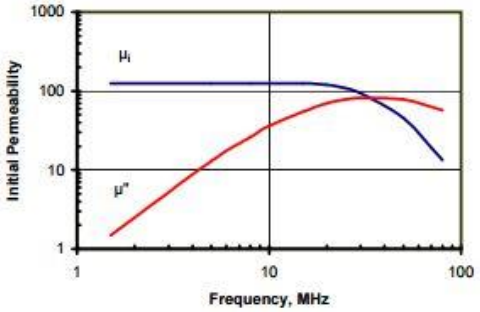

BH Loop Parameters vs. Temperature

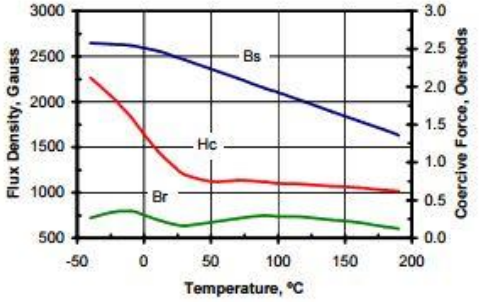

16 Law Drive • Fairfield • New Jersey • 07004 • USA
Phone: (973) 227-4222 • Fax: (973) 227-6735
http://www.cmi-ferrite.com

Rev. 1/15

Appendix B: Conference Presentations and Journal Articles

Three papers were presented at the 2015 IEEE International Pulsed Power Conference. The topics of the papers include 1. Ferrite-based composites; 2. Core-shell composites of barium titanate-coated ferrites; and 3. Antenna concepts based on double-positive metamaterials. The conference was held in Austin, TX from May 31 – June 4, 2015.

Two journal articles have been written, one has been accepted and the other is being edited.

The four manuscripts of completed articles are presented in the following pages.

Publication is pending for all manuscripts.

HIGH VOLTAGE BREAKDOWN ANALYSIS OF NICKLE-ZINC FERRITE DOUBLE-POSITIVE METAMATERIALS*

Aric M. Pearson, Randy D. Curry, Kelli M. Noel, Sarah A. Mounter, Kevin A. O'Connor
Center for Physical and Power Electronics, University of Missouri
349 Engineering Building West, Columbia, MO 65211 USA

Abstract

Metamaterials are currently under development to reduce the size of high power antennas. These materials may also have applications in other high power, dielectric-loaded components, including nonlinear transmission lines. A new procedure has been developed at the University of Missouri-Columbia that produces a double-positive metamaterial by combining nickel-zinc ferrite powders with a dielectric binder. The resulting composite is a machinable bulk material produced at significantly lower temperatures than sintered components. Previous measurements have shown this material to possess positive relative permeability and permittivity values in the range of 4 to 6 for frequencies between 200 MHz and 2 GHz. The dielectric strengths of five different types of ferrite-based composites were measured to evaluate the potential of these materials for high power applications. A pulser with a magnitude up to 100 kV and rise time on the order of tens of nanoseconds was used to determine the dielectric strength of disks with a diameter of 2.54 cm and a thickness of 2 mm. This work presents a statistical analysis of the dielectric strength data and projects the power handling capabilities of the composites.

I. INTRODUCTION

Metamaterials are artificially fabricated substances that have electromagnetic properties not found in nature. As stated by Balanis [1], materials are usually classified into four categories based on their permittivity, ϵ [F/m], and permeability, μ [H/m].

Figure 1 presents a characterization of double positive materials (DPS) along with our goal for new materials being developed. Most materials found in nature are double-positive. However, most good dielectrics have a relative permeability of one, and most magnetic materials are either conductive or otherwise unsuitable for high power applications. The Center for Physical and Power Electronics at the University of Missouri – Columbia is investigating double-positive metamaterial composites designed for high power applications. These composites have been shown to have permittivity and permeability values in the range of 4 to 6 for frequencies between 200 MHz and 2 GHz.

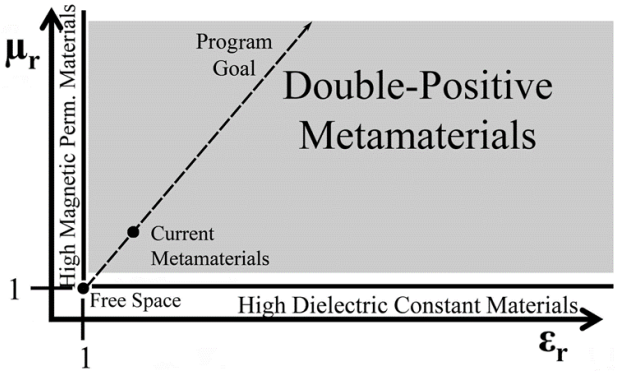

Figure 1. Classification of each type of metamaterial into a distinct quadrant based on its properties.

Double-positive metamaterials have been produced by introducing ferrite powders into a low dielectric constant polymer, using the powders as filler material surrounded by a dielectric matrix. This fabrication process produced a material with low to moderate values of permittivity and permeability while at the same time demonstrating strong mechanical and processing properties. The highly machinable nature of this material is due to the use of a dielectric polymer that can be pressed into any shape and is easily processed using standard milling and shaping techniques. This procedure of producing the composite also requires heating to only 73°C as opposed to the much higher temperatures required for sintering ceramics [2].

Historically, miniaturization of antennas with materials has focused on loading the antenna volume with high permittivity dielectrics ($\mu_r = 1$) in order to reduce the relative wave velocity in the antenna, as described by Equation 1 [3], [4].

$$V = \frac{c}{\sqrt{\epsilon_r \mu_r}} \qquad (1)$$

* Work was supported through the Office of Naval Research contract N0001413-1-0516.

radiation efficiency and degradation of the far field pattern [5]. Such limitations can be overcome by using a material with positive values of both μ_r and ϵ_r [6].

$$Z_m = Z_0 \sqrt{\frac{\mu_r}{\epsilon_r}} \qquad (2)$$

Equation 2 shows how the impedance of an electromagnetic wave in a material, Z_m, relates to that of free space. Increasing only the relative permittivity, ϵ_r, leads to an impedance mismatch of the antenna. However, incorporation of a DPS metamaterial allows for the impedance ratio to be controlled while still benefiting from the size reduction indicated in Equation 1.

Thus far, metamaterials have mainly been investigated for reducing the size of low voltage, handheld devices [2], [5]. This paper instead focuses on the dielectric strength of materials designed for high voltage applications where power handling is an important factor. The subsequent sections describe the production of the composite materials as well as outline the dielectric strength test procedure. This is followed by an analysis of the preliminary results.

II. MATERIAL PRODUCTION

The dielectric strength of five different ferrite based metamaterials was tested. Each composite was given a unique label, MMU1 thru MMU5. For the purpose of testing, each metamaterial was pressed into a disk with a 2.54 cm diameter. The procedure used for the production of the metamaterial samples was adapted from the procedure used previously at the University of Missouri – Columbia for the production of nanodielectric composites [7]. A die was filled with a specific ferrite powder mixed with a dielectric binder in a predetermined ratio of 6:1. Particles in each of the ferrite powders were sized to be between 45 and 52 μm and an acoustic mixer was used to achieve a uniform mixing of the ferrite powders with the binder. A non-reactive mold release was applied to the base plate and plunger of the die before pressing in order to minimize possible stress related defects. Once the mixture was placed into the die, it was put under pressure for 2 hours and heated to 73°C.

After pressing, each disk was machined with a CNC mill to reduce the thickness and to ensure a constant thickness over the entire disk. Each face of the milled disks was then polished in order to avoid unwanted field enhancement that would lead to premature breakdown. A DC sputter coated was used to place platinum electrodes onto each side of the disk and each electrode was coated with a layer of conductive silver paint. Each disk was made with four test sites on the front side and one large test site on the back side, as shown in Figure 2.

Figure 1. Image of front side (left) and back side (right) electrodes that were sputtered onto each disk.

III. DIELECTRIC STRENGTH TEST STAND

Measurement of the maximum electric field that a material can sustain before breakdown is a major factor in projecting the power handling capabilities of the composite. The dielectric strength of the metamaterial composite was characterized under pulsed conditions. A PA-80 pulse generator from L-3 Communications Pulse Sciences was the high voltage source for the dielectric strength test stand [8]. Figure 3 shows a schematic of the circuit.

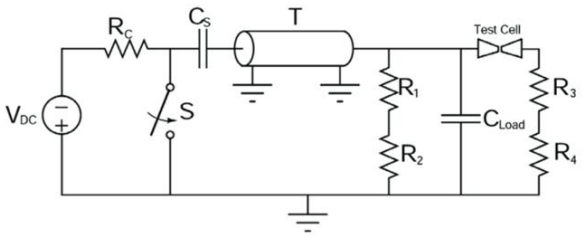

Figure 2. Circuit diagram of pulsed dielectric strength test stand [7].

A 75 nF capacitance, C_s, was resistively charged. Once charging was complete, switch S was closed. This discharged C_s into a transmission line T. The transmission line was a 50Ω cable of RG-218/U. The transmission line terminated into a high impedance load consisting of parallel arrangement of the dielectric test cell, a capacitance, C_{load}, of 0.54 nF, and a high resistance, $R_1 + R_2$. Since C_{load} is much smaller than C_s and the resistance of $R_1 + R_2$ is very high, the voltage across the test cell was able to reach a max peak of around 100kV [3]. The 10% to 90% risetime of the system has been measured to be approximately 60 ns. Figure 4 shows a photograph of the pulse generator, left, and the test cell, right. The test cell consists of an acrylic housing in which Shell Diala dielectric oil was used as a voltage background insulator.

The voltage diagnostics consisted of two North Star high voltage probes with a 1000:1 ratio. One probe measures each side of the test cell with a Tektronix

DPO7254 Digital Phosphor Oscilloscope [9]. To protect the sensitive electronics in the scope, a Faraday cage was built to isolate it from the electric fields generated by the high voltage supply and PA-80 pulser. Figure 5 shows a close up of the test cell and the high voltage probes. Tests were performed on disks 2.54 cm diameter and 2mm thick with four test sites were prepared on each disk.

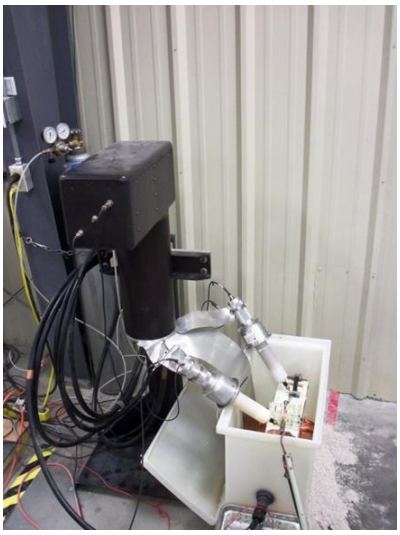

Figure 1. PA-80 pulse generator on the left, test cell with high voltage probes on the right.

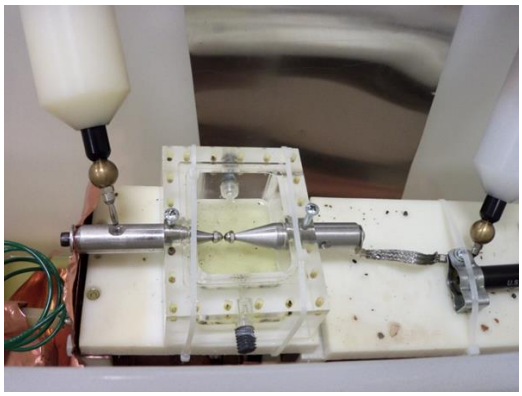

Figure 2. Close up of test cell and North Star high voltage probes.

IV. RESULTS AND ANALYSIS

Figure 6 shows an example of a typical breakdown trial. The trace labeled HV Source is the signal observed at the output of the PA-80 pulse generator. The other trace is the voltage seen on the other electrode of the metamaterial, and the label identifies the type of ferrite used. The dielectric strength of the composites is characterized by analyzing the peak potential difference between these two signals. Figure 7 shows a typical waveform displaying the voltage across the metamaterial composite. This specific plot shows an N40 disk with a peak voltage of 25 kV.

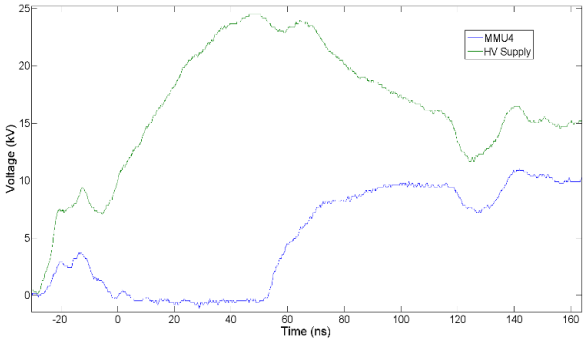

Figure 3. Example waveform of voltage at both sides of test cell.

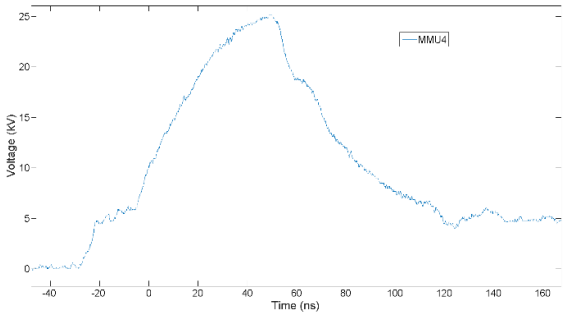

Figure 4. Example waveform of voltage across metamaterial composite.

Table 1 shows the average breakdown voltage and maximum electric field achieved for each material. MMU1 shows the highest breakdown voltage of 32.76 kV and a maximum electric field of 163.79 kV/cm. MMU3 was the second highest with the other three materials having breakdown voltage around 25kV.

Table 1. Breakdown and field properties for each type of 2mm metamaterial composite.

	MMU1	MMU2	MMU3	MMU4	MMU5
Average Breakdown Voltage [kV]	32.76	24.80	29.79	24.82	23.98
Maximum Electric Field [kV/cm]	163.79	124.00	148.93	124.11	119.89

Figure 8 shows a plot of Weibull statistics for each of the five types of ferrite composites. MMU1 shows the best beast ability to hold off higher voltages as compared to the

with a much higher slope than any of the others. This increased slope indicates that as higher voltages are applied to MMU2, it's probability of breakdown only increases marginally. It is currently believed that the breakdown characteristics of each material are strongly linked to the lattice structure of the ferrite used.

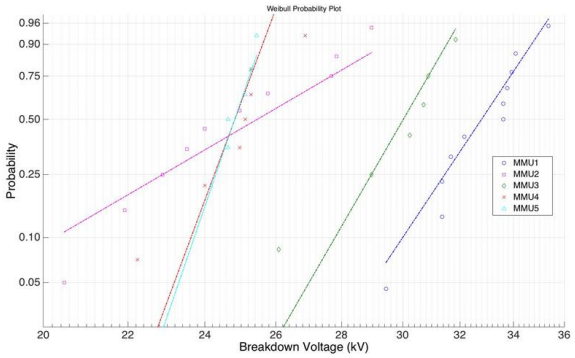

Figure 1. Cumulative probability of breakdown for each type of ferrite composite.

V. FUTURE WORK

The current work is part of an ongoing investigation into DPS metamaterials for high power applications. The next step in this program will involve breakdown tests of the materials at various thicknesses to determine how the maximum electric field scales with disk volume. Also by analyzing data of the permittivity and permeability of each type of metamaterial composite at various frequencies with the dielectric strength data, a specific metamaterial formulation can be selected for design and testing of high power antennas.

VI. SUMMARY

The University of Missouri – Columbia is producing and testing large area, machinable metamaterial composites to reduce the size of high power antennas. Nickel-zinc ferrite powders were incorporated into a dielectric binder matrix material. The resulting composite is a machinable bulk material produced at significantly lower temperatures than sintered components. The dielectric strengths of five different types of ferrite-based composites were measured and the potential of these materials for high power applications was discussed. Currently MMU1 and MMU2 appear to be the best for further development for use in high power applications due to MMU1 having the highest maximum of electric field of 163.79 kV/cm and MMU2 having a breakdown scaling with the lowest slope.

VII. REFERENCES

[1] Constantine A. Balanis, Advanced Engineering Electromagnetics, 2nd ed. Wiley, 2012.

[2] J. L. Mattei, L. Huitema, P. Queffelec, J. F. Pintos, P. Minard, A. Sharahia, B. Jamnier, F. Ferrero, R. Staraj, D. Souriou, and A. Thakur, "Suitability of Ni-Zn ferrites ceramics with controlled porosity as granular substrates for mobile handset miniaturized antennas," IEEE Trans. Magn., vol. 47, no. 10, pp. 3720–3723, 2011.

[3] K. a. O'Connor and R. D. Curry, "High voltage characterization of high dielectric constant composites," 2010 IEEE Int. Power Modul. High Volt. Conf., pp. 159–162, 2010.

[4] K. A. O'Connor and R. D. Curry, "High Dielectric Constant Composite for High Power Antennas," IEEE Pulsed Power Conf., 2011.

[5] P. M. T. Ikonen, K. N. Rozanov, A. V. Osipov, P. Alitalo, and S. a. Tretyakov, "Magnetodielectric substrates in antenna miniaturization: Potential and limitations," IEEE Trans. Antennas Propag., vol. 54, no. 11, pp. 3391–3399, 2006.

[6] G. B. Gentili, P. Piazzesi, C. Salvador, K. L. Wong, W. S. Chen, M. Opt, R. C. Hansen, and M. Burke, "Antennas with magneto-dielectrics," Microw. Opt. Technol. Lett., vol. 26, no. 2, 2000.

[7] K. a O. Connor, J. Smith, and R. D. Curry, "Dielectric Characterization of Polymer-Ceramic Nanocomposites," IEEE Instrum. Meas. Mag., pp. 336–341, 2009.

[8] "PA-80 and PA-100 Trigger Generators." L-3 Communications Pulse Sciences, San Leandro, CA.

[9] "DPO7000C Series Digital Phosphor Oscilloscope Quick Start User Manual." Tektronix, 2013.

THE DIELECTRIC STRENGTH OF HIGH FREQUENCY METAMATERIAL COMPOSITES

Kelli M. Noel, Randy D. Curry, Aric M. Pearson, Kevin A. O'Connor

Center for Physical & Power Electronics, University of Missouri, Columbia, MO 65211

Abstract

Metamaterial composites with both ferroelectric and ferromagnetic phases have promising applications in the field of applied electromagnetics and directed energy. This metamaterial, which integrates the dielectric-ferromagnetic properties into a single composite, was synthesized using a hydrothermal process combining barium hydroxide ($Ba(OH)_2$), titanium dioxide (TiO_2), and nickel-zinc ferrites. The product of this reaction forms a shell of barium titanate around the ferrite particles. The dielectric strength of the resulting metamaterial has been tested and will be reported. The material was pressed with a binder to form discs for breakdown testing. The dielectric and magnetic losses have been measured with an airline waveguide, and the high voltage breakdown of the material was determined using DC measurements as well as nanosecond pulses from a PA-80, 100 KV pulser. The breakdown field of the core-shell material is compared to other known insulator materials.

INTRODUCTION

Materials with both ferroelectric and ferromagnetic properties can be called multiferroics [1]. These metamaterials present many possible uses in electromagnetics and antenna designs such as antenna miniaturization and uses in non-linear transmission lines (NLTL).

Multiferroic metamaterials with tailored permittivity ε_r, and permeability μ_r, can be used to shrink antenna sizes and match impedances. Antenna size can be determined by the wavelength in the material as seen in equation 1, where λ_0 is the free space wavelength. By increasing the ε_r and μ_r of the material used in an antenna the size can be reduced substantially for similar wavelengths. [2].

$$\lambda_D = \frac{\lambda_0}{\sqrt{\epsilon_r \mu_r}} \tag{1}$$

The impedance of a material is also affected by its dielectric properties as seen in equation 2. When using materials with high dielectric constants, the impedance of the material becomes mismatched to free space [3]. Multiferrotic metamaterials with similar ε_r and μ_r values can aid in impedance matching.

$$Z_m = Z_0 \sqrt{\frac{\mu_e}{\varepsilon_r}} \tag{2}$$

Use of ferromagnetic materials and multiferrotics as dielectric material in NLTLs may allow for better pulse sharpening or reduced magnetic losses [4]. The magnetic domains present in multiferrotic metamaterials allow for saturation of the nonlinear permeability and if tailored to the required operational characteristics could have a significant impact on sources, delay lines, and slow wave structures [5]. Such materials could decrease the size of NLTLs and replace more expensive material.

The dielectric strength of multiferroic materials is important to investigate for their application as insulators or pulse generators. For use in high-powered microwave devices the material must withstand relatively high electric field strengths [6]. For use in antennas, higher energy storage can lower the bandwidth of the device [7].

The permittivity and permeability for the synthesized multiferroic metamaterials in this study are being investigated. Using a coaxial airline waveguide and dielectric measurement software we compared various ferrite samples. The magnetic and dielectric constants were measured across a frequency range of 0.2-2 GHz. The dielectric strength of the synthesized metamaterial will be investigated and discussed here.

II. EXPERIMENTAL SETUP

The metamaterial composite was synthesized using a hydrothermal process. $Ba(OH)_2$ and TiO_2 were combined with a 1:1 molar ratio and then ferrite particles were added. The ferrites used were selected from previous

that did not have magnetic cores. The synthesis of the metamaterial was confirmed with analysis in a scanning electron microscope (SEM) and energy dispersive spectroscopy (EDS).

After the metamaterial powders were synthesized and processed, one inch discs were prepared for the high voltage testing. A unique binder was used to create a polymer matrix with the metamaterial powders. A set amount of powder and binder was combined and then formed into 1" discs with a thickness of 3 mm. The discs were then milled to 1 mm in thickness using a CNC mini-mill. Increasing grades of sandpaper were then used to polish the surfaces of the discs. Titanium electrodes were sputtered onto the discs and covered in a thin layer of silver paint for electrical contacts.

The dielectric strength of the metamaterial was tested using a PA-80, 100 kV pulser. The metamaterial samples were over volted until breakdown occurred. The pulses had a 10% to 90% rise time of 60 ns. North Star voltage probes with a 1000:1 voltage ratio were used to measure the voltage difference across the electrodes on the sample. The breakdown voltage of each of the materials were measured using a Tektronix DPO7254 digital phosphor oscilloscope.

III. RESULTS AND DISCUSSION

SEM and EDS results confirmed the presence of both Ni-$ZnFe_2O_3$ and $BaTiO_3$. The EDS spectrum shows points of barium titanate around a central nickel-zinc ferrite particle confirming the core shell structure. The SEM images of the barium titanate synthesized without ferrites indicates individual particle sizes around 100 nm. This leads to the conclusion that the shells around the ferrite particles are on the range of 100 nm, or in intervals of 100nm.

The electromagnetic characteristics of both materials were tested and are summarized in Table 1. The core-shell multiferroic material increases the permittivity, but the permeability is decreased. The reduction in permeability is a result of the decrease in magnetic material present in the composite. The dielectric loss is slightly elevated due to an addition of dielectric material, but the magnetic losses are drastically decreased. This reduction of loss is due to the separation of the magnetic domains in the ferrite cores.

Table 1. Material Characteristics at 1 GHz

Characteristics at 1 GHz	Core Shell	Ferrite
Relative Permittivity	8.8	7.8
Relative Permeability	2.5	5.3
Impedance (Ω)	198	310
Relative Wave Velocity	0.23	0.16
Dielectric Loss	0.02	0.01
Magnetic Loss	0.05	0.8

Multiple 1 mm discs with 4 small area electrodes were investigated using the PA-80 pulser. The oscilloscope displays the input pulse, and resulting signal across the other electrode following breakdown of the material. When the output signal begins to mirror the input signal, breakdown of the material has occurred. The two signals were then subtracted from each other using a MATLAB program to determine the peak voltage breakdown. Figure 1 shows the input and output signals, and Figure 2 is the resulting subtracted signal.

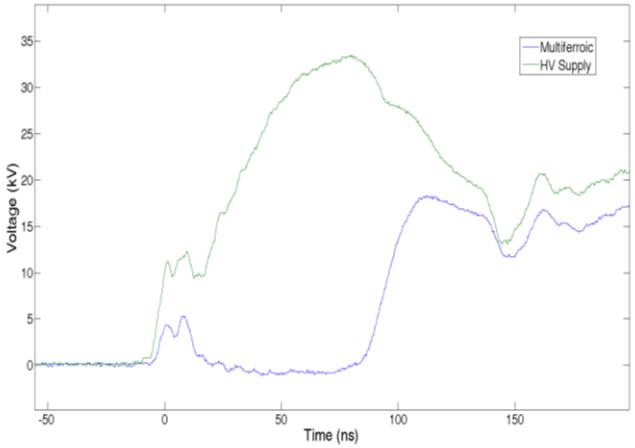

Figure 1. Input and output channels from the high voltage test stand.

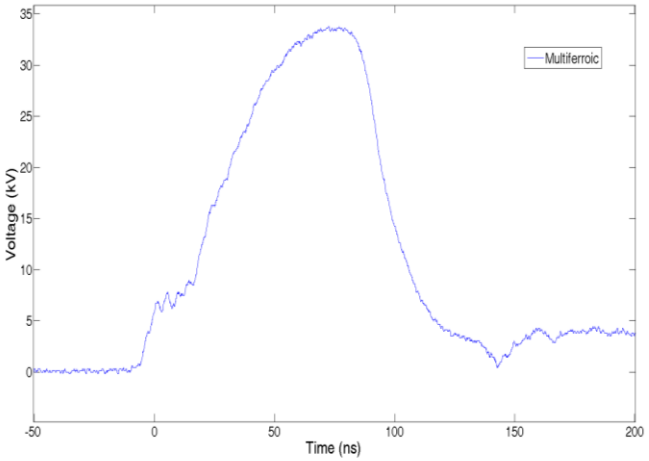

Figure 2. Peak breakdown voltage of metamaterial sample.

The average breakdown of the discs with 1 mm thickness was 21.46 kV/mm. If the breakdown voltage scales linearly, this would result in a breakdown voltage of 214.6 kV/cm. Commercial barium titanate capacitors have been shown to have a breakdown voltage of 90-200 kV/cm [8]. The trials from the voltage breakdown tests were analyzed

functions, and the resulting shape parameter was calculated to be 22.207 and the size parameter was 16.115. The data fit closely to the Weibull distribution indicating that the majority of breakdown for 1 mm samples will occur from about 19 kV to 23 kV.

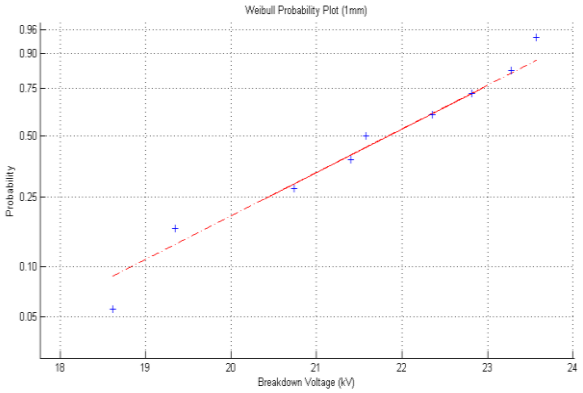

Figure 3. Weibull probability plot with breakdown voltage data.

IV. CONCLUSION AND FUTURE WORK

Multiferroic metamaterial powders were successfully synthesized and machined into test discs. These discs were tested at high voltage with a PA-80 pulser. The average voltage breakdown for the metamaterial was shown to be 21.46 kV/mm and fit a Weibull distribution. The next step is to machine more discs with varying thicknesses and test the voltage breakdown. A volumetric study of the breakdown of the material could then be completed. More trials for each thickness would also show a more likely fit to the Weibull distribution. Modeling the material into applications could be show size reductions in antenna or pulse forming in NLTLs.

V. REFERENCES

[1] G. Schileo, "Recent developments in ceramic multiferroic composites based on core/shell and other heterostructures obtained by sol–gel routes", *Progress in Solid State Chemistry*, Volume 41, Issue 4, December 2013, Pages 87-98, (http://www.sciencedirect.com/science/article/pii/S0079678613000186)

[2] Buerkle, A., and K. Sarabandi. "A Wide-band, Circularly Polarized, Magnetodielectric Resonator Antenna." *IEEE Transactions on Antennas and Propagation* 53.11 (2005): 3436-442. IEEEXplore. Web.

[3] K. A. O'Connor and R. Curry, "High dielectric constant composite for high power antennas," IEEE Pulsed Power Conference, 2011

[4] Solarski, R. C., D. V. Reale, J.-W. B. Bragg, A. A. Neuber, S. L. Holt, J. J. Mankowski, and J. C. Dickens. "High Voltage Solid Dielectric Coaxial Ferrimagnetic Nonlinear Transmission Line." *Pulsed Power Conference* (2013): 1-3. *IEEEXplore*. Web.

[5] Bragg, J.-W. Braxton, James C. Dickens, and Andreas A. Neuber. "Ferrimagnetic Nonlinear Transmission Lines as High-Power Microwave Sources." *IEEE Transactions on Plasma Science* 41.1 (2013): 232-37.*IEEEXplore*. Web.

[6] French, D.M., B. W. Hoff, S. Heidger, and D. Shiffler. "Dielectric Nonlinear Transmission Line." Proc. of Pulsed Power Conference (PPC) 2011, Chicago, IL. 341-45.

[7] Huynh, Adam P., Stuart A. Long, and David R. Jackson. "Effects of Permittivity on Bandwidth and Radiation Patterns of Cylindrical Dielectric Resonator Antennas." *Antennas and Propagation Society International Symposium (APSURSI)* (2010): 1-4.

[8] Rossi, J.O.; Silva Neto, L.P.; de Siqueira, R.H.M. "Study of the ceramic capacitor dielectric for pulsed power", *Pulsed Power Conference (PPC), 2013 19th IEEE*, On page(s): 1 – 4

[9] W. Weibull, "A statistical distribution function of wide applicability," *Journal of Applied Mechanics*, vol. 18, pp. 293-297, 1951

SIMULATION OF COMPACT HIGH POWER ANTENNA CONCEPTS LOADED BY DOUBLE-POSITIVE METAMATERIALS*

K.A. O'Connor and R.D. Curryξ

University of Missouri, Center for Physical and Power Electronics, 349 Engineering Building West Columbia, Missouri, USA

Abstract

An ongoing effort to reduce the size of high power antennas in the VHF and UHF bands investigates loading novel composite materials into the antenna structure. A previous effort developed high dielectric constant composites with a high dielectric strength for high power antennas. The current work aims to develop metamaterials with greater-than-unity values of relative permittivity and permeability. By designing the relative permittivity and permeability, the wave velocity in the antenna can be reduced while also controlling the wave impedance. These new magnetodielectric composite materials provide additional design flexibility over conventional dielectric loading for both traveling wave antennas and resonant antennas in HPM and HPRF applications. While a previous demonstration of dielectric loading of a dielectric resonator antenna utilized a composite with a dielectric constant of approximately 100 for high peak power operation in a very compact form factor, the current work focuses on achieving similar reductions in antenna size using composites with relative permittivity and permeability values of less than 10. Preliminary simulation analyses using CST Microwave Studio have shown the effectiveness of this approach in compact horns and helical antennas operating at frequencies below 1 GHz. This work presents the simulation of antenna concepts using magnetodielectric materials with greater than unity values of the relative permittivity and permeability. Magnetodielectric loading is compared to antennas not loaded with dielectrics and antennas loaded with conventional dielectric or magnetic materials. It is shown that magnetodielectric materials can achieve similar antenna size reduction as antennas with conventional dielectric or magnetic loading while improving the bandwidth.

I. INTRODUCTION

Novel materials are under development to reduce the size of high power antennas. In recent years, three classes of high dielectric constant composite materials were developed at the University of Missouri for high power applications [1]. To operate under high power conditions, the composites were required to have high dielectric strengths and to be fabricated in large bulk pieces. Size reduction of the antennas is based upon the relationship shown in equation (1). The length dimension, l_a [m], of the antenna corresponding to operation at frequency f_a [Hz] is dependent on the permittivity, $\varepsilon_0\varepsilon_r$ [F/m], and the permeability, $\mu_0\mu_r$ [H/m], of the medium in which the wave travels through the antenna.

$$l_a \propto \frac{1}{f_a\sqrt{\varepsilon_0\varepsilon_r\mu_0\mu_r}} \tag{1}$$

The original three classes of composite materials maximized the dielectric constant, ε_r, and the dielectric strength while leaving the relative permeability, μ_r, equal to 1. Some of these composite materials have been demonstrated in compact high power antennas. However, it is often necessary to modify the antenna design when incorporating high dielectric constant materials to maintain acceptable bandwidth and efficiency. It is desirable to have materials that can be directly incorporated into antenna structures to reduce the operating frequency without significant redesign or modification of the antenna. The current effort aims to enable direct loading of antenna structures with magnetodielectric materials to reduce the antenna size without requiring extensive redesign.

By modifying both the relative permeability and dielectric constant of the materials, impedance matching can be improved without altering the design or construction of the antenna, resulting in higher efficiency and bandwidth. Equation (2) shows the relationship of the characteristic impedance, Z [Ω], to the free-space impedance, Z_0 [Ω], the relative permeability, and the relative permittivity [2]. By increasing both the dielectric constant and the relative permeability, the antenna dimensions can be decreased while maintaining the characteristic impedance more closely to the free-space value.

$$Z = Z_0\sqrt{\frac{\mu_r}{\varepsilon_r}} \tag{2}$$

Use of magnetodielectric materials has previously been proposed in the form of sintered ferrites and certain types of metamaterials [2] [3]. It has previously been noted that to increase the bandwidth, it is better to include magnetic materials to contribute a static component of the relative permeability rather than a split-ring structure without magnetic materials [3]. Examples of magnetodielectric metamaterials proposed by other researchers include a

* Work supported by ONR Grant N000140810267

ξ email: CurryRD@missouri.edu

layered structure of dielectrics with interleaving sputtered films of ferromagnetics and periodic structures of magnetic and dielectric components [3] [2]. The current effort uses a core-shell structure to improve dielectric strength with an insulating shell around a magnetic core [4].

Most previous works on antennas with magnetodielectric materials incorporate a double-positive material as a substrate. There are several examples of analysis and experimentation on the use of magnetodielectrics in patch antennas [5] [6] [3] [2]. Other examples include backing a monopole antenna with a magnetodielectric substrate and a coplanar slot antenna [7] [8]. Since applications of magnetodielectric substrates in microstrip-fed antennas have already been demonstrated, this work focuses on loading antennas without a substrate. The following sections will consider a circular horn and a helical antenna. Both antennas have previously been used for high power applications, and dielectric loading has been used to decrease the size of both types of antennas. The size reduction and bandwidth will be compared between unloaded, dielectric-loaded, magnetic-loaded, and magnetodielectric-loaded forms of these antennas.

II. LOADED HORN ANTENNA

Horn antennas have obvious advantages for use with waveguide-fed systems, but the horn dimensions can be a limiting factor for compact systems. Dielectric loading of horns is a well-known option to reduce horn size, but lenses or other design modifications can be necessary to improve matching to free space. To compare dielectric, magnetic, and magnetodielectric loading of a horn antenna, the conical horn shown in Figure 1 with material loading was modeled in CST Microwave Studio. The antenna is fed from a rectangular waveguide, which transitions to a conical horn with a circular cross-section. The inner dimensions of the rectangular waveguide have a width and length of approximately 16.51 and 8.26 cm, respectively. The length of the waveguide before flaring to the conical horn is 1.27 cm. The inner diameter of the circular aperture of the antenna is approximately 16.5 cm. The horn flares to this diameter from the rectangular waveguide over a distance of approximately 30.5 cm, and the cross-sectional area of the horn remains constant for a distance of 0.635 cm at the output of the horn. The horn and waveguide are completely filled with lossless material with a permittivity and permeability that are modified between simulations. The surrounding materials are defined as free space. While coupling to the material-loaded horn is outside the scope of this paper, it should be noted that couplers have previously been designed to transition from larger air-filled waveguides to the more compact loaded waveguide of the horn antenna. Alternatively, the signal can be coupled into the loaded waveguide structure through probe coupling.

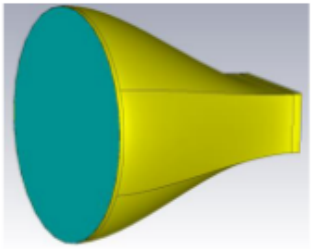

Figure 1. The loaded conical horn simulated with dielectric, magnetic, and magnetodielectric fillers

The following three graphs display the return loss of the horn antenna with only the values of the relative permeability and dielectric constant varied between simulations. Figure 2 plots the return loss of the baseline case in which the horn antenna is filled with air. To simulate this unloaded case, the properties of the filler are defined as $\varepsilon_r = \mu_r = 1$. The cutoff frequency is approximately 904 MHz. The return loss goes below -10 dB at approximately 925 MHz and remains below -15 dB at frequencies greater than 946 MHz.

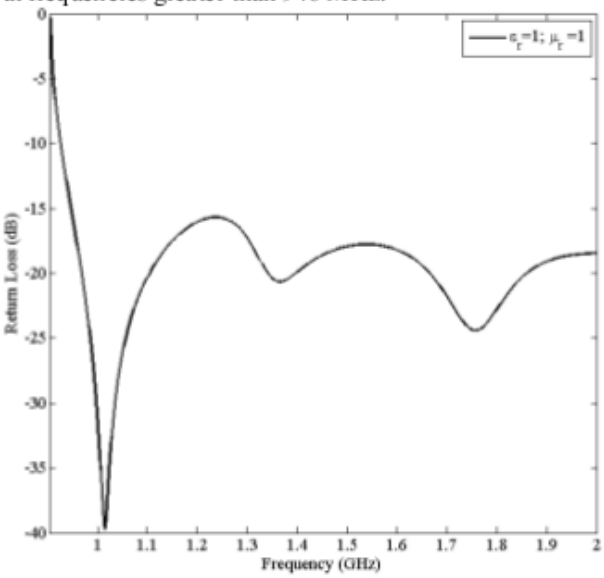

Figure 2. The return loss of the conical horn filled with air. $\varepsilon_r = \mu_r = 1$

Reduction of the operational band of the same conical horn antenna is examined for cases of dielectric, magnetic, and magnetodielectric loading. In the first set of simulations, the product of ε_r and μ_r is equal to 3. In the case of dielectric loading, the dielectric constant is defined to be 3, and the relative permeability is defined to be 1. Similarly, for the magnetic loading case, the relative permeability is defined to be 3, and the dielectric constant is set equal to 1. To compare a magnetodielectric case with an equivalent size reduction factor, the dielectric constant and relative permeability are set equal to each other with a value of $\sqrt{3}$ or 1.732. The plots of dielectric, magnetic, and magnetodielectric loading with $\varepsilon_r \mu_r = 3$ are shown in Figure 3. In all cases, the cutoff frequency is

reduced to approximately 522 MHz. The reduction of the cutoff frequency from 904 MHz to 522 MHz can be predicted from equation 3.The symbol f_{loaded} [Hz] is the cutoff frequency of the antenna loaded by a material, and the symbol f_0 [Hz] represents the frequency of the unloaded or air-filled horn antenna.

$$f_{loaded} = \frac{f_0}{\sqrt{\varepsilon_r \mu_r}} \tag{3}$$

While the cutoff frequency is the same regardless of whether the loading is dielectric, magnetic, or magnetodielectric, there are significant differences in the return loss and the operational bandwidth of the three cases. In the dielectric case, the return loss is below -10 dB between 600 and 720 MHz and above 835 MHz. Low frequency operation with magnetic loading is improved over dielectric loading as the first band below -10 dB extends from 540 to 790 MHz. Magnetodielectric loading provides the best performance with the return loss below -10 dB at frequencies above 530 MHz. Except for a peak between 800 and 850 MHz, the return loss is lower than -15 dB up to at least 1 GHz for the magnetodielectric-loaded horn.

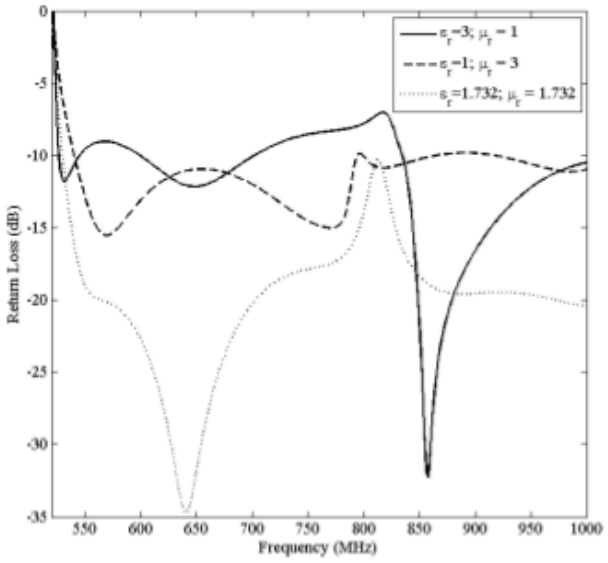

Figure 3. The return loss of the conical horn filled with dielectric, magnetic, and magnetodielectric material. For all cases, $\varepsilon_r \mu_r = 3$.

The next set of simulations further increases the value of the permittivity and permeability such that the product of the dielectric constant and relative permeability is 9. As in the previous example, for dielectric loading the dielectric constant is set equal to 9, and the relative permeability is 1. For magnetic loading, the dielectric constant is defined to be 1, and the relative permeability is set to 9. In the case of magnetodielectric loading, both the dielectric constant and relative permeability are equal to 3 such that the product of the two values is 9.

Figure 4 shows the return loss of the dielectric, magnetic, and magnetodielectric loading of the conical horn with $\varepsilon_r \mu_r = 9$. As in the previous example, the cutoff frequency is reduced to the same value in all three cases. With a cutoff frequency of just over 300 MHz, the frequency has been reduced according to equation 3 and is one-third the value of the air-filled horn. However, with higher values for the dielectric constant and relative permeability, the return loss is significantly different between the three types of loading. The return loss for dielectric loading with a dielectric constant of 9 is never below -10 dB, and the antenna would likely need design modifications to make it usable with this relatively high dielectric constant. In the case of magnetic loading, there are only small bands from 312 to 345 MHz and 411 to 455 MHz at which the return loss is below -10 dB. The magnetically loaded antenna may be useful in these bands, but it would also likely require modifications to the design. In the case of magnetodielectric loading, there is a small band from approximately 303 to 315 MHz and a much larger band from 350 to 480 MHz with return loss below -10 dB. The return loss is much lower than -10 dB above approximately 487 MHz. Magnetodielectric loading significantly improves the return loss and increases the bandwidth at which the conical horn can be operated.

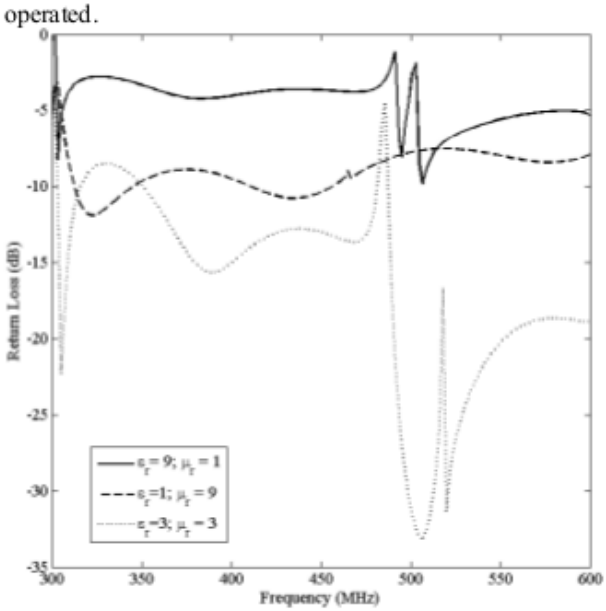

Figure 4. The return loss of the conical horn filled with dielectric, magnetic, and magnetodielectric material. For all cases, $\varepsilon_r \mu_r = 9$.

III. LOADED HELICAL ANTENNA

A helical antenna was also simulated with dielectric, magnetic, and magnetodielectric loading as shown in Figure 5. The helix is axially loaded with a solid mandrel of the loading material down the center of the helix. The helix consists of 6 turns with a turn-to-turn spacing of 7.5

cm. The diameter of the helix wire is 0.5 cm. The helix is wrapped around a cylinder of material with a diameter of 9 cm. The ground plane has a diameter of 40 cm and a thickness of 3 cm. The center conductor of the coaxial feed extends above the ground plane by 1.5 cm to the junction with the base of the helix.

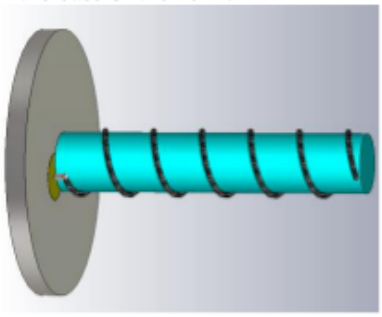

Figure 5. Helical antenna axially loaded with a cylinder modeled as a dielectric, magnetic, and magnetodielectric material

Figure 6 shows the return loss of the helical antenna in the air-filled, unloaded case with material values defined as $\varepsilon_r = \mu_r = 1$. The return loss is below -10 dB at frequencies as low as 685 MHz and remains below -10 dB through 1.5 GHz. The circumference of the mandrel around which the helix is wound is 0.283 m. A free-space wavelength equal to this distance is approximately 1.05 GHz, and an estimate of the band at which the antenna operates in the axial mode can be calculated to be between 790 MHz and 1.3 GHz. Examination of the far field pattern verifies that the antenna operates in the axial mode as low as 600 MHz and up to approximately 1.35 GHz. Above 1.35 GHz, the far field pattern has its peak off-axis and is not considered to be operational in the axial mode even though the return loss is still acceptable.

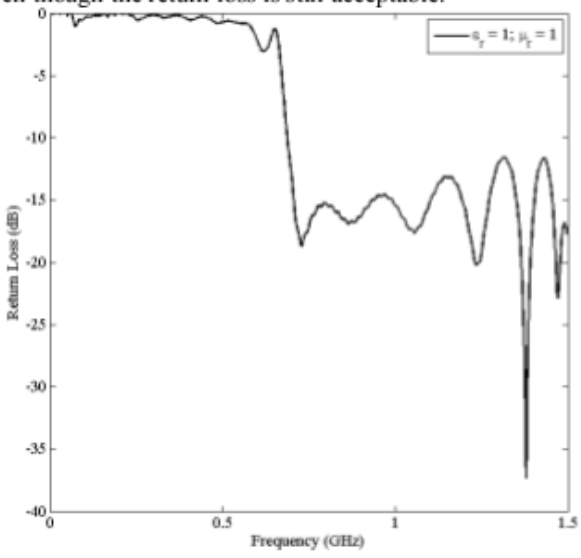

Figure 6. The return loss of the helical antenna with an air core

The materials loading the center of the helix are then defined such that the product of the dielectric constant and relative permeability are equal to 3. In the cases of dielectric and magnetic loading, the dielectric constant and relative permeability are set to 3, respectively, while the other parameter is defined to be equal to 1. For the case of magnetodielectric loading, both parameters are set equal to $\sqrt{3}$ such that their product would be the same as the cases of dielectric and magnetic loading. As shown in Figure 7, the return losses of all three cases match very closely up to the point at which they cross below -10 dB at approximately 579 MHz. In contrast to the frequency downshift seen in the conical horn, the frequency downshift of the helical antenna is less than that predicted by equation 3. It is believed that the frequency is downshifted by a lower factor because the wave traveling along the helix travels not only through the material loaded in the center of the helix but also in the surrounding air. Therefore, similar to the effective permittivity calculated for a microstip line, the frequency is shifted down by an effective value less than $\sqrt{3}$. Using 685 MHz as the lowest frequency at which the return loss was below -10 dB in the air-filled case and 579 MHz for the loaded cases, the frequency was downshifted by a factor of $\sqrt{1.4}$. All three cases of loading show a wide bandwidth of potential operation at which the return loss is below -10 dB. For the dielectric, magnetic, and magnetodielectric cases, the return loss remains below -10 dB until 1.026 GHz, 993 MHz, and 1.13 GHz, respectively. The return loss in the case of magnetic loading, while going above -10 dB at 993 MHz, remains less than -9.87 dB through 1.23 GHz.

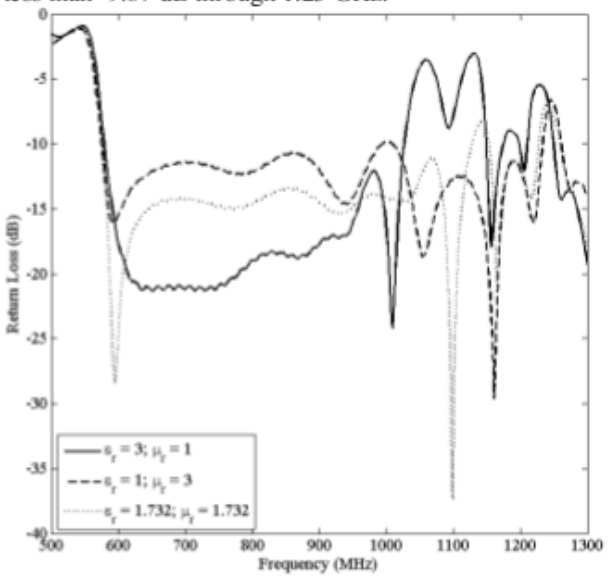

Figure 7. The return loss of the helical antenna filled with dielectric, magnetic, and magnetodielectric material. For all cases, $\varepsilon_r \mu_r = 3$.

The final set of simulations has the product of the dielectric constant and relative permeability defined as 9.

In contrast to the previous example of the helical antenna, the frequencies at which each case first goes below -10 dB differ significantly. The return losses of the dielectric, magnetic, and magnetodielectric cases first cross below -10 dB at 470, 511, and 480 MHz, respectively. Again, the frequency downshift of the axially loaded helical antenna is less than that predicted by equation 3 due to the material not fully containing the waves propagating along the helix. The upper frequency at which return losses of the dielectric, magnetic, and magnetodielectric cases cross above -10 dB are 561, 660, and 653 MHz, respectively. The case of loading with the magnetodielectric material had the largest band below -10 dB at 173 MHz as opposed to bandwidths of 91 and 149 MHz for dielectric and magnetic loading, respectively. While all three types of loading could be effectively applied with these relatively low dielectric constant and relative permeability values, magnetodielectric loading has the advantage of providing the largest bandwidth.

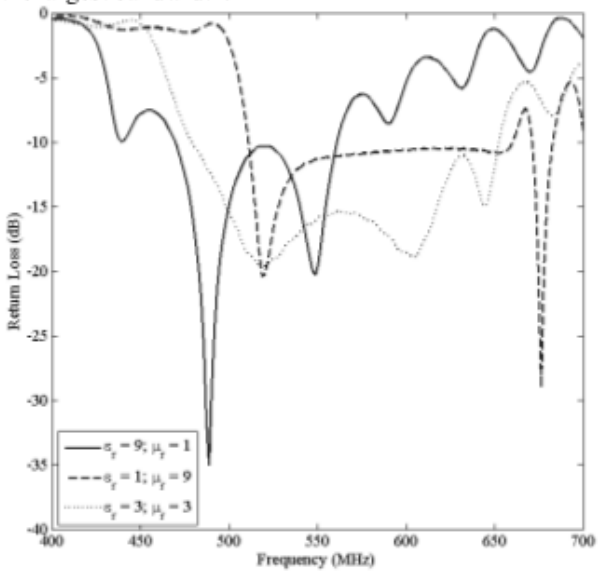

Figure 8. The return loss of the helical antenna filled with dielectric, magnetic, and magnetodielectric material. For all cases, $\varepsilon_r \mu_r = 9$.

IV. CONCLUSIONS

Magnetodielectric loading for high power antennas has been compared through simulations to dielectric and magnetic loading of a conical horn and helical antenna. For the conical horn, the frequency downshift was shown to be proportional to the inverse square root of the product of the dielectric constant and the relative permeability. When the product of the dielectric constant and relative permeability were increased to 9, the magnetodielectric material was the only viable option that provided the expected frequency downshift with an acceptable return loss and bandwidth. For the helical antenna, the shift of the operating band was less than that seen in the conical horn due to the wave propagating in both the loading material and the air surrounding the helix. While dielectric and magnetic loading also had bands at which the return loss was below -10 dB, magnetodielectric loading provided the largest bandwidth.

In both of the examples, the magnetodielectrics were defined with equal values for the dielectric constant and relative permeability. While that definition theoretically keeps the characteristic impedance as calculated by equation 2 the same as if the antenna were unloaded, there are likely many instances in which an antenna's performance can be improved when both the dielectric constant and relative permeability are greater than one but unequal. The design flexibility of controlling both parameters is one advantage of utilizing metamaterials with magnetodielectric properties. Future work in refining antenna designs for experimental verification will allow the values to be changed independently.

V. REFERENCES

[1] K. A. O'Connor and R. D. Curry, "High dielectric constant composites for high power antennas," in *Proc. IEEE Pulsed Power Conf.*, Chicago, IL, 2011.

[2] H. Mosallaei and K. Sarabandi, "Magneto-dielectrics in electromagnetics: concepts and applications," *IEEE Trans. on Antennas and Propagaion,* vol. 52, no. 6, pp. 1558-1566, 2004.

[3] P. M. T. Ikonen, K. N. Rozanov, A. V. Osipov, P. Alitalo and S. A. Tretyakov, "Magnetodielectric substrates in antenna miniaturization: potential and limitations," *IEEE Trans. on Antennas and Propagation,* vol. 54, no. 11, pp. 3391-3399, 2006.

[4] A. Pearson, R. D. Curry and K. A. O'Connor, "First results in the development of double-positive metamaterials for high power components," in *IEEE Power Modulator and High Voltage Conference*, Santa Fe, NM, 2014.

[5] G. M. Yang, O. Obi, M. Liu and N. X. Sun, "Miniaturized patch antennas with ferrite/dielectric/ferrite magnetodielectric sandwich substrate," *PIERS Online,* vol. 7, no. 7, pp. 609-612, 2011.

[6] R. C. Hansen and M. Burke, "Antennas with magneto-dielectrics," *Microwave and Optical Technology Letters,* vol. 26, no. 2, pp. 75-78, 2000.

[7] D. Rialet, A. Sharaiha, A. C. Tarot, X. Castel and C. Delaveaud, "Characterization of antennas on dielectric and magnetic substrates effective medium approximation," *Radioengineering,* vol. 18, no. 4, pp. 348-353, 2009.

[8] D. Souriou, J. L. Mattei, S. Boucher, A. Sharaiha, A. C. Tarot, A. Chevalier and P. Queffelec, "Antenna miniaturization and nanoferrite magneto-dielectric materials," in *14th Intl. AMEREM*, Ottawa, ON, Canada, 2010.

High Frequency Properties of High Voltage Barium Titanate-Ferrite Multiferroic Metamaterial Composites[1]

Kelli M. Noel, Aric M. Pearson, Randy D. Curry, Kevin A. O'Connor
Center for Physical and Power Electronics
University of Missouri
Columbia, MO, 65211, USA

ABSTRACT

Permittivity and permeability parameters of dielectric composites made of ferrite particles coated in a barium titanate ($BaTiO_3$) layer were analyzed and compared against composites of ferrite powders with no dielectric layer. A hydrothermal synthesis process combined barium hydroxide ($Ba(OH)_2$) and titanium dioxide (TiO_2) to form the coating of barium titanate around a ferrite core. These barium titanate ferrite composites particles are then combined with a unique binder to form a metamaterial. Discs of the metamaterial are characterized with an Agilent coaxial airline and dielectric measurement software to determine the permittivity and permeability responses within a frequency range of 20 MHz to 4 GHz. By comparing these results to previous work on ferrite composites, the merit of insulating the magnetic particles with a dielectric layer is examined.

Index Terms — **Materials processing, magnetic materials, dielectric materials, permeability, permittivity, HF antennas**

1 INTRODUCTION

Materials that possess both ferroelectric and ferromagnetic properties have potentially numerous applications in the field of electromagnetics. One of the most defining applications for such materials is antenna size reduction. When antennas are used in the very high frequency (VHF) and ultra-high frequency (UHF) ranges, 30 MHz to 3 GHz, the hardware can get very bulky and heavy, so the reduction in size is increasingly important [3]. Antenna size (l) [m] is related to the wavelength (λ) [m] to be propagated through the antenna medium. This antenna size can be reduced significantly by changing the frequency (f), permittivity (ε), or permeability (μ) as described by Equation 1 [1]. Many antennas used in the UHF and VHF ranges are designed for specific frequency bands so increasing the μ_r and ε_r is the how size can be reduced.

$$l \propto \lambda = \frac{c}{f\sqrt{\varepsilon_r \mu_r}} \tag{1}$$

Impedance of a material (Z_m) in relation to the impedance of free space (Z_0) is given by Equation 2 [1]. Changing only the permittivity of a material can reduce the size of antennas, but the characteristic impedance will also change. Without also changing the permeability of the material, the impedance of the antenna will be mismatched [3]. Using a multiferroic material allows impedance matching as well as reduction of antenna size.

$$Z_m = Z_0\sqrt{\frac{\mu_r}{\varepsilon_r}} \tag{2}$$

Applications of materials in the field of pulsed power must also be able to withstand high electric fields.

Materials with both ferromagnetic and ferroelectric properties in one phase do not occur in nature so they must be manufactured [2]. Manufactured materials with multiferroic properties that are not found in nature are also known as metamaterials [3]. The ferromagnetic phase is usually conductive, which would inhibit some of the applications in high frequency applications. To mitigate this property, the ferromagnetic phase must be insulated by the ferroelectric phase [2]. Ferrites make a good ferromagnetic phase due to their low conductivity and high permeability, but they can also be lossy in the UHF and VHF bands [4] [5] [6]. Perovskite ceramics have high permittivity values that, when used as a dielectric medium, can reduce the size of an antenna by a factor of 10 or more. Barium titanate ($BaTiO_3$) is one such ceramic that has ε_r values of 100 or greater and high dielectric strength. To decrease the losses, the ferroelectric phase can be made of low loss ceramics such as $BaTiO_3$ [7].

Pulsed power applications require materials that can hold off high voltages without breaking down. Many of these applications also need materials that can be engineered into thick substrates that can be machined into complex shapes [3]. $BaTiO_3$ substrates that have been designed for these

[1] *All work supported by the Office of Naval Research (code 30) contract N0001413-0516*

applications show a dielectric strength ranging from 150 to 250 kV/mm [3].

The combination of ferrites and $BaTiO_3$ as a metamaterial has been explored in the past. Solid combination and sintering of the two phases increase the magnetoelectric (ME) effects, but the material was very lossy [8]. The losses occurred because the two phases' boundaries were not matched, causing micro cracks and low material density [7]. To better match the boundaries of the two phases a new composite is proposed. The new procedures attempt to isolate each ferromagnetic particle and surround it with the ferroelectric phase and can be achieved with sol-gel, or hydrothermal synthesis methods.

For this study a hydrothermal synthesis method was used to form a barium titanate ferrite (BTF) composite. The ferromagnetic phase was chosen to be nickel-zinc ferrite ($Ni_xZn_xFe_2O_4$) since it has been seen to have lower losses than other ferrites [5]. The ferrite used was purchased in bulk form to ensure the hexaferrite phase [4]. The $BaTiO_3$ was chosen as the ferroelectric phase for its high dielectric strength, low losses, and high relative permittivity [3]. The boundaries of the two phases are very well matched with $BaTiO_3$ having a lattice parameter of a=0.4006 nm and $Ni_xZn_xFe_2O_4$ with a=0.8337 nm, almost double the $BaTiO_3$ [5]. This ensures that the bonds made for epitaxial growth of the $BaTiO_3$ are not strained, creating a well matched interface.

The hydrothermal synthesis process was based on a procedure for synthesizing $BaTiO_3$ powders with high strength as outlined by Eckert [8]. This process combined with $Ni_xZn_xFe_2O_4$ powders creates a metamaterial composite that has multiferroic properties in the VHF range. A ferrite metamaterial has also been developed from sintered nickel-zinc ferrites and used as a comparison to the electromagnetic properties of the BTF composites.

2 EXPERIMENTAL PROCEDURES

2.1 SYNTHESIS OF PARTICLES

The dielectric composite powders were synthesized using a hydrothermal synthesis procedure combining a ferromagnetic core with a ferroelectric coating. The core of the metamaterial was made of nickel-zinc ferrite ($Ni_xZn_xFe_2O_4$). This ferrite was purchased in bulk and processed into powder with particle sizes less than 45 µm. The other chemical reagents necessary for the process were barium hydroxide ($Ba(OH)_2$) and titanium oxide (TiO_2). These chemicals needed no further purification so were used as received.

The $Ba(OH)_2$ and TiO_2 were combined with a 1:1 molar ratio with distilled water. Ferrite was then combined in the solution. The final solution was then placed in a hydrothermal reactor at 90 ^{0}C for 72 hours. The resulting powder was then dried and milled to break up the individual particles. A strong magnet was used to separate the powders with magnetic cores from any excess $BaTiO_3$ particles. This step ensured the presence of ferrite cores in every particle. The final powder was pressed into discs with a unique binder to form composite metamaterial solids. The discs were pressed into 7 mm diameter samples necessary for dielectric property characterization.

The length of the samples prepared for characterization was specifically designed for a higher range of frequencies (200 MHz - 2 GHz). Optimal sample length in a coaxial structure can be found using Equation 3, where the length of the sample is $\lambda_s/4$ and ε_r and μ_r are known. Equation 3 [4] assumes a single frequency measurement, and the properties were characterized over a range of frequencies. It was experimentally determined that a sample thickness of 6 mm would be ideal for frequencies in the range of 200 MHz-2 GHz with minimal error.

$$\lambda_s = \left(\frac{\lambda_0}{\sqrt{\varepsilon_r \mu_r}}\right) \quad (3)$$

2.2 CHARACTERIZATION OF SAMPLES

The presence of nickel-zinc ferrite and $BaTiO_3$ in the composite powders was confirmed using energy dispersive spectroscopy (EDS) in a scanning electron microscope (SEM). The SEM analysis of $BaTiO_3$ particles synthesized without ferrite was analyzed to determine makeup, phase, and size. The configuration of the particles formed was analyzed using transmission electron microscopy (TEM).

The multiferroic properties of the composite were measured using an Agilent 50 Ohm, Type N airline, an Agilent network analyzer, and dielectric measurement software. The software uses S parameters to calculate the ε_r and μ_r using the Ross-Nicolson method [9]. To use the airline, the samples were machined into toroids. The toroids were machined with an inner diameter of 3 mm and the outer diameter of 7 mm.

3 RESULTS AND DISCUSSION

3.1 SEM AND TEM RESULTS

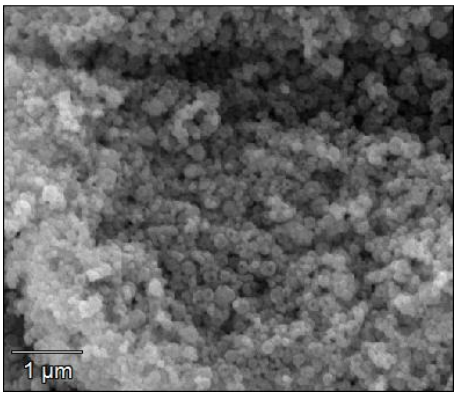

Figure 1: SEM image of synthesized $BaTiO_3$

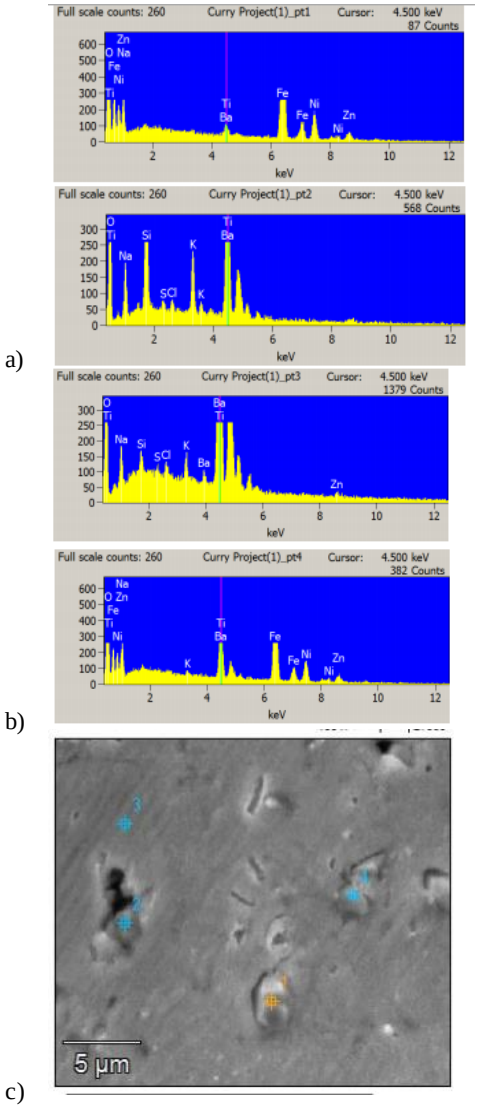

Figure 2: a) EDS plot of points 1 and 2 b) EDS plots of points 3 and 4 c) SEM image of material with EDS

The SEM images of the synthesized $BaTiO_3$ particles without ferrite (Figure 1) show that the size of the particles are around 100 µm. This implies the coating of $BaTiO_3$ around the ferrite is 100 µm in thickness. The EDS spectrum confirms the $BaTiO_3$ chemistry as well as phase. Figure 2c shows four points of particles suspended in resin for EDS analysis. Figures 2a and 2b are the resulting spectra. The presence of nickel-zinc ferrite is seen at point 1 and 4 on the EDS spectrum around 6 and 7 keV, seen in Figure 2a. These particles are surrounded by $BaTiO_3$ at point 2 and 3 and seen on the spectrum around 4.5 keV seen in Figure 2b.

3.2 DIELECTIC PROPERTIES

The relative dielectric and permeability constants of the BTF composites were calculated and compared to ferrite composites. The dielectric constants are seen in Figure 3 and the process increases the dielectric constant of the ferrite metamaterials by about one. The permeability of the BTF composite, seen in Figure 4, is lower than the ferrite but does not drop as quickly at higher frequencies. This effect is a result of the amount of magnetic material in the BTF particles.

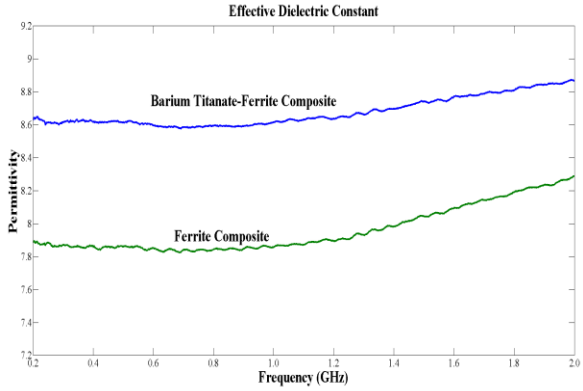

Figure 3: Dielectric constants of ferrite and barium titanate-ferrite composites.

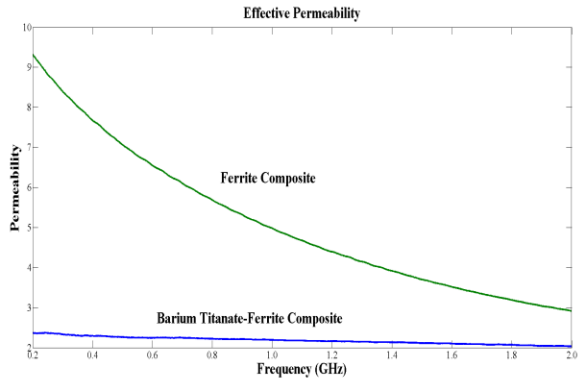

Figure 4: Permeability of ferrite and barium titanate-ferrite composites.

The losses of the barium titanate-ferrite composites is also compared to ferrite composites. Figure 5 and Figure 6 show the dielectric and magnetic losses of both materials. The dielectric losses of the BTF composites are higher than the ferrites, but both materials still have rather low dielectric loss. The magnetic loss of the BTF material is much less than ferrite composites. By separating the individual magnetic domains with dielectric material, the interaction between the ferrite particles lessens, thus decreasing the loss. If the particle size of the magnetic core contains a partial magnetic domain, the magnetic field will extend into the $BaTiO_3$ [10] [11].

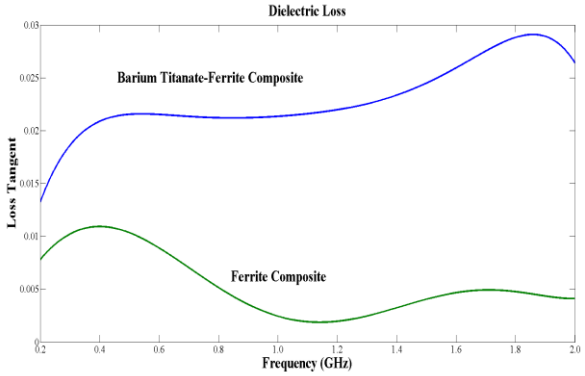

Figure 5: Dielectric losses of ferrite and barium titanate-ferrite composites.

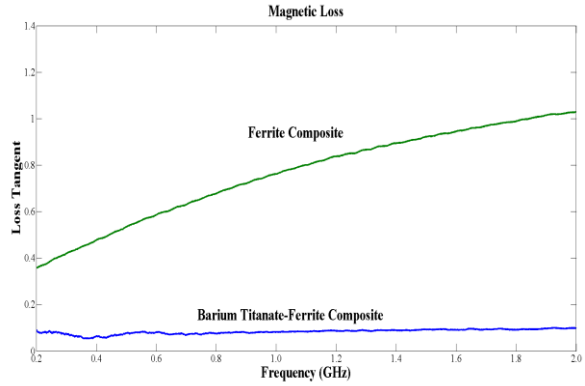

Figure 6: Magnetic losses of ferrite and barium titanate-ferrite composites.

The relative impedance of the two materials and relative wave velocities were calculated from the measured permittivity and permeability. The relative impedance of the BTF material is less than that of free space (377Ω) but stays relatively constant across all frequencies. The ferrite materials do get close to impedance of free space around 400 MHz, but quickly decrease due to the decreasing permeability. The relative wave velocity of the BTF composites is close to one fourth the speed of light, and relatively constant across the frequency range. These properties show that an antenna using this material would have a possible size reduction by a factor of four.

High voltage measurements of the barium titanate-ferrite composite have also been obtained. The composites show a high-voltage breakdown around 215 kV/cm [12].

4 CONCLUSION

The synthesis of barium titanate ferrite composites was achieved and compared to ferrite composites. SEM and EDS analysis has confirmed the presence of both nickel-zinc ferrite and barium titanate phases is the same compound. The BTF composites show 44% increased permittivity and 81% reduced permeability over prepared ferrite composites. The magnetic losses decrease drastically with the separation of magnetic domains, while the dielectric loss remains very low, around .021. The addition of the dielectric phase also reduces the drop in permeability as the frequency is increased, this could lead to larger frequency bands in applications of the material. The dielectric strength of the material shows the usefulness of the composites in pulsed power applications. Further investigation of particle sizing and material packing density could decrease the dielectric losses and create a lower loss composite material for high frequency applications. Tailoring the thickness of the dielectric layer could also increase permittivity and capacitance between particles allowing better impedance matching in antenna applications.

REFERENCES

[1] Balanis, Constantine A. Antenna Theory. 3rd ed. New York: Harper & Row, 1982. Print.

[2] G. Schileo, "Recent developments in ceramic multiferroic composites based on core/shell and other heterostructures obtained by sol–gel routes*", Progress in Solid State Chemistry*, Volume 41, Issue 4, December 2013, Pages 87-98

[3] K. A. O'Connor and R. Curry, "High dielectric constant composite for high power antennas," *IEEE Pulsed Power Conference*, 2011.

[4] A. M. Pearson, R. Curry, and K. A. O'Connor, "First Results in the Development of Double-Positive Metamaterials for High Power Microwave Components" *IEEE International Power Modulator and High Voltage Conference*, Santa Fe, NM, 2014.

[5] Jian-Ping Zhou et al, 2012. "Hydrothermal synthesis and properties of NiFe2O4@BaTiO3 composites with well-matched interface" Sci. Technol. Adv. Mater. 13 045001

[6] H. Mosallaei and K Sarabandi, "Magneto-Dielectrics in Electromagnetics: Concept and Applications" *IEEE Transactions on Antennas and Propogation*, Vol. 52, No 6. June 2004

[7] Mitoseriu L, Buscaglia V. "Intrinsic/extrinsic interplay contributions to the functional properties of ferroelectric-magnetic composites." *Phase Trans* 2006; 79(12):1095e121

[8] J. O. Eckhart Jr. et al. "Kinetics and Mechanics of Hydrothermal Synthesis of Barium Titanate" *Journal of American Ceramics Society*. 79 [11] 2929-39, 1996.

[9] A. M. Nicolson and G. F. Ross. "Measurement of the Intrinsic Properties of Materials by Time-Domain Techniques" *IEEE Transactions on Instrumentation and Measurement*. 19(4) 377-382. November 1970.

[10] CG Duan, SS Jasawal, and EY Tsymbal. "Predicted Magnetoelectric Effect in Fe/BaTiO3 Multilayers: Ferroelectric Control of Magnetism." *Physics Review Letters*. 97(4). July 2008.

[11] C Wang et al. "Magnetic and Dielectric Properties of Barium Titanate-Coated Barium Ferrite." *Journal of Alloys and Compounds* 479(2) 560-565. May 2009.

[12] K. M. Noel, A. M. Pearson, R. D. Curry and K. A. O'Connor "The Dielectric Strength of Metamaterial Composites" Presented at the *IEEE Pulsed Power Conference*, Austin, TX. June 2015.

Kelli M. Noel was born in Springfield, Missouri in 1990. She received her BS in Biomedical Engineering from The George Washington University in 2012, and is now pursuing a MS degree in Electrical Engineering. Kelli has worked for multiple research labs, and is focusing her talents in pulsed power and applications for medical technologies. Her society memberships include IEEE, Eta Kappa Nu, Theta Tau, and the Society of Women Engineers.

Aric M. Pearson was born in Slidell, Louisiana in 1991. He received a BS in Physics from Truman State University in 2013. He is currently working towards a MS in Electrical Engineering at the University of Missouri and does research for the Center for Physical and Power Electronics in the areas of Pulsed Power, Metamaterials, and RF Design. He is a student member of IEEE as well as a member of Eta Kappa Nu.

Randy D. Curry While in industry Dr. Curry developed new applications of pulse power including nanodielectric materials, optically triggered picosecond solid state switches, rep-rate oil switches, picosecond rise time modulators, compact modulators, solid state modulators, high power broadband sources, tacitron switches (AFRL/DE) and pulse power acoustic sources. Dr. Curry's team at Titan/PSI was the first to demonstrate 500kV-1MV, 100-picosecond rise time, Gigawatt UWB, kilohertz oil switches in 1992 (MICOM Pulser). Also as team member, Dr. Curry developed the original conceptual design for the GEM HPM solid-state source built for AFRL/DE. He also built a high temperature tacitron switch for AFRL for utilization in the TOPAZ nuclear reactor program. Working with a team of scientists and engineers he designed and built the two electron beam systems for the Laser Radar MIT Firepond facility, which was voted the most successful SDIO program of 1990-1991. Dr. Curry as principal investigator is presently directing an interdisciplinary team of mathematicians, physicists, civil engineers, and pulsed power engineers for detection and neutralization of asymmetric threats. He is presently funded for narrowband antenna development using nanodielectrics. His expertise includes pulse power, piezoelectric applications, optical switching, electron beams, megavolt accelerator applications and applications of pulse power. Dr. Curry has published over 120 journal and conference articles, holds a secret clearance and is a member of the DEPS, IEEE, APS, ACS, and holds 12 patents. Dr. Curry was the Chair of the 2011 IEEE PPC that was held in Chicago Illinois. He holds two Electrical Engineering degrees from Texas Tech and a PhD from St. Andrews University.

Kevin A. O'Connor (S'06, M'13) was born in Aurora, Illinois in 1983. He received B.S. and M.S. degrees in electrical engineering from the University of Missouri-Columbia in 2005 and 2008, respectively. He earned a PhD in electrical and computer engineering from the University of Missouri in 2013.He was a Fellow of the National Physical Science Consortium from 2008 to 2011 through the support of Sandia National Laboratories. He is currently an Adjunct Assistant Research Professor at the University of Missouri and co-founder of NanoElectromagnetics LLC. He has previously investigated power conditioning systems for flux compression generators, including air-core pulse transformers, exploding-wire fuses, and RF sources. His current research focuses on the development of several types of high dielectric constant composite materials and their application in antennas and capacitors. Dr. O'Connor was a finalist for the IEEE Nuclear and Plasma Sciences Society's student paper of the year award for 2010-2011. He was awarded a Tom Burkes Outstanding Graduate Student Award at the 2012 Power Modulator Conference in San Diego, CA. His society memberships include IEEE, Sigma Xi, and Tau Beta Pi.